UNIVERSITY OF LIVERPOOL

THE UNIVERSITY *of* LIVERPOOL

Advanced Control of VSC-HVDC Systems for Dynamic Performance Enhancement

Thesis submitted in accordance with the
requirements of the University of Liverpool
for the degree of Doctor of Philosophy

in

Electrical Engineering and Electronics

by

Yiyan Sang,

February 2019

Advanced Control of VSC-HVDC Systems for Dynamic Performance Enhancement

by

Yiyan Sang

Acknowledgements

I would like to give my heartfelt thanks to my supervisor, Dr. L. Jiang, whose encouragement, guidance and support enabled me to develop a deep understanding of my work. Without his consistent and illuminating instructions, my research work and my life could not proceed to this stage. The research skill, writing skill and presenting skill he taught me will benefit me throughout my life.

I offer my regards and blessings to all of the members of Smart Grid Control and Renewable Energy Group, the University of Liverpool, especially to Dr. B. Yang for his kind and helpful discussion on power system modelling and operation, Dr. C. K. Zhang for his expert control knowledge, and Dr. K. Shi for his hardware skill teaching. I would like to devote my deepest thank and love to my family and friends, who always encourage me when my project went through failures one after another.

I am grateful to the Department of Electrical Engineering and Electronics at the University of Liverpool, for providing the research facilities that made it possible for me to carry out this research.

Abstract

The fundamental changes in the generation of electrical power within recent decades raised the need for smarter and more flexible power grids. High voltage direct current (HVDC) technology has been regarded as an ideal supplement to existing AC power grids for energy conversion, power flow control, and stability enhancement. The rapid progress of self-commutating high-voltage high-current semiconductor switches, which mainly attributed to the development of the insulated gate bipolar transistor (IGBT), has led to the rise of voltage-source converter (VSC) HVDC technology. Control system plays a key role to maintain the proper operation of VSC-HVDC system due to the full controllability of its power electronic devices.

Conventional control strategies, which is based on classic linear control theory, maintain the expected performance for a wide range of operation points with complicated tuning processes and are hardly able to guarantee the global stability in nonlinear systems with ease. The objective of the research work presented in this thesis is to improve the VSC-HVDC system dynamic performance via modifying the controller with advanced control strategy.

Multiple advanced control strategies have been proposed for the control of VSC-HVDC system based on Lyapunov theory because of the high nonlinearity and strong coupling between each state in VSCs. Current tracking problem in the modular multi-level converter (MMC) low-level controller cost huge control energy due to its high-resolution time-varying reference signal. Passivity based control (PBC) is proposed and applied for improving the system damping and saving control energy cost as the beneficial system nonlinearities are remained instead of being fully cancelled.

Since that the two terminal point-to-point VSC-HVDC system is complicated

nonlinear system and involving with excessive system uncertainties and various unexpected external disturbance, the robustness against these effects ie required to be enhanced. Sliding mode state and perturbation observer (SMSPO) is developed as one robust extended state observer (ESO) to estimate the combinatorial effect of nonlinearities, parameter uncertainties, internal unmodelled dynamics and time-varying external disturbances in VSC-HVDC systems. Perturbation observer based sliding mode controller (POSMC) is proposed based on robust sliding mode control theory with adopting SMSPO for enhancing the whole system robustness against comprehensively.

Fault ride-through (FRT) capability of VSC-HVDC system with offshore wind farm integration is inspired by strict grid code requirements. FRT capability of type 2 generating plants like offshore wind turbines is considered and investigated with corresponding VSC-HVDC transmission system. Nonlinear adaptive control(NAC) is proposed as one of the novel nonlinear adaptive control strategies and combined de-loading strategy which is designed and proposed for suppressing the surge effects during the FRT process especially. Hence the FRT performance of the whole system is well improved and the corresponding FRT capability is enhanced.

VSC based multi-terminal HVDC (VSC-MTDC) systems with wind farm integration garnered massive attention these years for that several practical projects have put into service. Perturbation observer based robust passivity based control (PORPC) is proposed based on PBC which is enhanced by adopting high-gain state and perturbation observer (HGSPO) for being more applicable in complicated systems like VSC-MTDC system with wind farm integration without requiring the accurate system model and providing extra excellent robustness against system uncertainties. PORPC is applied to VSC-MTDC system and combined with the essential droop control strategy in order to appropriate load sharing. The combinatorial effect of interaction between different terminals, unmodelled dynamics and unknown time-varying external disturbances are aggregated into a perturbation, which is estimated online by an HGSPO and can be represented as a chained-integrator system associated with matched nonlinearities and disturbances.

Declaration

The author hereby declares that this thesis is a record of work carried out in the Department of Electrical Engineering and Electronics at the University of Liverpool during the period from October 2014 to September 2018. The thesis is original in content except where otherwise indicated.

Contents

List of Figures

List of Tables

List of Abbreviations and Notations

Abbreviations in Control Systems

PC	Passive control.
PO	Perturbation observer.
HGO	High-gain observer.
HGPO	High-gain perturbation observer.
HGSPO	High-gain state and perturbation observer.
FLC	Feedback linearization control.
APC	Adaptive passive control.
POAPC	Perturbation observer based adaptive passive control.
RPC	Robust passive control.
CPC	Coordinated passive control.
CAPC	Coordinated adaptive passive control.
POCAPC	Perturbation observer based coordinated adaptive passive control.
PID	Proportional-integral-derivative.
VC	Vector control.
PI	Proportional-integral.
SMO	Sliding-mode observer.
SMC	Sliding-mode control.
TDC	Time delay control.
ADP	Adaptive dynamic programming.
ADRC	Adaptive disturbance rejection controller.
CLF	Control Lyapunov function.
SISO	Single-input single-output.
MIMO	Multi-input multi-output.

Abbreviations in VSC-HVDC Systems

VSC	Voltage source converter.
LCC	Line-commutated converter.
MMC	Modular multi-level converter.
HVDC	High voltage direct current.
VSC-HVDC	Voltage source converter based high voltage direct current.
VSC-MTDC	Voltage source converter based multi-terminal high voltage direct current.
HIL	Hardware-in-the-loop.
FRT	Fault ride-through.
IGBT	Insulated gate bipolar transistor.
PWM	Pulse width modulation.
SPWM	Sinusoidal pulse width modulation.
SVM	Space vector modulation.
PLL	Phase-locked loop.
AC	Alternating current.
DC	Direct current.
I/O	Input/output.
A/D	Analogue/digital.
SVPWM	Space vector pulse width modulation.

Symbols

$\forall$	for all.
$\exists$	exist.
$\Rightarrow$	implies.
$\rightarrow$	tends to.
$\mapsto$	maps to.
∂	partial derivative.
$\sum$	sum.
$\in$	in.
∞	infinity.
$\angle$	angle.
$\lim$	limit.
$\max$	maximum.

$\min$	minimum.
$\sup$	supremum, the least upper bound.
$\inf$	infimum, the greatest lower bound.
$\min$	designation the end of proofs.
$\mathbb{R}^n$	the n-dimensional Euclidean space.

Vectors and Matrices

$\|a\|$	the absolute value of a scalar a.
$\|x\|_p$	the induced p-norm of vector x, i.e. $\|x\|_p = (\|x_1\|^p + \cdots + \|x_n\|^p)^{1/p}$, $1 \leq p < \infty$; $\|x\|_\infty = \max_i \|x_i\|$.
$\|x\|$	the Euclidean norm of a vector x, i.e. $\|x\| = (x^{\mathrm{T}}x)^{1/2}$.
$\|A\|_p$	the induced p-norm of a matrix A, i.e. $\|A\|_p = \sup_{x \neq 0} \frac{\|Ax\|_p}{\|x\|_p}$.
$\|A\|$	the induced 2-norm of a matrix A, i.e. $\|A\| = [\lambda_{\max}(A^{\mathrm{T}}A)]^{1/2}$.
diag$[a_1, \cdots, a_n]$	a diagonal matrix with diagonal elements a_1 to a_n.
$A^{\mathrm{T}}(x^{\mathrm{T}})$	the transpose of a matrix A (a vector x).
$\lambda_{\max}(P)(\lambda_{\min}(P))$	the maximum and (minimum) eigenvalues of a symmetric matrix P.
$P > 0 (P \geq 0)$	a positive definite (semi-definite) matrix P.

Chapter 1

Introduction

1.1 Background

1.1.1 VSC-HVDC systems

The fundamental changes in the generation of electrical power within recent decades raised the need of smarter and more flexible power grids for modern electrical power industry [1]. High voltage direct current (HVDC) technology has been regarded as an ideal supplement to existing AC power grids. DC is the form that as opposed to AC which enables electrons flowing through the circuit in one direction only. As a result, it does not generate reactive power. The first use of electric power transmission was in DC form in late 19th century. However, HVDC transmission did not make a modest beginning until 1954 [2]. The AC electrical power system has been the domination since the advent of the transformers and induction machines in around 1890. At that time, Teslas invention of the induction machine and advances in transformers meant that AC at the time offered too many advantages as shown below [2].

- In the 19th century, only transformers allowed efficient conversion between voltages. This permitted generation and load at low voltage, but transformation to high voltage for efficient long-distance transmission. This situation remained largely unchanged until that mercury arc based converters became sufficiently advanced in the 1950s.

- AC currents are easier to interrupt since they fall to zero twice per electrical cycle. A circuit breaker can therefore switch off at zero, or nearly zero, current making them cheaper and more compact.
- DC machines require brushes; induction machines do not. Induction machines have gone on to become the dominant electrical load.

Nevertheless, the acceptance and dominance of AC systems still can not eclipse the distinct advantages of DC systems. For power transmission systems via overhead lines, they have primarily inductive characteristics. For the overhead line which is longer than 200 km, voltage drop and phase shift due to the inductance need to be overcome [3]. Flexible alternating current transmission systems (FACTS) are installed for solving this problem. HVDC transmission system is more economical because there is completely no line capacity wasted on transmitting reactive power and then no requirement on periodic reactive power compensation. Meanwhile, the losses of a DC line are smaller than the losses of an AC line due to high voltages and thus lower currents. For environmental consideration, a single HVDC line with two conductor bundles certainly has less environmental impact than a double circuit HVAC line with six conductor bundles since one bipolar HVDC overhead line has the same capability as a double circuit AC line [3]. Therefore, the same power can be transmitted over fewer transmission lines than would be required using AC, so less land is needed to accommodate the lines. HVDC technology induces minimal magnetic fields, so the power lines may be safely built closer to human habitation. Hence HVDC technology is capable of transmitting more power for a given transmission corridor size than conventional HVAC system. Where space is constrained, this may mean that, in future, HVAC lines may be replaced by HVDC. This has been the case in Germany for the Ultranet project [4]. Other examples for this type of HVDC connection are DC links directly into the downtown area of large cities like New York (Hudson Project) and San Francisco (Transbay Cable) [2].

For transmitting electrical power via submarine cables or underground cables which have primarily capacitive characteristics, HVDC technology is technically and economically feasible. Since a conventional AC transmission system generates more reactive power than it consumes with the cable length increasing, it requires

a corresponding reactive current to charge and discharge the cable as the grid voltage polarity changes. Both active and reactive current take the thermal capacity of the cable. Due to the extremely high reactive power exchange, AC cable transmission links have a maximum practical length of 100 km. Because the DC link does not generate reactive power as mentioned above, there is no technical limits to the potential length on HVDC cable which cause HVDC technology the only viable technical transmission alternative for distant cable links.

Besides, being built in point-to-point schemes for electric power transmission, HVDC systems are also being built in back-to-back scheme for interconnection of power systems. HVDC systems have already been widely applied to connecting unsynchronized AC networks or AC networks of different frequencies like 50 Hz and 60 Hz in Japan and South-America. HVDC technology is attracted for acting as frequency and phase conversion in Europe such as HVDC connections between the United Kingdom and Continental Europe, where two systems operate at 50-Hz nominal frequency but are not synchronized. HVDC systems can also provide a firewall to prevent disturbances propagating from one network to another and thus they are installed for the place that needs to be connected without increasing AC fault level. This was one of the reasons of installing ABB Mackinac converter project in Michigan [5].

During the time between 1890s to 1930s when AC form has already dominated the electrical power system, HVDC systems were still used in a number of installations of connecting two AC networks which were unsynchronized or owing different frequencies. These HVDC systems used the Thury systems where voltage conversion was accomplished by back-to-back motor-generator sets. However, the rotating machinery required high maintenance and had high energy loss. Various electromechanical devices were tested during the first half of the 20th century with little commercial success. The Moutiers-Lyons line was the most powerful system which running from 1906 to 1936 in France, over at a distance of 200 km at 75 kV with a current of 150 A (or about 22 MW) [2]. By the 1930s, the concept of rectification with a mercury arc, demonstrated in 1902 by Peter Hewitt , had reached a level of development and be used with moderate power AC to DC to AC conversion

systems. Then in the 1930s and 1940s, Uno Lamm and his team at ASEA (now part of ABB) improved the mercury arc rectifiers capability and built the first modern commercial HVDC system, the 20-MW, 98-km, 100-kV system linking the island of Gotland and the Swedish mainland. From the early 1970s onwards, mercury arc rectifiers started to be replaced by thyristor valves, which had matured as a technology from their introduction in the 1950s [2]. As solid-state devices, they did not suffer the material deposition problems that mercury arc devices did, which limited mercury arc device voltage, and required considerable maintenance. Thyristors which unlike mercury arc converters also do not suffer from operational problems such as arc-backs. Both mercury arc rectifiers and thyristors can delay turn-on of their valves but actually require the assistance of the AC grid to commutate (switch) from one valve to another. Since they are line-commutated converters (LCCs), this places minimum strength requirements on the AC grid to which they are connected. Their operation can be considered to be a DC source, switched between AC phases by the combined action of the AC grid and thyristor control, hence also the name current source converters (CSC). Insulated gate bipolar transistors (IGBTs), and other self-commutating high-voltage high-current semiconductor switches, have led to the rise of voltage-source converter (VSC) HVDC technology. VSC-HVDC technology which is known as HVDC Light (ABB), HVDC Plus (Siemens) and HVDC Flexible (China) is utilizing state-of-the-art power electronics device which can be fully controlled, unlike LCC-HVDC which is known as HVDC Classic. The VSC-HVDC technology is experiencing rapid development. According to an industry report in 2015 [6], the market has already been split roughly equally between CSC and VSC. Conventional CSC-HVDC transmission using line-commutated thyristor valves has higher power rating and is capable of very high transmission voltage. The principal development of LCC over the last two decades has been in the increase of operational voltage and power [2]. It is also characterized by higher transmission efficiency. Due to the low degree of controllability, lack of black start capability and reactive power consumption in converter, however, weak networks cannot be connected to this system. Extra AC series capacitors have been proposed to help CSC-HVDC operate with weak systems (the so-called capacitor-commutated converters)

and have been used in two back-to-back projects (Garabi in Brazil-Argentina, 2002, 2000 MW $\pm$ 70 kV and Rapid City, 2003, 200 MW, $\pm$ 13 kV) [2]. VSC-HVDC transmission, on the other hand, is available only for lower transmission voltage levels and power ratings. It is more expensive and has higher losses, which are related to the switching behavior and frequency of the self-commutated devices. However, VSC-HVDC owns the characteristics that make it very suitable for the connection of large offshore wind farms, such as fast control of active and reactive power independently from one another, capability to support the system in major contingencies, black start capability, possibility of connection to weak or even passive networks, capability to reverse the power flow direction almost instantaneously, etc. Additionally, new soft-switching methods and higher level topologies for VSC-HVDC can significantly reduce the converter losses and make this kind of transmission more economical and reliable [53]. VSC-HVDC can provide a variety of power quality support functions which meet the crucial demand of the modern electric power system especially with integration of variable renewable generation. Reactive power support, AC voltage control, and black-start functionality are provided in ABBs Mackinac project [5]. Other functions are also provided like firewalling one AC system so that disturbances will not spread to an adjacent system; providing frequency stabilizing functions and artificial fast frequency response (also called artificial inertia, as implemented in the Caprivi Link project); providing power oscillation damping (such as implemented in the Pacific DC Intertie, INELFE, BritNed, ATCO, WATL projects) [7]. Integrated and reliable transmission networks are the crucial prerequisite for developing integrated energy markets, enhancing the security of power supply, enabling the integration of renewable energy sources, and increasing energy efficiency. VSC-HVDC technology has been selected for a number of transmission projects which aimed at interconnecting European energy markets by means of undergrounding, integrating remote renewable energy sources such as offshore wind farms which strives to further decarbonize our environment. As mentioned above a number of advantageous integration and control features are provided with VSC-HVDC systems, the stabilized grid can be achieved with large shares of volatile generation in the power networks.

VSC-HVDC technology provides additional controllability to network operators to support efficient management on facilitate energy sharing and trading by interconnecting energy markets. Integration of the highly flexible VSC-HVDC directly as part of the smart grid architecture especially in unbundled markets with a high penetration of renewable sources enable operators to value new ancillary services to manage variability in power flows. As current and voltage capabilities of VSCs have increased significantly during recent years, additional functionality could be carefully coordinated for electric power markets to match the converters real power import and export capability.

HVDC technology is an effective and economic solution to a number of problems in existing power network which is verified by many years of successful operational experience of HVDC projects. Both LCC and VSC HVDC technologies are still developing rapidly, and corresponding improved solutions are being proposed by a number of manufacturers for their promising prospects. Therefore, VSC-HVDC system provides highly flexibility in modern power systems and undergo with rapid development in the forthcoming future.

1.1.2 HVDC converters

HVDC technology is in the stage of rapid development, great progress has been made especially in the HVDC converters over the last two decades. LCC is still being widely used for its high power capability as shown in Fig. 1.1 for comparison with VSC.

Nowadays, the demand for electricity in load centers is increasing, but the bulk of the energy resources built for satisfying rising demand are located remote from the load centers. The principal development of LCC has been in the increases of the operational voltage and power to provide enhanced performance for point-to-point bulk power transmission solution.

Although previous projects have used $\pm$ 600 kV (Itaipu1 and 2, each 3150 MW), most projects among them in previous decades had limited themselves to $\pm$ 500 kV (e.g., Three-Gorges and Gui-Guang in China or the East-South Interconnector in India in the first decade of the 21st century). In 2010, a new upper voltage level of 800

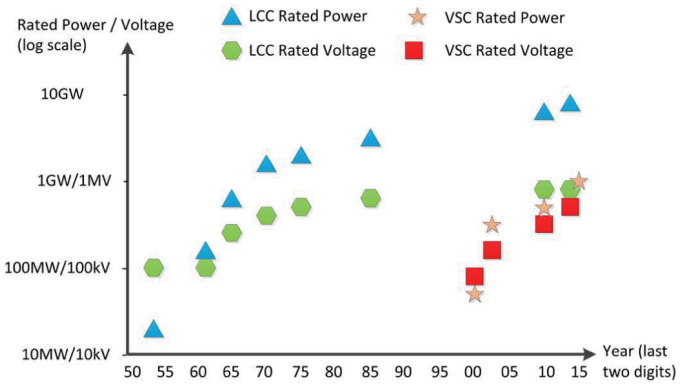

Figure 1.1: Progression of voltage and power ratings for LCC and VSC HVDC [2].

kV was set with the Siemens Yunnan-Guangdong 1418-km, 5000-MW project and the ABB Xianjiaba-Shanghai SGCC Project, China 1980-km, 6400-MW project. The inauguration of the Hami-Zhengzhou HVDC line raised this to 8000 MW at $\pm$ 800 kV over 2210 km. This step in voltage was economical for the increased power requirement (5000 MW or more) and distance covered (more than 1000- 2500 km) [2].

At the meantime, there is vast technology evolution in VSC-HVDC systems over last two decades besides significant increase on current and voltage capabilities of VSCs. VSC-HVDC technology was emerged by the advent of self-commutating power semiconductor in the 1990s which terminated the domination of CSC which makes the use of naturally commutated devices in HVDC application [8].

The full controllability and switching symmetry through both turn-on and turn-off operation of self-commutating semiconductor switches like IGBTs allows the device to regulate power flow extremely rapidly comparing with classic technology. The utilization of solid-state devices virtually eliminates the risk of commutation failure. In addition, VSC technology has the ability to absorb and generate active and reactive power which also are controlled independently of one another. This eliminates the demands for extra expensive reactive power compensators which has been used extensively within classic HVDC projects. Besides, there is no requirement for regulation of the short-circuit level since that the commutation process is operated without an AC system voltage source. Furthermore, the size and capac-

ity of corresponding filters can be effectively reduced since that the generation of harmonics is effectively reduced. The blackstart support can also be offered with applying VSCs which restoring power without the help of an external power source. This is especially advantageous ability in a wide area power outage and helps the progressive resurrection of the whole power grid [1].

The ratings and applications have progressed rapidly. The first commercial VSC-HVDC was built in 1997 at Gotland (50 MW, $\pm$80 kV, 70 km). The power has risen to 2000 MW (INELFE project between France and Spain) and a voltage of 500 kV (Skagerrak 4 project between Norway and Denmark) [2] during previous two decades. Many decisions of the early installations of VSC-HVDC were influenced by the desire to minimize the environmental impact and the need to manage and minimize potential power quality issues on the AC side. Low-profile stations, fed by cables, with self-commutating VSC, producing low amounts of low frequency harmonics were a clear advantage in 1990s for VSC-HVDC technology.

The first VSC-HVDC offshore converter station was installed in 2005 for connecting the Troll A oil platform (44 MW, $\pm$ 60-kV DC, 70 km). The original motivations for adopting VSC-HVDC technology were its significantly smaller footprint than LCC which is ideally suited for offshore applications and the fully controllability of the converter also makes it highly suited to weaker grids [2]. Following on from the success of the Troll offshore platform, the utility TenneT and the German government have pioneered the development offshore connection of offshore wind farms through VSC-HVDC transmissions . The Energiewende which is the planned energy transition in Germany provided a stable investment climate for renewable sources and corresponding power networks. Aa a result, over 4 GW of VSC-HVDC transmission has been installed to allow offshore renewable energy to be fed to mainland Germany.

The installations of five offshore VSC-HVDC connections in 2015 shown in Table 1.1 displayed that the VSC-HVDC is now a well-proven solution for offshore wind farms.

Table 1.1: Five offshore VSC-HVDC projects in 2015 and their basic parameters [2]

Project Name	Year of Commission	Power Rating	AC Voltage	DC Voltage	Length of DC Cables	Supplier
BorWin2, Germany	2015	800 MW	155 kV-BorWin Beta platform 380kV-Diele	± 300 kV	125 km Submarine cables 75 km Underground cables	SIEMENS
DolWin1, Germany	2015	800 MW	155 kV-DolWin Alpha platform 380kV-Dörpen-West	± 320 kV	75 km Submarine cables 90 km Underground cables	ABB
HelWin1, Germany	2015	576 MW	155 kV-HelWin Alpha platform 380kV-Büttel	± 250 kV	85 km Submarine cables 45 km Underground cables	SIEMENS
HelWin2, Germany	2015	690 MW	155 kV-HelWin Beta platform 380kV-Büttel	± 320 kV	85 km Submarine cables 45 km Underground cables	SIEMENS
SylWin1, Germany	2015	864 MW	155 kV-SylWin Alpha platform 380kV-Büttel	± 320 kV	159 km Submarine cables 45 km Underground cables	SIEMENS

In a classic HVDC multi-terminal system, reversing the power flow direction on a certain branch requires the power flow direction reversal on the other branches including the reversal of polarity of the converters. The complexity is that this introduces into multiterminal operation has limited the widespread use of multi-terminal systems (MTDC) [9]. This is the reason that why the HVDC with LCC has largely been selected as a point-to-point solution but have been few applied multiterminal installations [2]. Only two multiterminal schemes are carried out before 2015, with a tapping connection on the DC system. The notable projects are the links from Hydro-Quebec to New England (1990) and the connection between Italy, Corsica, and Sardinia (1989), which are in operation, both with three terminals. After more than 20 years, a new multi-terminal LCC-HVDC system called NEA (800 kV, 6000 MW, 1728 km) between Biswanath-Alipurduar-Agra, is under construction in India and was expected to be fully commissioned by 2016. However, in 2015, only one pole was in operation. The system comprises four terminals located at three con-

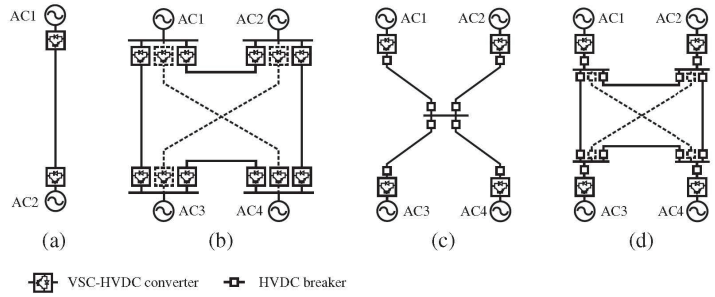

Figure 1.2: VSC-HVDC configurations: (a) point-to-point HVDC; (b) MTDC based on point-to-point links; (c) radial MTDC grid; (d) meshed MTDC grid; [9].

verter stations with a 33% continuous overload rating which is designed to supply hydropower from the Northeast India [9].

Various configurations of HVDC systems are illustrated in Fig. 1.2. Most of the HVDC systems in operation, either CSC- or VSC-based technology, are of point-to-point type (Figure 1.2a). Theoretically, the AC nodes can be connected by several point-to-point links in a so-called multiple-pair configuration(Figure 1.2b). However, for technical and economic reasons, it is more effective to connect the lines on the DC side, forming an HVDC network (Figures 1.2c and 1.2d). The advantage is the reduced number of converters which results in reduced costs and power losses.

The VSC-HVDC technology is totally flexible when developing HVDC networks. Each VSC station can send/receive power or reverse the power flow direction while providing similar control only at the station involved during the transaction. With VSC technology, power reversal is achieved by reversing the direction of current flow while does not require any change to the polarity of the converter terminals. This opens up the possibility of designing multi-terminal systems and hence full meshed DC grids [9]

The first VSC HVDC multi-terminal network systems are the Chinese Nanao Island (2013) and Zhoushan (2014) VSC-HVDC systems. Nanao Island is a $\pm$ 160-kV three-terminal (200, 150, and 50 MW) collaboration between Rongxin Power Electronic, NR-Electric, and XiDian [35]. Zhoushan is a five-terminal (400, 300, and three times 100 MW) 200-kV system built by C-EPRI and NR Electric [2]. But both systems are radial networks.

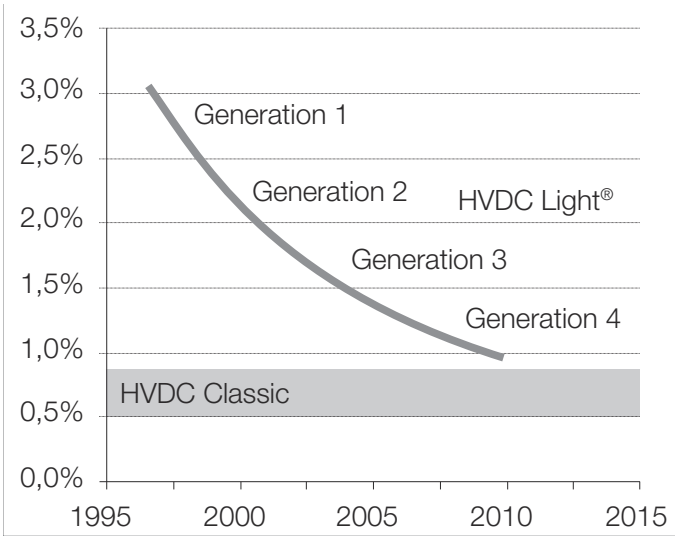

Figure 1.3: Losses for HVDC Light have decreased for each generation [10].

Initially, the prevailing VSC topology was the two-level converter and it is still the preferred solution for nowadays low-voltage applications. The two-level converter switches rapidly between the voltages at the upper and lower DC supply which uses pulse-width modulation (PWM). Only higher order switching harmonics need to be filtered, leaving a sinusoidal fundamental voltage at the point of connection, and drastically reducing the AC filter compared with LCC-HVDC. However, the losses is relatively high compared with classic HVDC shown in Fig. 1.3.

As shown in Fig. 1.3, the development of HVDC Light converter technology which was proposed by ABB has been going over 4 generations which also can be regarded as evolution of VSC-HVDC technology shown in Table 1.2. Generation 1 was a straight forward two-level converter switching the full voltage in a PWM pattern. Generation 2 was a three-level converter which used the neutral point clamped (NPC) topology in order to reduce the losses. However, more IGBTs were required and the cost was increased. Generation 3 was going back to a two-level converter with reduced number of IGBTs, but the subsequent improvement of two-level converter design and the use of optimum PWM (careful switching selection to reduce harmonics and third harmonic injection to boost DC voltage utilization) to continue reducing the losses [10]. The fourth generation of HVDC light converter is a Cas-

caded Two- Level (CTL) converter obtained by connecting several smaller two-level building blocks (cells) in series.

Instead, a transition to multilevel converter topologies offers better prospects for providing cost-effective power conversion at higher voltages. These topologies do not require direct series connection for increasing the operating voltage. Furthermore, the harmonic characteristics are well improved, so that the requirements on voltage and current distortion can be met without excessive switching losses [8].

In 2010, Siemens proposed a modular multilevel converter (MMC) design based on the work of Marquardt and named as HVDC Plus [2]. Then, the fourth generation of HVDC Light converter was proposed by ABB with CTL converter which is another type of MMC.

Table 1.2 displays the evolution in converter technology used in a selection of commercial projects: from two-level and three-level NPC towards multilevel converters.

Table 1.2: Development of VSC-HVDC technology and related parameters [2]

Project Name	Year of Commission	Power Rating	Converter Losses	Switching Frequency	Technology Name and Supplier	Topology
Gotland HVDC Light, Sweden	1997	50 MW	3%	1950 Hz	HVDC Light Gen. 1st ABB	2-level
Eagle Pass, USA	2000	36 MW	2.2%	1500 Hz	HVDC Light Gen. 2nd ABB	3-level Diode NPC
MurrayLink, Australia	2002	220 MW	1.8%	1350 Hz	HVDC Light Gen. 2nd ABB	3-level Active NPC
Estlink,Estonia-Finland	2006	350 MW	1.4%	1150 Hz	HVDC Light Gen. 3rd ABB	2-level
Trans Bay Cable, USA	2010	400 MW	1%	<150 Hz	HVDC Plus SIEMENS	MMC
South West Link, Sweden	2016	2×720 MW	1%	<150 Hz	HVDC MaxSine GE / Alstom	MMC
DolWin2, Germany	2017	916 MW	1%	=>150 Hz	HVDC Light Gen. 4th ABB	CTL

1.1.3 Basic Concepts and Terminology Used in This Thesis

Definition of basic concepts and terminology used in this thesis

Advanced control

In control theory, advanced control refers to a broad range of techniques and technologies implemented within industrial process control systems. Advanced control methods are usually deployed optionally and in addition to basic process controls. Basic controls are designed and built with the process itself, to facilitate basic operation, control and automation requirements. Advanced controls are typically added subsequently, often over the course of many years, to address particular performance or economic improvement opportunities in the process [11].

Robust control

In control theory, robust control is an approach to controller design that explicitly deals with uncertainty. Robust control methods are designed to function properly provided that uncertain parameters or disturbances are found within some (typically compact) set. Robust methods aim to achieve robust performance and/or stability in the presence of bounded modelling errors[12].

Stability

In mathematics, stability theory addresses the stability of solutions of differential equations and of trajectories of dynamical systems under small perturbations of initial conditions. In dynamical systems, an orbit is called Lyapunov stable if the forward orbit of any point is in a small enough neighborhood or it stays in a small (but perhaps, larger) neighborhood. Various criteria have been developed to prove stability or instability of an orbit. Under favorable circumstances, the question may be reduced to a well-studied problem involving eigenvalues of matrices. A more general method involves Lyapunov functions. In practice, any one of a number of different stability criteria are applied [11].

Disturbance

In electrical power engineering, a disturbance is a temporary change in environmental conditions that causes a pronounced change in a power system like power outage.

Uncertainty

Uncertainty refers to epistemic situations involving imperfect or unknown information. It applies to predictions of future events, to physical measurements that are

already made, or to the unknown. Uncertainty arises in partially observable and/or stochastic condition in system. In the power system uncertainty especially refers to cable/line parameter uncertainty.

1.2 Literature review

1.2.1 Control Methods of MMC in VSC-HVDC Transmission Systems

For the requirements of stable operation of MMC in VSC-HVDC transmission system, multiple control objectives are required to be achieved simultaneously like output current regulation, submodule (SM) capacitor voltage control, and circulating ripple currents suppression [13].

Existing cascaded control strategies with multi-loop for MMCs are built to achieve those control objectives with relatively complex controllers, and controller parameter tuning is difficult for such highly nonlinear systems with highly coupled states due to the complexity of MMC internal dynamics [14].

Most commonly adopted control scheme in cascaded manner is first introduced by [15]. This control concept employs multiple control loops with conventional proportional-integral (PI) loops combined with a phase-shifted pulse width modulation (PSPWM) scheme to regulate the MMC output and internal dynamics. However, the ripples in the differential current, which are undesired and reduce the converter efficiency, can not be suppressed effectively by this approach. Various differential current control strategies [16, 17, 18] were proposed for second-order harmonic suppression. Multiple resonant controllers are proposed for dealing with harmonics under both symmetric and unbalanced load conditions [19, 20]. Plug-in repetitive controllers [21, 22] to eliminate multiple harmonics in the differential current of MMC systems.

The aforementioned control strategies are all based on cascaded structures with multiple linear PI or PR controllers. Although these controllers have been able to

control the internal dynamics, the highly nonlinear dynamics with wide range of operational points and strong coupling among its states necessitates more advanced control strategies. Recently, various model predictive control (MPC)-based control methods have been proposed and investigated, including direct and indirect model-based predictive control [23, 24, 25, 26]. However, the computational burden of digital controllers is highly related to the MMC model complexity and the number of submodules in the system. Hence the implementation of MPC based methods in real time is hindered by their substantial calculation requirements, especially in applications where a large number of voltage levels are required.

Feedback linearization based control strategy offers a global control consistency via full non-linearities compensation which is suitable for acquiring both excellent control performance and system stability in MMC systems. Linear input-output behavior of MMC internal dynamics can be achieved by performing an inputCoutput linearization, the order of the internal dynamics can be reduced compared to regarding currents or capacitor voltages as outputs [27]. And then improved feedback linearization based control strategy is developed [13] The above-mentioned nonlinear feedback designs neglect the consideration of the features of system that were inherently imposed by the physical structure and energy-dissipative nature. From the practical point of view, it is desired that one can take advantage of these intrinsic physical properties of the system dynamics in designing a proper controller for the purpose of stabilization and command tracking. Passivity-based control (PBC) provides a powerful tool to systematically analyse the essential physical property of engineering problems. It normally treats a dynamical system as an energy transmission device, while the controller is viewed as another energy exchanging device which enables the overall energy of the controlled system to be desirably reshaped, upon dynamical interconnection, such that a satisfactory closed loop system performance could be realised. Hence PBC brings robustness to 'energy-preserving' (i.e., passive) unmodeled effects and enhanced system damping performance compared with the previous model-based nonlinear controllers [28].

Test cases in [14] are adopted for dynamic performance comparison in simulation section.

1.2.2 Control Methods of the Typical Two-terminal VSC-HVDC Systems

Traditionally, control of the VSC-HVDC system utilizes a nested-loop d-q vector control (VC) approach based on linear proportional-integral (PI) methods [29], whose control performance may be degraded with the change of operation conditions as its control parameters are tuned from one-point linearization model [30]. As VSC-HVDC systems are highly nonlinear resulting from converters and also operate in power systems with modelling uncertainties, many advanced control approaches are developed to provide a consistent control performance under various operation conditions, such as feedback linearization control (FLC) [31], linear matrix inequality (LMI)-based robust control [32], adaptive backstepping control [33], and power-synchronization control [34]. However, these methods are inadequate to handle perturbations such as modelling uncertainties and time-varying external disturbances.

Based on the variable structure control strategy, sliding-mode control (SMC) is an effective and high-frequency switching control for nonlinear systems with modelling uncertainties and time-varying external disturbances. The main idea of SMC is to maintain the system sliding on a surface in the state space via an appropriate switching logic, it features the simple implementation, disturbance rejection, fast response and strong robustness [35]. While the malignant effect of chattering phenomenon can be reduced by self-tuning sliding mode [36], SMC has been applied on electrical vehicles [37], power converters [38], induction machines [39], wind turbines [40], ect. Moreover, a feedback linearization sliding-mode control (FLSMC) has been developed for the VSC-HVDC system to offer invariant stability to modelling uncertainties by [41]. Basically, SMC assumes perturbations to be bounded and the prior knowledge of these upper bounds is required. However, it may be difficult or sometimes impossible to obtain these upper bounds, thus the supreme upper bound is chosen to cover the whole range of perturbations. As a consequence, SMC based on this knowledge becomes over-conservative which may cause a poor tracking performance and undesirable control oscillations [42].

Test cases in [30] including active and reactive power tracking, AC bus fault,

system parameter uncertainties and weak AC gird connection are adopted for dynamic performance comparison in simulation section.

1.2.3 FRT Capability Enhancement Strategies for VSC-HVDC with Wind Farm Integrated

One inevitable challenge for VSC-HVDC transmission systems which applied for integrating offshore wind farm is the fault ride-through (FRT) capability which stipulated by grid codes [43]. FRT capability enables offshore wind farm to be remained connected during abnormal onshore AC grid conditions like voltage deviations [44]. Fig. 4.1 demonstrates an FRT time-voltage profiles set by the German Transmission and Distribution Utility (E.ON) regulation [45]. The FRT requirement is a broad category covering zero voltage ride-through (ZVRT), low-voltage ride-through (LVRT) and high-voltage ride-through (HVRT). The ZVRT and LVRT are the main investigation objectives in the thesis. Fig. 4.2 demonstrates the reactive current requirement for supporting grid voltage during grid failure according to German grid code [46]. Although FRT attracted many research works, most of them are mainly studying FRT capability of individual wind turbine and these proposed works all caused considerable efforts in large-scale wind farm which formed by huge amounts of wind turbine. Investigating FRT capability on VSC-HVDC transmission system is regarded as a smarter way. There are two major types of approaches to enhance the FRT capability, one for control improvement and the other one for hardware modification.

FRT capability can be enhanced by installing additional protection devices, such as DC choppers with braking resistors [51], flywheel energy storage system [47] and novel topology like nine switch converter [48]. Installing extra devices used for providing voltage compensation, energy consumption or storage are effective yet being limited by the high cost and heat dissipation capacity. These methods also bring the complicated control of energy storage circuits or novel converter. Another effective alternative putting forward to enhance the FRT of the HVDC is to modify the control strategies applied on the converters. In [49], fuzzy logic controller for

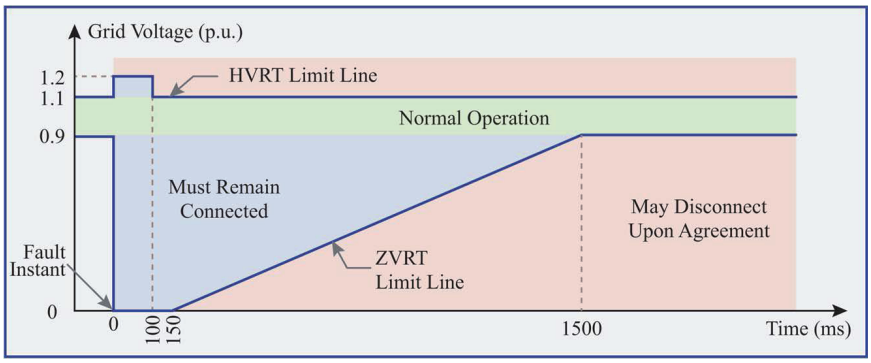

Figure 1.4: FRT profiles according to E.ON regulation [45]

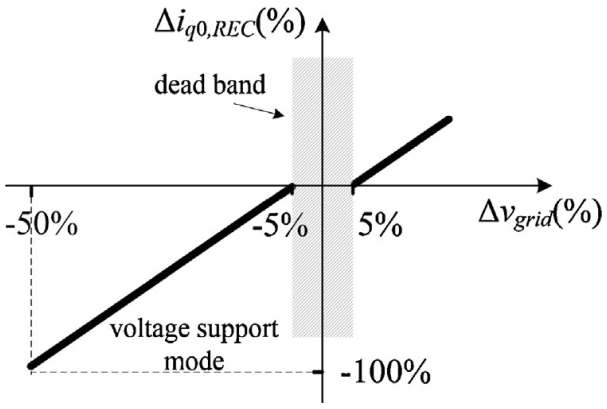

Figure 1.5: Required reactive current for voltage support according to German grid code [46]

temporary blocking the VSC converter is proposed during AC grid fault. However, even when the insulated gate bipolar transistors (IGBTs) in the sending-end VSC are blocked, the reverse current flowing via antiparallel diodes will still cause the power transmitting to the DC side [48]. Different control strategies are applied for power reduction (de-loading strategies) to enhance the FRT performance but are designed based on linear mode as mentioned in [50, 51, 52, 53]. However, existing linear approaches can not provide consistently satisfactory performance since that they are all tuned especially based on one operation point and the time-varying nonlinearities and uncertainties are not being fully compensated. Due to the poor off standard operation point behavior characteristics during AC network faults, inrush faulty grid-side current can not be limited rapidly and may cause converter components damaged since that the power electronics in the converter are very sensitive to transient current surges [54]. Feedback linearizing control (FLC) has been proposed in [54] for solving the nonlinearity problem to improve the FRT performance of individual wind turbine. However, the FLC requires the accurate system model and hence FLC will degrade dramatically in the presence of parameter uncertainties, and external disturbances which has adverse impacts on FRT performance. On the other hand, most FLC based controllers require full state feedback and many measured variables to calculate the nonlinear controller. Since co-operating with de-loading strategy will introduce more parameter uncertainties and disturbances caused by transients of slower mechanical response and can hardly provide real-time full state feedback, FLC is not suitable to be applied to this application. To improve these issues of the FLC, extended-order state and perturbation observer (E-SPO) based nonlinear adaptive controller is proposed to use the estimate of perturbation to compensate real perturbation and achieve the adaptive feedback linearizing control. A perturbation estimation based nonlinear adaptive control (NAC) scheme with proper de-loading strategy is developed for the FRT capability enhancement of VSC-HVDC systems. The combinatorial effect of nonlinearities, system parameter uncertainties and external disturbances is aggregated into a perturbation, which is estimated by a high-gain perturbation observer (HGPO) [55, 56, 57]. NAC is proposed to solve the nonlinearity problem and considered as the suitable method to

enhance the FRT capability with de-loading strategy. NAC-based VSC-HVDC converter controller only requires the measurement of active and reactive power and DC voltage, thus it provides the merit of inherently easy implementation in real systems.

Test cases in [51] are adopted for dynamic performance comparison in simulation section.

1.2.4 Coordinated Control Methods for VSC-MTDC with Wind Farm Integrated

Furthermore, the above applications are merely applied to two-terminal VSC-HVDC systems. In the multi-terminal VSC-HVDC (VSC-MTDC) system framework, not only the DC voltage and power transmission stability need to be self-controlled, but also an appropriate coordination among different terminals are needed for DC link cable line protection. Thus far, several coordinated control schemes have been developed for VSC-MTDC systems, such as adaptive droop control [58], which can share the burden according to the available headroom of each converter station. Meanwhile, an adaptive backstepping droop controller is proposed in [59], which can adaptively tune the droop gains to enhance control performances of traditional droop controllers by considering DC cable dynamics. Moreover, power-dependent droop-based control strategy is proposed in [60] so as to offer enhanced dynamic responses during AC/DC faults and large power scheduling changes.

The passivity-based control (PC) offers a power tool to exploit the physical property of a given engineering problem, upon energy interconnection and assignment, to achieve a satisfactory transient response with relatively fewer control efforts[61]. However, conventional PC [133] is highly sensitive to the uncertain system parameters and requires a detailed system model. To handle such issue, perturbation observer (PO) [57] is employed to estimate system state and perturbation term for nonlinear system, which can be represented as a chained-integrator system and matched nonlinearities and disturbances. Thus a perturbation observer based robust passivity-based control (PORPC) scheme is proposed for an N-terminal VSC-MTDC system, in which the combinatorial effect of interaction between different terminals, unmod-

elled dynamics and unknown time-varying external disturbances is aggregated into a perturbation, which is estimated online by a linear extended-state observer (ESO). Moreover, PORPC does not require an accurate VSC-MTDC model and only the D-C voltage, active and reactive power need to be measured. Furthermore, it provides a faster transient response with fewer control efforts as passivation [133] is adopted by the proposed approach to carefully reshape the system damping.

The DC link voltage droop controller with appropriate droop constant is required to be designed according to three-terminals radial VSC-MTDC model with wind farms and embedded into converter controller based on PORPC strategy of each terminal, which is not considered in the perturbation observer based passive controller design in [63]. This design can provide immediate corresponding response to the gird unbalance situation. PORPC also modified the parameters of the perturbation observer based passive control mentioned in [63] to improve corresponding robustness against unpredictable rapid-varying power fluctuation, system disturbance via considering wind turbine aerodynamics and weak grids characteristics which caused by wind farm integrating. Test cases in [58] including power regulation, AC bus fault, offshore wind farm integration, and weak power grids connection are adopted for dynamic performance comparison in simulation section.

The main contributions are summarized as follows:

1.3 Objectives and Motivations

VSC-HVDC systems is valuable for its multiple applications and being effective and efficient solutions for challenges which are faced by modern power grids. However, its valuable characterises can not be fulfilled to realize its originally designed application purposes for many reasons. Besides limited by its high cost and complexity, there is another serious obstacle due to the degraded control performance from equipped conventional controller at different system layers under varying operating performance and unexpected perturbations. It is because the process of power converting in VSC-HVDC system is highly-nonlinear and strong coupling

between each states. Thus the objective of the research work presented in this thesis is to improve the VSC-HVDC system dynamic performance and enable its functions better fulfilled in their designed applications via purposing advanced controllers at different layers of the VSC-HVDC system. Furthermore the conventional control strategies in existing equipped controllers at different layers of VSC-HVDC system are exposed the drawbacks that they lack the robustness against rapid time-varying disturbance and parameter uncertainties. Advanced control strategies are developed for solving the problems raised by the drawbacks of the existing controllers.

- The first objective of the research work presented in this thesis is evaluating the existing low-level controllers in MMC and propose the enhanced advanced controllers. PBC is developed and applied in chapter 2. In the VSC lower-level controllers, current regulation and arm-balancing control need to be investigated for they are essential to generate the gate switching signals. Gate switching signal directly affects the VSC-HVDC system and even the whole power systems. The wide application of MMC increased the complexity of the VSC topology and raised the challenges for the corresponding controller. Existing embedded low-level controller in converters can not meet the requirements of staying stable when the operation point varying largely due to fulfilling the flexibility of VSC-HVDC system in some applications.

- The second objective is comprehensively raising the robustness when operating point-to-point VSC-HVDC systems. The corresponding studying results of the proposed POSMC are presented in Chapter 3. There are massive operation requirements on adjusting power flow in power grids of different areas via VSC-HVDC system for realizing smarter grid. That exposes the challenges to providing satisfactory performance of power tracking, fault recovery responses. The conventional higher-level converter control strategies do not own enough robustness against time-varying modelling uncertainties and unexpected external disturbance. The SMC method is regarded to be an efficient method to possess strong robustness against system uncertainties. Considering uncertain system states and further enhance the system robustness

against rapid varying unmodelled dynamics, POSMC which adopting SM-SPOs for estimating uncertain system states and corresponding perturbations is proposed.

- The third objective is to enhance the FRT capability of the offshore wind farm which connected via VSC-HVDC system. Advanced control strategy with NAC is proposed and applied for FRT capability enhancement of the offshore wind farm, which is presented in chapter 4. Due to the unique characteristics of wind energy conversion systems, challenges are raised to control system in VSC-HVDC system when being applied to connect the offshore wind farm. One of the most important applications of VSC-HVDC system is renewable energy generation integration, especially offshore wind farms. Unlike conventional type 1 synchronous generator which directly connect to the grid, the renewable energy generation systems which uses asynchronous generators or frequency converters are referred to type 2 generating plants [46]. According to related grid code, in the event of faults in the grid outside the protection range of the generating plant, there must be no disconnection from the grid. A short-circuit reactive current must be fed into the grid during the period of a fault. VSC-HVDC system which owns fully-controllable devices when integrating renewable energy generation system is capable of improving the FRT capability of the latter.

- The fourth objective is better implementing the droop control strategy in VSC-MTDC system and improve corresponding control performance. The PORPC is proposed and being combined with the droop control strategy in chapter 5. Besides two-terminal point-to-point VSC-HVDC system has significant high application value, VSC-based MTDC system also has significant high application potentialities in modern power systems like embedding DC grid into current power system. Multiple practical applications have been implemented. Renewable energy sources have already been combined in the finished VSC-MTDC system projects. Coordinated control is essential to MTDC system for transmission line protection. Droop control strategy is designed for

appropriate load sharing which has been widely accepted and well proven. The challenges raised for better combining the droop control strategy with nonlinear advanced control theory which has already been applied for two-terminal point-to-point VSC-HVDC system.

1.4 Main Contributions

The contribution of research work presented in this thesis can be grouped as two parts: (a) Advanced control theory is developed and applied to build the advanced controllers for different layers in VSC-HVDC systems for ensuring global stability. and (b) There exist necessary control strategies which generating essential instructions for VSC-HVDC controllers in the large-scale power system. The advanced controller applied in VSC-HVDC system is modified for better realizing the coordination control purposes in various application conditions. The global system stability is also improved under different operating conditions. Main contributions are summarized as follows:

- Passivity is investigated in MMC current controller and one passivity-based control scheme is developed in chapter 2. For tracking the reference signals in the MMC, the proposed PBC can help to save control efforts greatly while ensuring the global stability of the whole system. The simulation results give the numerical data to verify the effectiveness of the proposed controller under testing dynamic-response with the steady-state and transient-state.

- One enhanced SMC is proposed and applied for two-terminal VSC-HVDC systems, which can greatly comprehensively enhance the robustness against variable disturbance occurring in the system. Modified SMO is adopted in the proposed POSMC to achieve the improved robustness in VSC-HVDC system. Simulation results of different cases like power tracking, LLLG faults, oscillations in weak grids and systems with parameter uncertainties verify that the proposed POSMC can provide excellent dynamic performance in VSC-HVDC system in all operation conditions. HIL test is carried out to validate the implementation feasibility of the proposed controller.

- One NAC-based de-loading strategy is proposed to enhance the FRT capability of VSC-HVDC system with offshore wind farm integration. During main grid fault ride-through process, the peak converter currents and DC link voltage are effectively suppressed via applying proposed control strategy. Simulation results and corresponding analysis provide the proper strategy design and effectiveness of the proposed FRT capability enhancement strategy. HIL test is carried out to prove the consistency with the simulation results. Hence the implementation feasibility of the proposed strategy is validated.

- PORPC is developed and designed with droop control strategy for the N-terminal VSC-MTDC system with the wind farm integration considered, which does not require an accurate system model thus a significant robustness against system uncertainties can be provided. Global stability can be ensured within a predetermined range of variation in system variables without further tuning. PORPC is proposed which basing on PBC for its energy cost saving since the operation points of MTDC system which integrating renewable energy source varies in relatively high frequency. Simulation results of different cases like power regulation, LLLG faults, oscillations in weak grids and output power variation in connected wind farm verify that the proposed PORPC can improve dynamic performance in VSC-MTDC system in all operation conditions. HIL test is carried out to validate the implementation feasibility of the proposed controller.

1.5 Publication List

The following publications linked to this thesis closely are listed as follows:

[1] **Y.Y. Sang**, B. Yang, W. Yao, and L. Jiang. "Design and implementation of perturbation observer based robust passivity-based control for VSC-MTDC systems considering offshore wind power integration," *IET Generation, Transmission & Distribution*. vol. 12, no. 10, pp. 2415-2424, 2018.

[2]B. Yang, **Y.Y. Sang**, K. Shi, W. Yao, L. Jiang, and T. Yu, "Design and real-

time implementation of perturbation observer based sliding-mode control for VSC-HVDC systems," *Control Engineering Practice*, vol. 56, pp. 13-26, 2016.

[3] **Y,Y. Sang**, B. Yang, and L. Jiang, "Nonlinear adaptive control design for the VSC-HVDC light transmission system," *UPEC 2015*, Staffordshire, UK, Sep. 1-4, 2015.

[4] B. Yang, L. Jiang, C.K. Zhang, **Y.Y. Sang**, T. Yu, and Q.H. Wu, "Perturbation observer-based adaptive passive control for nonlinear systems with uncertainties and disturbances," *Transactions of the Institute of Measurement and Control*. vol. 40, no. 4, pp. 1223-1236, 2018.

1.6 Thesis Outline

In this thesis, as shown in Fig. 1.6, control methods for single VSC converter in HVDC system are investigated and modified for dynamic performance improvement in Chapter 2. Then two-terminal point-to-point VSC-HVDC system are investigated and corresponding controllers are modified for dynamic performance improvement in Chapter 3. Offshore wind farm integration is considered into VSC-HVDC system in Chapter 4, corresponding controllers are modified for fault ride-though capability enhancement. VSC-MTDC with wind farm integration are investigated and corresponding controllers are modified for dynamic performance improvement in Chapter 5. This thesis is organized as follows:

Chapter 2: Passivity-based Current Control Design for MMC in HVDC Systems via Energy Shaping The complexity of MMC internal dynamics raised the severe situations for designing the corresponding controller. The existing cascaded control strategies based on classical linear control theory for MMCs achieve control objectives via requiring relatively complex structure and the controller parameter design is normally difficult for such highly nonlinear systems with highly coupled states. In view of this, advanced controllers are demanded in the regula-

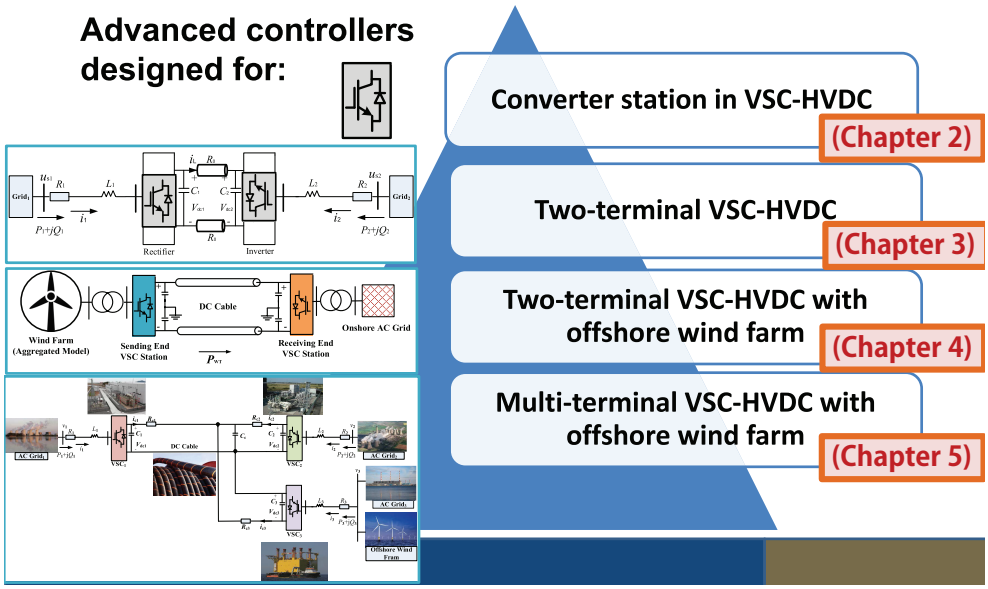

Figure 1.6: Configurations investigated in different chapters

tion tasks of MMC. Passivity is introduced in the MMC control system and PBC is proposed in chapter 2. PBC can provide extra damping to help energy saving via utilizing passivity in the system. A controllable decoupled form can be achieved after passivation output calculation. Well-tuned controllers are employed to regulate the output and inner differential currents of the MMC. Simulation results give the numerical data that showing the significantly improved steady-state and transient-state performances with greatly control costs saving.

Chapter 3: Perturbation Observer based Sliding Mode Control for Enhancing Dynamic Responses of VSC-HVDC Systems This chapter proposed an extended state observer based sliding-mode control scheme for VSC-HVDC systems. The combinatorial effect of nonlinearities, parameter uncertainties, unmodelled dynamics and time-varying external disturbances is aggregated into a perturbation, which is estimated online by an ESO called SMSPO. It does not require an accurate system model and only one state measurement is needed. As the upper bound of perturbation is replaced by the smaller bound of its estimation error, an over-conservative control input is avoided such that the tracking accuracy can be improved. Four case studies are carried out on the VSC-HVDC system, such as active and reactive pow-

er tracking, AC bus fault, system parameter uncertainties, and weak AC gird connection. Simulation results verify its superiority over vector control and feedback linearization sliding-mode control. Then a hardware-in-the-loop test is undertaken to validate the implementation feasibility of the proposed approach.

Chapter 4: Nonlinear Adaptive Control for Fault Ride-Through Capability Enhancement of VSC-HVDC Transmission Systems with Offshore Wind Farm Integration

This chapter proposes a perturbation estimation based nonlinear adaptive control for VSC-HVDC power transmission systems which are applied to interconnect offshore large-scaled wind farms to onshore main grid in order to enhance the fault ride-through (FRT) capability of Type-4 wind energy conversion systems (WECS). VSC-HVDC power transmission system is regarded as the favourable solution for interconnecting offshore wind farm. The rapid increasing adoption of this interconnection approach in industrial projects inspires investigating on VSC-HVDC power transmission system to improve the FRT capability of integrated WECS. Type-4 WECS is indicated that it will take over the wind energy market in coming years by the wind turbine manufacturers for the enhanced performance brought by full-scale (100%) power converters. To improve the FRT capability of offshore power plant, de-loading strategy is investigated with novel advanced control of the VSC-HVDC systems. The proposed NAC does not require the accurate model and full state measurements since combinatorial effect of nonlinearities, system parameter uncertainties and external disturbances are aggregated into a perturbation term, which is estimated online by a high-gain perturbation observer and being fully compensated. As proposed NAC is adaptive to system model uncertainties (e.g., mismatched output impedance of the converters and the line impedance of transmission line), time-varying disturbance (e.g., AC grid voltage sags and line to ground faults) and unknown time-varying nonlinearities of power electronic system (e.g., unmodelled dynamics existed in valves and VSC phase-locked loop system), a significant robustness can be provided with de-loading strategy to enhance the FRT capability. Simulation results show that the proposed strategy can provide better dynamic per-

formances in the cases of operation with a variety of reduced voltage levels and better robustness against model uncertainties and mismatched system parameters comparing with conventional vector control.

Chapter 5: Perturbation Observer based Robust Passivity-based Control for VSC-MTDC Systems

With the increasing penetration of renewable energy sources especially wind power, VSC-MTDC systems are starting to be commissioned. However, concentrated integration of large scale wind power demands stronger robustness against power fluctuation and system disturbances to increase the reliability of the whole system. This chapter proposes a perturbation observer based robust passivity-based control for VSC-MTDC systems connected to an offshore wind farm to meet the demands. The aggregated effect of system nonlinearities, parameter uncertainties, unmodelled dynamics and external disturbances includes grid faults and time-varying wind power output is estimated by a linear perturbation observer and fully compensated by a passive controller, thus no accurate VSC-MTDC system model is required. The proposed scheme attempts to regulate DC voltage and reactive power at the rectifier side, as well as active power and reactive power at the inverters side connected to an offshore wind farm. Besides, a DC link voltage droop controller is introduced so as to provide immediate load sharing arrangement which responses to the grid unbalance situation. Moreover, a noticeable robustness against parameter uncertainties can be achieved as no accurate system model is needed. Case studies are carried out to compare the performance of PORPC to other typical approaches. Lastly, a hardware-in-the-loop (HIL) test is undertaken via dSPACE simulators which validates its implementation feasibility.

Chapter 6: Conclusions and Future Works

This thesis is concluded with a summary of the obtained results and perspectives for future work. Future works presented in this chapter are focused on unsolved problems that remain in this thesis.

Chapter 2

Passivity-based Current Control Design for MMC in HVDC Systems via Energy Shaping

2.1 Introduction

MMC is regarded as the most promising converter topology for VSC-HVDC systems because of its high efficiency, modular design, easily scalable in terms of voltage and power, low distortion of output voltage and minimized filter design [64, 65, 66]. However, the design complexity of MMC systems has been expanded from the relatively simple topological configuration to the overall control strategy, which attracts considerable research interests in recent years [13]. Several control strategies based on classical linear control theory, e.g. proportional-integral (PI) and proportional-resonant (PR) controllers, have been proposed for MMC systems. However, more advanced control strategies are required due to the highly nonlinear dynamics of the MMC with a wide range of operational points and strong coupling among its states. Recently, various model predictive control (MPC)-based control methods have been proposed and investigated, including direct and indirect model-based predictive control [23, 24, 25, 26]. However, the computational burden of digital controllers is highly related to the MMC model complexity and the number

of submodules in the system. Hence the implementation of MPC based methods in real time are hindered by their substantial calculation requirements, especially in applications where a large number of voltage levels are required.

Feedback linearization based control strategy offers a global control consistency via full non-linearities compensation which is suitable for acquiring both excellent control performance and system stability in MMC systems, Linear inputCoutput behavior of MMC internal dynamics can be achieved by performing an inputCoutput linearization, the order of the internal dynamics can be reduced compared to regarding currents or capacitor voltages as outputs [27]. And then improved feedback linearization based control strategy is developed [13] The above-mentioned nonlinear feedback designs neglect the consideration of the features of system that were inherently imposed by the physical structure and energy-dissipative nature. From the practical point of view, it is desired that one can take advantage of these intrinsic physical properties of the system dynamics in designing a proper controller for the purpose of stabilization and command tracking. Passivity-based control (PBC) provides a powerful tool to systematically analyse the essential physical property of engineering problems. It normally treats a dynamical system as an energy transmission device, while the controller is viewed as another energy exchanging device which enables the overall energy of the controlled system to be desirably reshaped, upon dynamical interconnection, such that a satisfactory closed loop system performance could be realised. Hence PBC brings robustness to 'energy-preserving' (i.e., passive) unmodeled effects and enhanced system damping performance compared with the previous model-based nonlinear controllers [28].

This chapter proposed a passivity-based controller which has already successfully implemented in various industrial applications like induction motors [67], robot arms [28] and low-voltage/medium-voltage DC-to-DC converters [68, 69]. In the full operation range of the MMC, especially during large operation point step changes with balanced submodule capacitor voltage, the proposed passivity-based controller, compared to the other controllers provides a faster dynamic response and comparable steady state performance for MMC operation at rating since it can provide globally consistent control performance and extra damping effect-

s via passivation. Fast dynamic response is an important requirement for flexible application of MMC-based VSC-HVDC systems like renewable energy sources integration. Fast dynamic response is also required to guarantee stable operation of MMC-based VSC-HVDC systems in power system especially under fault conditions. Simulation studies in the Simulink software environment are carried out to validate the performance and effectiveness of the proposed control method in the MMC-based VSC-HVDC system.

2.2 State Functional Model of the MMC

The typical MMC-based VSC system shown in Fig.2.1 is adopted to demonstrate the proposed passivity-based current control strategy.

The MMC is comprised of *N* SMs per arm and it may include *M* redundant SMs per arm submodules connected in series in the upper and lower arms in one phase respectively. In practical application, there is normally using 10% redundant SMs for reliability improvement [70] but in this chapter $M = 0$. Each arm is equipped with an arm inductor L_{arm} to limit the arm currents in the events such as dc-link short circuit. An equivalent resistor R_{arm} is employed in each arm to represent the losses on the semiconductors, equivalent series resistance in C_{SM} and L_{arm}, etc.

Assuming the submodule capacitor voltages in one arm are perfectly balanced, the average capacitor voltages in the upper and lower arms can be denoted as u_{Cu} and u_{Cl} respectively. According to the average model of the MMC, the voltages and currents in the upper and lower arms can be expressed as follows:

$$\begin{cases} u_{\text{u}} = N u_{\text{u}} [\frac{1-u_{\text{o}}^*}{2} - u_{\text{diff}}^*] \\ u_{\text{l}} = N u_{\text{l}} [\frac{1+u_{\text{o}}^*}{2} - u_{\text{diff}}^*] \end{cases} \tag{2.2.1}$$

$$\begin{cases} i_{\text{u}} = i_{\text{diff}} + \frac{i_{\text{o}}}{2} \\ i_{\text{l}} = i_{\text{diff}} - \frac{i_{\text{o}}}{2} \end{cases} \tag{2.2.2}$$

where u_{o}^* and u_{diff}^* are the normalized output and differential voltage reference signals. i_{o} is the output current of the MMC, and i_{diff} is the inner differential current in

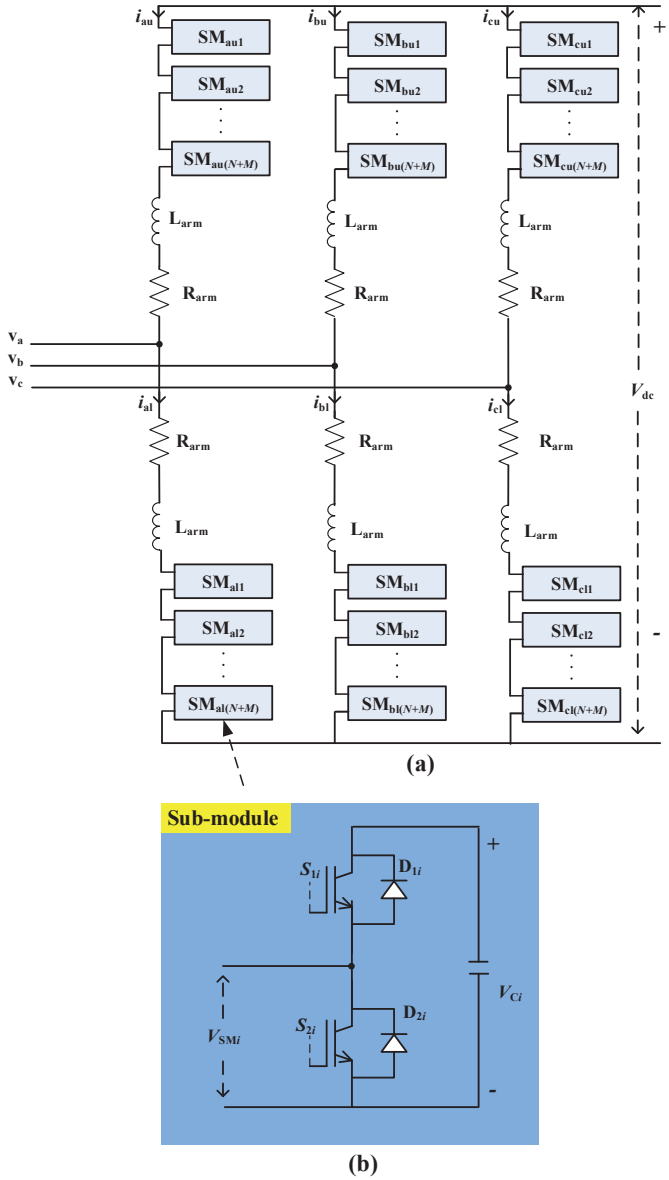

Figure 2.1: (a)Three-phase MMC topology; (b) Half-bridge circuit for the *i*th SM.

the phase leg. And the output voltage u_{o} of the MMC is expressed as:

$$u_{\mathrm{o}} = u_{\mathrm{load}} + L_{\mathrm{o}} \frac{di_{\mathrm{o}}}{dt} \tag{2.2.3}$$

where u_{load} and L_{o} are the equivalent voltage source of the load and the equivalent inductor connected to the the middle points of the two arms of the MMC. The DC voltage can be derived as follows:

$$\begin{aligned} U_{\mathrm{DC}} &= 2u_{\mathrm{u}} + 2R_{\mathrm{arm}} i_{\mathrm{u}} + 2L_{\mathrm{arm}} \frac{di_{\mathrm{u}}}{dt} - 2u_{\mathrm{o}} \\ &= 2u_{\mathrm{l}} + 2R_{\mathrm{arm}} i_{\mathrm{l}} + 2L_{\mathrm{arm}} \frac{di_{\mathrm{u}}}{dt} + 2u_{\mathrm{o}} \end{aligned} \tag{2.2.4}$$

Substituting (2.2.2) and (2.2.3) into (2.2.4), following equations can be obtained.

$$\begin{cases} \frac{di_{\mathrm{o}}}{dt} = \frac{-R_{\mathrm{arm}} i_{\mathrm{o}} - u_{\mathrm{u}} + u_{\mathrm{l}} - 2u_{\mathrm{load}}}{L_{\mathrm{arm}} + 2L_{\mathrm{o}}} \\ \frac{di_{\mathrm{diff}}}{dt} = \frac{-2R_{\mathrm{arm}} i_{\mathrm{diff}} - u_{\mathrm{u}} - u_{\mathrm{l}} + U_{\mathrm{DC}}}{2L_{\mathrm{arm}}} \end{cases} \tag{2.2.5}$$

According the equations mentioned above, i_{o} and i_{diff} can be controlled by adjusting u_{o}^* and u_{diff}^*. The submodule capacitors that are inserted into each arm will be charged or discharged by the arm current and can be calculated as follows,

$$\begin{cases} \frac{du_{\mathrm{Cu}}}{dt} = \frac{i_{\mathrm{u}}}{C_{\mathrm{SM}}} n_{\mathrm{u}} = \frac{i_{\mathrm{u}}}{C_{\mathrm{SM}}} \left(\frac{1 - u_{\mathrm{o}}^*}{2} - u_{\mathrm{diff}}^* \right) \\ \frac{du_{\mathrm{Cl}}}{dt} = \frac{i_{\mathrm{l}}}{C_{\mathrm{SM}}} n_{\mathrm{l}} = \frac{i_{\mathrm{l}}}{C_{\mathrm{SM}}} \left(\frac{1 + u_{\mathrm{o}}^*}{2} - u_{\mathrm{diff}}^* \right) \end{cases} \tag{2.2.6}$$

where the n_{u} and n_{l} represent the number of submodule inserted in up and low arm respectively and they are the actual control inputs for the MMC [13]. Hence the state functions of the MMC system can be obtained and the state variables are chosen as $x = [i_{\mathrm{o}} \ i_{\mathrm{diff}} \ u_{\mathrm{Cu}} \ u_{\mathrm{Cl}}]^{\mathrm{T}}$. The inputs of the system are chosen as $u = [u_{\mathrm{o}}^* \ u_{\mathrm{diff}}^*]^{\mathrm{T}}$ and the outputs of the system are chosen as $y = [i_{\mathrm{o}} \ i_{\mathrm{diff}}]^{\mathrm{T}}$ State functions of the MMC system can be derived as follows:

$$\begin{cases} \dot{x} = f(x) + g_{\mathrm{o}}(x) u_{\mathrm{o}}^* + g_{\mathrm{diff}}(x) u_{\mathrm{diff}}^* \\ y = h(x) \end{cases} \tag{2.2.7}$$

where

$$
\begin{aligned}
f(x) = &\begin{bmatrix} \frac{-2u_{\text{load}}}{L_{\text{arm}}+2L_{\text{o}}} & \frac{U_{\text{DC}}}{2L_{\text{arm}}} & 0 & 0 \end{bmatrix}^{\text{T}} \\
&+ \begin{bmatrix} \frac{-R_{\text{arm}}}{L_{\text{arm}}+2L_{\text{o}}} & 0 & \frac{-N}{2L_{\text{arm}}+4L_{\text{o}}} & \frac{N}{2L_{\text{arm}}+4L_{\text{o}}} \\ 0 & \frac{R_{\text{arm}}}{L_{\text{arm}}} & \frac{-N}{4L_{\text{arm}}} & \frac{-N}{4L_{\text{arm}}} \\ \frac{1}{4C_{\text{SM}}} & \frac{1}{2C_{\text{SM}}} & 0 & 0 \\ \frac{-1}{4C_{\text{SM}}} & \frac{1}{2C_{\text{SM}}} & 0 & 0 \end{bmatrix} \\
&\times \begin{bmatrix} i_{\text{o}} \\ i_{\text{diff}} \\ u_{\text{Cu}} \\ u_{\text{Cl}} \end{bmatrix}
\end{aligned}
\tag{2.2.8}
$$

$$
g_{\text{o}}(x) = \begin{bmatrix} \frac{N(u_{\text{Cu}}+u_{\text{Cl}})}{2L_{\text{arm}}+4L_{\text{o}}} & \frac{N(u_{\text{Cu}}-u_{\text{Cl}})}{4L_{\text{arm}}} & \frac{-2i_{\text{diff}}-i_{\text{o}}}{4C_{\text{SM}}} & \frac{2i_{\text{diff}}-i_{\text{o}}}{4C_{\text{SM}}} \end{bmatrix}^{\text{T}} \tag{2.2.9}
$$

$$
g_{\text{diff}}(x) = \begin{bmatrix} \frac{N(u_{\text{Cu}}-u_{\text{Cl}})}{L_{\text{arm}}+2L_{\text{o}}} & \frac{N(u_{\text{Cu}}+u_{\text{Cl}})}{4L_{\text{arm}}} & \frac{-2i_{\text{diff}}-i_{\text{o}}}{2C_{\text{SM}}} & \frac{-2i_{\text{diff}}+i_{\text{o}}}{2C_{\text{SM}}} \end{bmatrix}^{\text{T}} \tag{2.2.10}
$$

$$
h(x) = \begin{bmatrix} 1 & 0 & 0 & 0 \\ 0 & 1 & 0 & 0 \end{bmatrix} x \tag{2.2.11}
$$

2.3 PBC Design for the MMC

2.3.1 Passivity-based Control with Energy-reshaping

Consider a normal system as follows

$$
\begin{cases} \dot{x} = f(x,u) + \bar{B}u + \zeta(t) \\ \dot{y} = h(x,u) \end{cases} \tag{2.3.1}
$$

where the output $x \in \mathbb{R}^m$ and control input $d \in \mathbb{R}^m$, such that considering system (2.3.1) is of the vector relative degree of one. $f(x,u) \in \mathbb{R}^m$ is considered as being nonlinear which consists of the structure with parameter uncertainties, $\zeta(t) \in \mathbb{R}^m$ is the time-varying external disturbance. $h(x,y)$ is a known smooth function of

dimension $(n-m)\times m$. The unknown control gain $\bar{B}\in\mathbb{R}^{m\times m}$ is written as

$$\bar{B}=\begin{bmatrix} b_{11}(x,y) & \cdots & b_{1m}(x,y) \\ \vdots & \vdots & \vdots \\ b_{m1}(x,y) & \cdots & b_{mm}(x,y) \end{bmatrix} \tag{2.3.2}$$

The energy balance equations of the system can be considered as

$$\underbrace{\mathcal{H}_x(T)-\mathcal{H}_x(0)}_{\text{stored energy}}+\underbrace{\int_0^T f_{\mathrm{d}}(x)\mathrm{d}t}_{\text{dissipated}}=\underbrace{\int_0^T f_{\mathrm{s}}(x)\mathrm{d}t}_{\text{supplied}} \tag{2.3.3}$$

where $H_x(t)$ is the stored energy function, and $f_{\mathrm{d}}(x)$ and $f_{\mathrm{s}}(x)$ are a non-negative functions that represent the energy dissipation, e.g., due to resistances or friction-s, etc. System considered is defined to be output strictly passive if there exists a continuously differentiable positive semi-definite function $H_x(T)$ called the storage function) such that

$$u^{\mathrm{T}}y\geq\frac{dH_x}{dx}+\xi y^T y,\qquad\forall(x,u)\in\mathbb{R}^n\times\mathbb{R}^m \tag{2.3.4}$$

where $\xi>0$. In order to obtain the asymptotic stability the following lemma is needed. The system (2.3.1) is assumed and zero-state detectable and locally weak-ly minimum-phase. Hence the origin of the uncontrolled system is asymptotically stable with a positive definite storage function. Moreover, if the storage function is radially unbounded then the origin is globally asymptotic stable [21]. If the sys-tem is not strictly passive but there exists a positive definite storage function and a feedback control law $u=\beta(x)+v$ such that $\dot{H}\leq vy$ the feedback system is passive. The process is called as feedback passivation and $v=-\phi(y)$ where $\phi(y)$ is sector-nonlinearity and it meets $y\phi(y)>0$ for $y\neq 0$, $phi(0)=0$. Therefore $\dot{H}\leq -y\phi(y)\leq 0$.

2.3.2 Proposed Passivity-based Current Control in MMC

For introducing the passivity into MMC control, the calculating passive output y is necessary via defining the storage function $H(x)$.

$$y=\begin{bmatrix} x^{*\mathrm{T}}g_{\mathrm{o}}(x)^{\mathrm{T}} \\ x^{*\mathrm{T}}g_{\mathrm{diff}}(x)^{\mathrm{T}} \end{bmatrix} f_H(x) \tag{2.3.5}$$

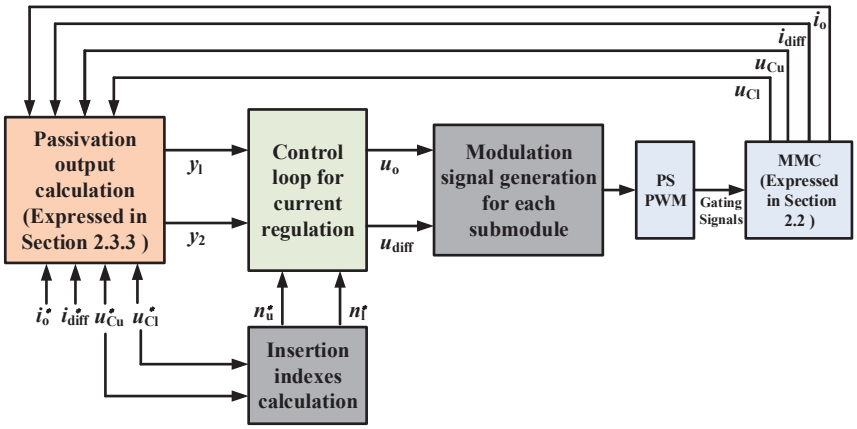

Figure 2.2: Block diagram of the proposed control system for the MMC system.

where x^* is the corresponding reference signals of the x and the $f_H(x)$ is the derived from $f(x)$ which removing the effects of dissipation and supplies which can be expressed as;

$$f_H(x) = \begin{bmatrix} 2L_{\text{arm}} & 0 & 0 & 0 \\ 0 & \frac{L_{\text{arm}}}{2} + L_{\text{load}} & 0 & 0 \\ 0 & 0 & \frac{2C_{\text{SM}}}{2} & 0 \\ 0 & 0 & 0 & \frac{2C_{\text{SM}}}{2} \end{bmatrix} \times \begin{bmatrix} i_{\text{o}} \\ i_{\text{diff}} \\ u_{\text{Cu}} \\ u_{\text{Cl}} \end{bmatrix} \tag{2.3.6}$$

The proposed current controller for system using the passivation is designed as

$$\begin{cases} u = u^* - K_1 y - K_2 z \\ y = \dot{z} \end{cases} \tag{2.3.7}$$

where

$$u = \begin{bmatrix} u_{\text{o}} \\ u_{\text{diff}} \end{bmatrix}, u^* = \begin{bmatrix} n_{\text{u}}^* + n_{\text{l}}^* \\ n_{\text{u}}^* - n_{\text{l}}^* \end{bmatrix} \tag{2.3.8}$$

where K_1 and K_2 are the feedback control gains which place the poles of the closed-loop system in the left-half plane (LHP) and are tuned for system global stability for all operation points. $n_{\text{u}}^* = \frac{\frac{V_{\text{DC}}}{2} - e_v^* - u_{\text{diff}}^*}{U_{Cu}^*}$, $n_{\text{l}}^* = \frac{\frac{V_{\text{DC}}}{2} + e_v^* - u_{\text{diff}}^*}{U_{Cl}^*}$ where e_v^* is the internal e.m.f. voltage of the MMC.

The whole proposed MMC current control system is illustrated as Fig.2.2

2.4 Case Studies

The proposed PBC is applied on the MMC mentioned in Section 2.2. The control performance of proposed PBC strategy is evaluated under various operating conditions in a wide neighbourhood of the initial operating points and compared to that of conventional control and FLC used in [13]. The system parameters used in the simulation are listed in Table 5.1.

Table 2.1: System parameters used in the MMC system.

Rated AC-bus frequency	f	50 Hz
DC-bus voltage	$V_{\mathrm{DC}_{\mathrm{base}}}$	200 kV
DC-bus capacitance	C_{DC}	4 mF
Output inductance	L_{o}	0.7 mH
No. of SM in each arm	N	3
Arm inductance	L_{arm}	5 mH
Arm resistance	R_{arm}	0.03 Ω
SM capacitance	C_{SM}	900 μF

The steady-state performance of the MMC regulated by the proposed PBC control is investigated. The amplitude of the output current is set as 9 A in the steady-state performance. The steady-state performance of the MMC regulated by the proposed PBC is illustrated in Fig. 2.3. It can be seen that the output currents are well regulated with the help of the proposed nonlinear control method and the MMC operates stably. From Fig. 2.4, the capacitor voltage is well stabilized.

For comparison, the tracking error of current waveforms of the MMC under the conventional cascaded control strategy, FLC proposed in [13] and proposed PBC is shown in Fig. 2.5. It is obviously that the FLC and PBC is able to achieve almost the same excellent output current tracking accuracy (peak-to-peak tracking error is less than 0.07 A) than that of the conventional control strategy due to nonlinearity con-

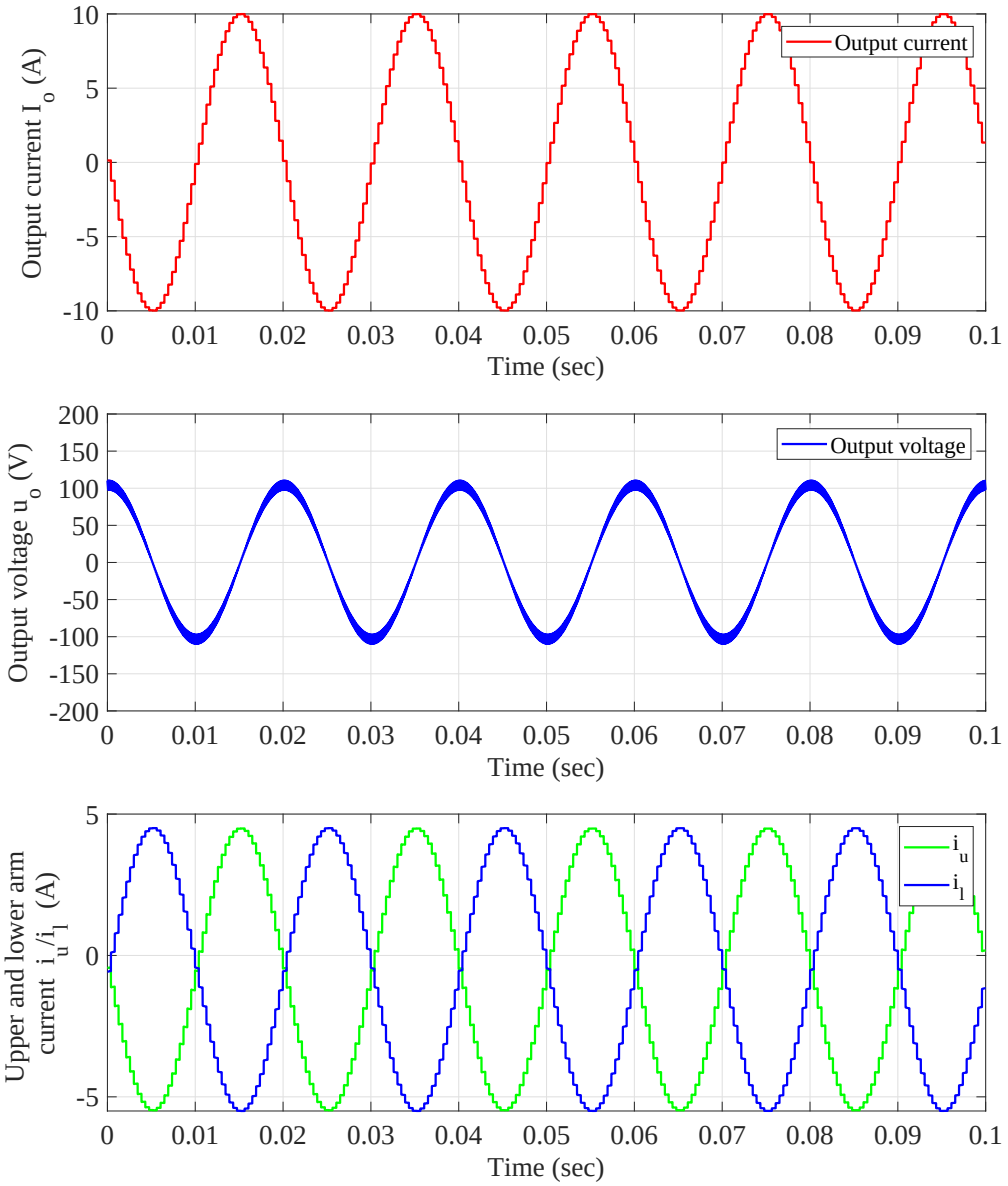

Figure 2.3: Voltage and current waveforms of the MMC regulated under steady state conditions.

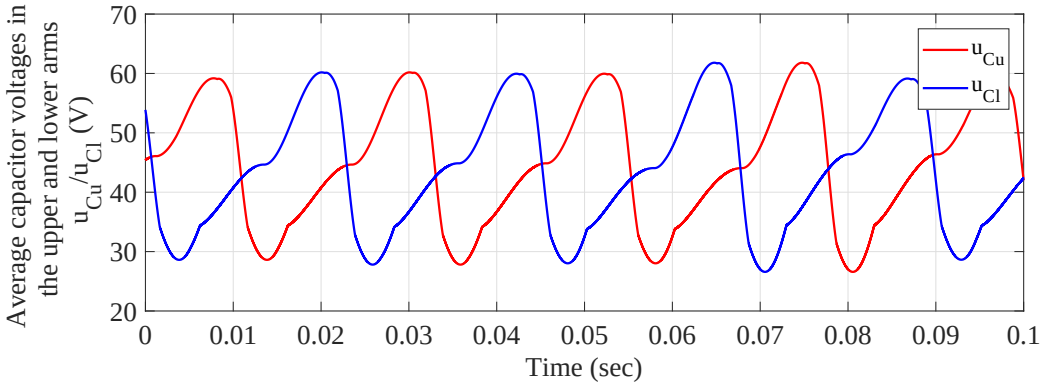

Figure 2.4: The average capacitor voltages in the upper and lower arms voltage waveforms of the MMC regulated under steady state conditions.

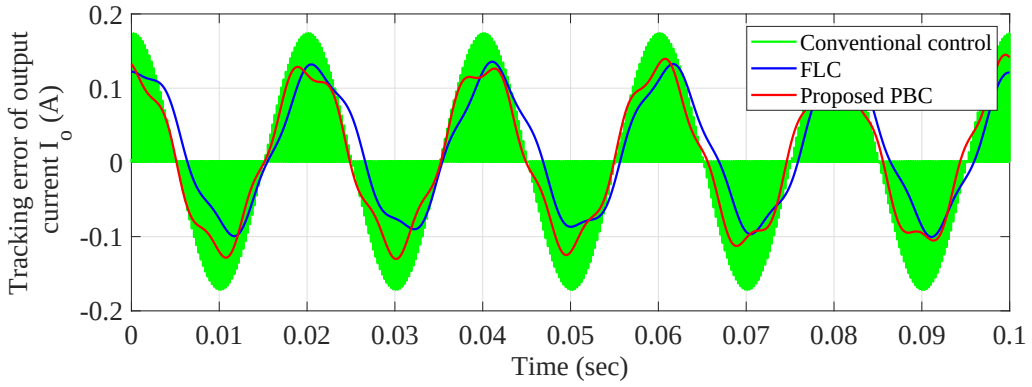

Figure 2.5: The waveform of tracking error of output current obtained from the conventional control strategy, FLC proposed in [13] and proposed PBC.

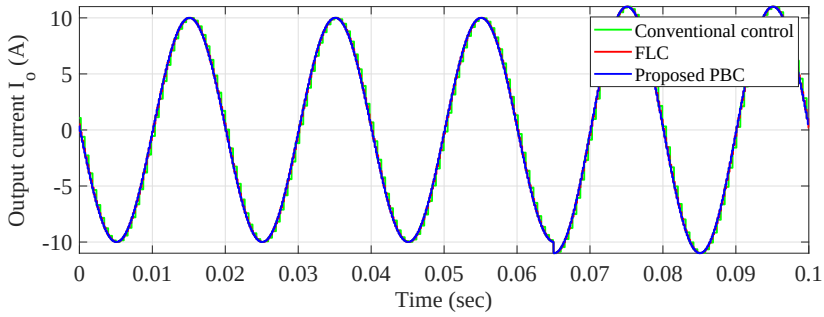

Figure 2.6: The waveform of output current obtained via applying the conventional control strategy, FLC proposed in [13] and proposed PBC when reference signal raised at 0.065s.

sideration. The high-frequency chatting error is easily introduced by conventional control due high sampling frequency of the generated reference signals. For evaluating the dynamic response performance of the MMC, the amplitude of the reference current signal is raised by 10% at 0.065s. The waveforms of the output current regulated by different control strategies is displayed in Fig. 2.6. It can be seen that the dynamic responses obtained via different control strategies are almost similar. For further evaluating the control performance of different control strategies with numerical data, absolute error (IAE) index is introduced. Here $\text{IAE}_x = \int_0^T |x - x^*| \mathrm{d}t$ and x^* is the reference value of the variable x. The simulation time $T = 0.2$ s. The results are presented in Table 2.2. Note that the proposed PBC can provide pretty excellent performance comparing with conventional control and FLC especially when suppressing unwanted fluctuation in differential currents. The IAE of the proposed PBC is only 26.1% and 32.4% of the conventional control and FLC.

The overall control efforts of different approaches can also be evaluated by IAE index where $\text{IAE}_u = \int_0^T |u| \mathrm{d}t$. In the investigated target, the action of a controller can be understood in energy terms as another dynamical system typically implemented in a computer-interconnected with the process to modify its behavior. The control problem can then be recast as finding a dynamical system and an interconnection pattern such that the overall energy function takes the desired form [71]. Control effort in the application of this chapter is the energy consumed during the controller switching process. Numerical data is also provided in Table 2.2 Table

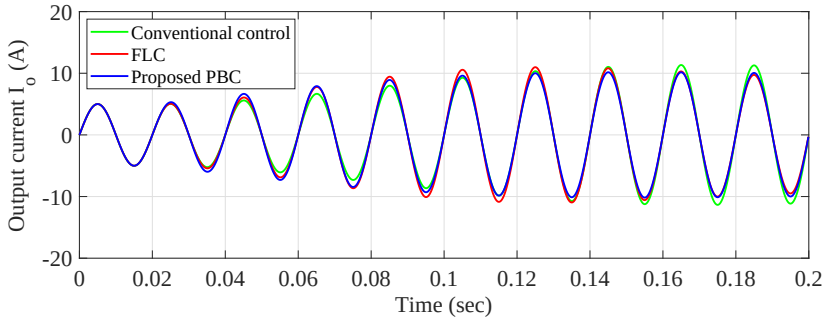

Figure 2.7: The waveform of output current obtained via applying the conventional control strategy, FLC proposed in [13] and proposed PBC when reference signal raised at 0.02s.

2.3and verified that the proposed PBC can save the control efforts effectively comparing with FLC proposed in [13]. The largely efforts savings (91.9% and 83.0%) comparing with FLC are benefiting from extra damping effects due to passivation in proposed PBC instead of fully linearization in FLC.

For damping performance comparison of different controllers, the reference signal is set to rise from 5A to 10A in a relatively slow rate which beginning at 0.02s. As shown in Fig. 2.7, the proposed control method can effectively suppress the overshoots and reach the required value rapidly comparing with other controllers. It is caused by its fully utilising the physical property and provide extra damping effect via passivation.

Table 2.2: IAE index of different control schemes for evaluating steady-state performance

Method \ Variable	IAE_{I_o}	$\text{IAE}_{I_\text{diff}}$	IAE_{u_o}	$\text{IAE}_{u_\text{diff}}$
Conventional control	0.3591	0.0078	0.460	0.3324
FLC in [13]	0.1052	0.006298	0.389	0.161
Proposed PBC	0.105	0.002039	0.03152	0.0273

Table 2.3: IAE index of different control schemes for evaluating dynamic response performance

Method \ Variable	$\mathrm{IAE}_{I_\mathrm{o}}$	$\mathrm{IAE}_{I_\mathrm{diff}}$	$\mathrm{IAE}_{u_\mathrm{o}}$	$\mathrm{IAE}_{u_\mathrm{diff}}$
Conventional control	0.4301	0.00971	0.4903	0.3782
FLC in [13]	0.1225	0.006786	0.4132	0.192
Proposed PBC	0.1203	0.002842	0.03635	0.0403

2.5 Conclusion

In this chapter, one PBC based control strategy has been proposed and applied on an N-level MMC steady state model for regulating internal dynamics. MMC is well-proven technology for VSC-HVDC application and owns highly nonlinearity and strong coupling among its states. PBC based current control strategy provide alternative for solving nonlinearity problem and decoupling the states of the system besides FLC proposed in [13]. The use of passivation in the controller can provide extra damping effects comparing regulating under fully system linearization. The proposed PBC also considers global stability and does not need further tuning when operating point varying. The simulation results and corresponding analysis in the steady state conditions verify the effectiveness of the proposed PBC. In comparison, conventional control introduces high-frequency chatting phenomenon and caused huge waste on control efforts due to incomplete nonlinearity compensation when operating points keep varying rapidly especially applying high-sampling-resolution reference signals. FLC still waste considerable proportion of control efforts for regulation under fully linearization. The overall control efforts can be largely saved via applying proposed PBC in MMC system.

As presented in this chapter, the PBC based control strategy is applied to the MMC based voltage source converter, and corresponding dynamic performance has been improved. In the next chapter, the control strategy of VSC based HVDC system will be modified.

Chapter 3

Perturbation Observer based Sliding Mode Control for Enhancing Dynamic Responses of VSC-HVDC Systems

3.1 Introduction

Voltage source converter based high voltage direct current (VSC-HVDC) systems using insulated gate bipolar transistor (IGBT) technology have attracted increasing attentions due to the interconnection between the mainland and offshore wind farms, power flow regulation in alternating current (AC) power systems, long distance transmission [72], and introduction of the supergrid, which is a large-scale power grid interconnected between national power grids [73]. The main feature of the VSC-HVDC system is that no external voltage source is needed for communication, while active and reactive power at each AC grid can be independently controlled [74]. In this chapter, investigated target is point-to-point two terminal VSC-HVDC system which used as bulk power transmission.

Traditionally, The VSC-HVDC system utilizes a nested-loop d-q vector control (VC) approach based on linear proportional-integral (PI) methods [75] for output

power and voltage regulations, whose control performance may be degraded with the change of operation conditions as its controller gains are tuned from one-point linearization model [76]. As VSC-HVDC systems are highly nonlinear resulted from converters and also operate in power systems with modelling uncertainties, many advanced control approaches are developed, such as feedback linearization control (FLC) [77] which fully compensating the nonlinearities with the requirement of an accurate system model, linear matrix inequality (LMI)-based robust control [78] which maximizing the size of the uncertainty region within while maintaining closed loop stability. In addition, adaptive backstepping control was designed to estimate the uncertain parameters [79]. In [80], power-synchronization control was employed to greatly increase the short-circuit capacity to the AC system. However, the aforementioned methods may not be adequate to simultaneously handle perturbations such as modelling uncertainties and time-varying external disturbances.

Based on the variable structure control strategy, sliding-mode control (SMC) is an effective and high-frequency switching robust control for nonlinear systems with modelling uncertainties and time-varying external disturbances. The main idea of SMC is to maintain the system sliding on a surface in the state space via an appropriate switching logic, it features the simple implementation, disturbance rejection, fast response and strong robustness [81]. While the malignant effect of chattering phenomenon can be reduced by predictive variable structure [82] and self-tuning sliding mode [83]. SMC has been applied to electrical vehicle [84], power converters [85], induction machine [86], and wind turbine [87]. A feedback linearization sliding-mode control (FLSMC) has been developed for the VSC-HVDC system to offer invariant stability to modelling uncertainties by [88], which can provide significant system damping and robustness under a variety of operation conditions. In practice, SMC assumes perturbations to be bounded and the prior knowledge of these upper bounds is required. However, it may be difficult or sometimes impossible to obtain these upper bounds, thus the supreme upper bound is chosen to cover the whole range of perturbations. Consequently, SMC based on this knowledge becomes over-conservative which may cause a poor tracking performance and undesirable control oscillations [89].

During the past decades, several elegant approaches based on observers have been proposed to estimate perturbations, including the unknown input observer (UIO) [90], the disturbance observer (DOB) [91], the equivalent input disturbance (EID) based estimation [92], and the extended state observer (ESO) based active disturbance rejection control (ADRC) [93], and practical multivariable control based on inverted decoupling and decentralized ADRC [94]. Among the above listed approaches, ESO requires the least amount of system information, in fact, only the system order should be known [95]. Due to such promising features, ESO based control schemes have become particularly propular. Recently, ESO based SMC has been developed to remedy the above issue of SMC with an online perturbation estimation. It observes both system states and perturbations by defining an extended state to represent the lumped perturbation, which can be then compensated online to improve the performance of system. Related applications can be referred to mechanical systems [96], missile systems [97], spherical robots [98], and DC-DC buck power converters [101].

In order to solve some of the problems of discontinuous operation of the switching devices in VSC-HVDC system with regards to changing parameters and external disturbances, this chapter adopts a developed ESO called sliding-mode state and perturbation observer (SMSPO) [125, 126] to estimate the combinatorial effect of nonlinearities, parameter uncertainties, unmodelled dynamics and time-varying external disturbances existed in VSC-HVDC systems, which is compensated by the perturbation observer based sliding-mode control (POSMC). The motivation to use POSMC can be summarized as follows, the robustness of proposed POSMC to the perturbation mostly depends on the perturbation compensation while the ground of the robustness in SMC is the discrete switching input. Furthermore, the upper bound of perturbation is replaced by the smaller bound of its estimation error, which yields a desirable level of control activity for a given precision of trajectory tracking. Compared to VC [76], POSMC can provide a consistent control performance under various operation condition of the VSC-HVDC system and improve the power tracking by eliminating the power overshoot. Compared to FLSMC [88], POSMC only requires the measurement of active and reactive power and DC voltage, which

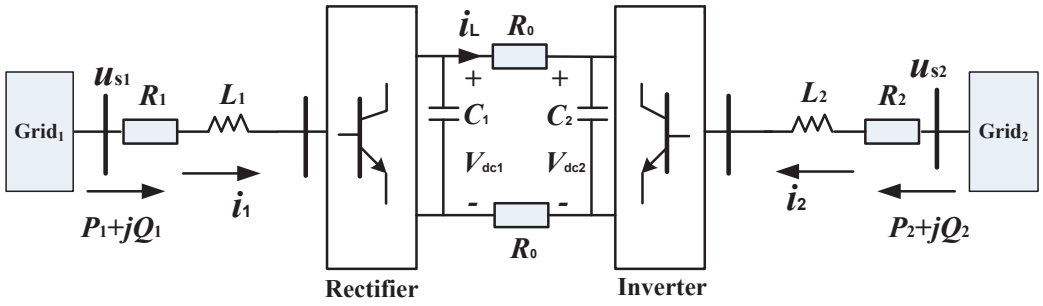

Figure 3.1: The two-terminal VSC-HVDC system

can provide a significant robustness and avoid an over-conservative control input as the real perturbation is estimated and compensated online. Four case studies are carried out to evaluate the control performance of POSMC through simulation, such as active and reactive power tracking, AC bus fault, system parameter uncertainties and weak AC gird connection. A dSPACE simulator based hardware-in-the-loop (HIL) test is then undertaken to validate the implementation feasibility of the proposed approach.

3.2 Two-terminal VSC-HVDC System Modelling

There are two VSCs in the VSC-HVDC system shown in Fig. 5.5, in which the rectifier regulates DC voltage and reactive power, while the inverter regulates the active and reactive power. Only the balanced condition is considered, e.g., the three phases have identical parameters and their voltages and currents have the same amplitude while each phase shifts 120° between themselves. The rectifier dynamics can be written at the angular frequency ω as [31]

$$\begin{cases} \frac{\mathrm{d}i_{\mathrm{d1}}}{\mathrm{d}t} = -\frac{R_1}{L_1} i_{\mathrm{d1}} + \omega i_{\mathrm{q1}} + u_{\mathrm{d1}} \\ \frac{\mathrm{d}i_{\mathrm{q1}}}{\mathrm{d}t} = -\frac{R_1}{L_1} i_{\mathrm{q1}} - \omega i_{\mathrm{d1}} + u_{\mathrm{q1}} \\ \frac{\mathrm{d}V_{\mathrm{dc1}}}{\mathrm{d}t} = \frac{3u_{\mathrm{sq1}} i_{\mathrm{q1}}}{2C_1 V_{\mathrm{dc1}}} - \frac{i_{\mathrm{L}}}{C_1} \end{cases} \tag{3.2.1}$$

where the rectifier is connected with the AC grid via the equivalent resistance and inductance R_1 and L_1, respectively; C_1 is the DC bus capacitor; $u_{\mathrm{q1}} = \frac{u_{\mathrm{sq1}} - u_{\mathrm{rq1}}}{L_1}$ and $u_{\mathrm{d1}} = \frac{u_{\mathrm{sd1}} - u_{\mathrm{rd1}}}{L_1}$.

The inverter dynamics is written as

$$\begin{cases} \frac{\mathrm{d}i_{\mathrm{d}2}}{\mathrm{d}t} = -\frac{R_2}{L_2} i_{\mathrm{d}2} + \omega i_{\mathrm{q}2} + u_{\mathrm{d}2} \\ \frac{\mathrm{d}i_{\mathrm{q}2}}{\mathrm{d}t} = -\frac{R_2}{L_2} i_{\mathrm{q}2} - \omega i_{\mathrm{d}2} + u_{\mathrm{q}2} \\ \frac{\mathrm{d}V_{\mathrm{dc}2}}{\mathrm{d}t} = \frac{3u_{\mathrm{sq}2}i_{\mathrm{q}2}}{2C_2V_{\mathrm{dc}2}} + \frac{i_{\mathrm{L}}}{C_2} \end{cases} \tag{3.2.2}$$

where the inverter is connected with the AC grid via the equivalent resistance and inductance R_2 and L_2, respectively; C_2 is the DC bus capacitor; $u_{\mathrm{q}2} = \frac{u_{\mathrm{sq}2} - u_{\mathrm{rq}2}}{L_2}$ and $u_{\mathrm{d}2} = \frac{u_{\mathrm{sd}2} - u_{\mathrm{rd}2}}{L_2}$.

The interconnection between the rectifier and inverter through DC cable is given as

$$V_{\mathrm{dc}1} i_{\mathrm{L}} = V_{\mathrm{dc}2} i_{\mathrm{L}} + 2R_0 i_{\mathrm{L}}^2 \tag{3.2.3}$$

where R_0 represents the equivalent DC cable resistance.

The phase-locked loop (PLL) is used during the transformation of the *abc* frame to the *dq* frame [99, 100]. In the synchronous frame, $u_{\mathrm{sd}1}$, $u_{\mathrm{sd}2}$, $u_{\mathrm{sq}1}$, and $u_{\mathrm{sq}2}$ are the $d-$, $q-$ axes components of the respective AC grid voltages; $i_{\mathrm{d}1}$, $i_{\mathrm{d}2}$, $i_{\mathrm{q}1}$, and $i_{\mathrm{q}2}$ are that of the line currents; $u_{\mathrm{rd}1}$, $u_{\mathrm{rd}2}$, $u_{\mathrm{rq}1}$, and $u_{\mathrm{rq}2}$ are that of the converter input voltages; P_1, P_2, Q_1, and Q_2 are the active and reactive power transferred from the AC grid to the VSC; $V_{\mathrm{dc}1}$ and $V_{\mathrm{dc}2}$ are DC voltages; and i_{L} is DC cable current.

At the rectifier side, the *q*-axis is set to be in phase with the AC grid voltage $u_{\mathrm{s}1}$. Correspondingly, the *q*-axis is set to be in phase with the AC grid voltage $u_{\mathrm{s}2}$ at the inverter side. Hence, $u_{\mathrm{sd}1}$ and $u_{\mathrm{sd}2}$ are equal to 0 while $u_{\mathrm{sq}1}$ and $u_{\mathrm{sq}2}$ are equal to the magnitude of $u_{\mathrm{s}1}$ and $u_{\mathrm{s}2}$. The VSC-HVDC system is assumed that being connected to sufficiently strong AC grids, such that the AC grid voltage remains as an ideal constant. Then the power flows from the AC grid can be given as

$$\begin{cases} P_1 = \frac{3}{2}\left(u_{\mathrm{sq}1} i_{\mathrm{q}1} + u_{\mathrm{sd}1} i_{\mathrm{d}1}\right) = \frac{3}{2} u_{\mathrm{sq}1} i_{\mathrm{q}1} \\ Q_1 = \frac{3}{2}\left(u_{\mathrm{sq}1} i_{\mathrm{d}1} - u_{\mathrm{sd}1} i_{\mathrm{q}1}\right) = \frac{3}{2} u_{\mathrm{sq}1} i_{\mathrm{d}1} \\ P_2 = \frac{3}{2}\left(u_{\mathrm{sq}2} i_{\mathrm{q}2} + u_{\mathrm{sd}2} i_{\mathrm{d}2}\right) = \frac{3}{2} u_{\mathrm{sq}2} i_{\mathrm{q}2} \\ Q_2 = \frac{3}{2}\left(u_{\mathrm{sq}2} i_{\mathrm{d}2} - u_{\mathrm{sd}2} i_{\mathrm{q}2}\right) = \frac{3}{2} u_{\mathrm{sq}2} i_{\mathrm{d}2} \end{cases} \tag{3.2.4}$$

3.3 POSMC Design for Two-terminal VSC-HVDC System

3.3.1 Perturbation Observer based Sliding Mode Control

Consider an uncertain nonlinear system which has the following canonical form

$$\begin{cases} \dot{x} = Ax + B(a(x) + b(x)u + d(t)) \\ y = x_1 \end{cases} \tag{3.3.1}$$

where $x = [x_1, x_2, \cdots, x_n]^{\mathrm{T}} \in \mathbb{R}^n$ is the state variable vector, $u \in \mathbb{R}$ and $y \in \mathbb{R}$ are the control input and system output, respectively. $a(x) : \mathbb{R}^n \mapsto \mathbb{R}$ and $b(x) : \mathbb{R}^n \mapsto \mathbb{R}$ are unknown smooth functions, and $d(t) : \mathbb{R}^+ \mapsto \mathbb{R}$ represents the time-varying external disturbance. The $n \times n$ matrix A and the $n \times 1$ matrix B are of the canonical form as follows

$$A = \begin{bmatrix} 0 & 1 & 0 & \cdots & 0 \\ 0 & 0 & 1 & \cdots & 0 \\ \vdots & & & & \vdots \\ 0 & 0 & 0 & \cdots & 1 \\ 0 & 0 & 0 & \cdots & 0 \end{bmatrix}_{n\times n}, \quad B = \begin{bmatrix} 0 \\ 0 \\ \vdots \\ 0 \\ 1 \end{bmatrix}_{n\times 1}$$

The perturbation of system (3.3.1) is defined as [125, 126, 61]

$$\Psi(x, u, t) = a(x) + (b(x) - b_0)u + d(t) \tag{3.3.2}$$

which is represented by a *fictitious state* written as $x_{n+1} = \Psi(x, u, t)$. Then, system (3.3.1) can be extended as

$$\begin{cases} y = x_1 \\ \dot{x}_1 = x_2 \\ \vdots \\ \dot{x}_n = x_{n+1} + b_0 u \\ \dot{x}_{n+1} = \dot{\Psi}(\cdot) \end{cases} \tag{3.3.3}$$

The new state vector becomes $x_{\mathrm{e}} = [x_1, x_2, \cdots, x_n, x_{n+1}]^{\mathrm{T}}$, the control object is to drive the system state x to track a desired state $x_{\mathrm{d}} = [y_{\mathrm{d}}, y_{\mathrm{d}}^{(1)}, \cdots, y_{\mathrm{d}}^{(n-1)}]^{\mathrm{T}}$, and following assumptions are made [125]

- A.1 b_0 is chosen to satisfy: $|b(x)/b_0 - 1| \leq \theta < 1$, where θ is a positive constant.

- A.2 The functions $\Psi(x, u, t) : \mathbb{R}^n \times \mathbb{R} \times \mathbb{R}^+ \mapsto \mathbb{R}$ and $\dot{\Psi}(x, u, t) : \mathbb{R}^n \times \mathbb{R} \times \mathbb{R}^+ \mapsto \mathbb{R}$ are bounded over the domain of interest: $|\Psi(x, u, t)| \leq \gamma_1$, $|\dot{\Psi}(x, u, t)| \leq \gamma_2$ with $\Psi(0, 0, 0) = 0$ and $\dot{\Psi}(0, 0, 0) = 0$, where γ_1 and γ_2 are positive constants.

- A.3 The desired trajectory y_d and its up to nth-order derivative are continuous and bounded.

Under the above three assumptions, the effectiveness of such perturbation estimation based approach can be guaranteed. In particular, Assumptions A.1 and A.2 guarantee the closed-loop system stability with perturbation estimation, while Assumption A.3 ensures that POSMC can drive the system state x to track a desired state. In the consideration of the worst case such as that only the system output $y = x_1$ is available, an (n+1)th-order SMSPO [125, 126] for the extended system (3.3.3) is employed to estimate the system states and perturbation as follows

$$\begin{cases} \dot{\hat{x}}_1 = \hat{x}_2 + \alpha_1 \tilde{x}_1 + k_1 \mathrm{sat}(\tilde{x}_1) \\ \quad \vdots \\ \dot{\hat{x}}_n = \hat{\Psi}(\cdot) + \alpha_n \tilde{x}_1 + k_n \mathrm{sat}(\tilde{x}_1) + b_0 u \\ \dot{\hat{\Psi}}(\cdot) = \alpha_{n+1} \tilde{x}_1 + k_{n+1} \mathrm{sat}(\tilde{x}_1) \end{cases} \tag{3.3.4}$$

where $\tilde{x}_1 = x_1 - \hat{x}_1$, k_i and α_i, $i = 1, 2, \cdots, n+1$, are positive coefficients, function $\mathrm{sat}(\tilde{x}_1)$ is defined as $\mathrm{sat}(\tilde{x}_1) = \tilde{x}_1/|\tilde{x}_1|$ when $|\tilde{x}_1| > \epsilon$ and $\mathrm{sat}(\tilde{x}_1) = \tilde{x}_1/\epsilon$ when $|\tilde{x}_1| \leq \epsilon$, where ϵ is a small positive scalar. The constants α_i are chosen as in a Luenberger observer so as to place the poles at the desired locations in the open left-half complex plane. In other words, α_i are chosen such that the root of $s^{n+1} + \alpha_1 s^n + \alpha_2 s^{n-1} + \cdots + \alpha_{n+1} = (s + \lambda_\alpha)^{n+1} = 0$ is in the open left-half complex plain. A larger value of α_i will accelerate the estimation rate of SMSPO but also result in generating peaking phenomenon. Thus a trade-off between the estimation rate and effect of peaking phenomenon must be made through trial-and-error. Normally they are set to be much larger than the root of the closed-loop system to

ensure a fast online estimation. According to [125], the condition for the existence of the sliding mode of SMSPO (3.3.4) is: $k_1 \geq |\tilde{x}_2|_{\max}$. The sliding surface constant is chosen to guarantee that the estimation error of SMSPO will enter into the sliding surface. *And* poles on the sliding surface can be properly set by selecting the ratio $k_i/k_1(i = 2, 3, \cdots, n+1)$. Precisely, k_i are chosen such that the pole of $p^n + (k_2/k_1)p^{n-1} + \cdots + (k_n/k_1)p + (k_{n+1}/k_1) = (p + \lambda_k)^n = 0$ to be in the open left-half complex plane. Under Assumption A.2, the SMSPO converges to a neighbourhood of the origin if gains k_i are properly selected, which has been proved in [125, 104]. For a given k_i, a larger k_i will accelerate the estimation rate of SMSPO but also result in a degraded observer stability. Thus a trade-off between the estimation rate and observer stability must be made through trial-and-error. The layer thickness constant of saturation function ϵ: Which is a positive small scaler to replace the sign function by the saturation function, such that the chattering effect can be reduced. A larger ϵ will result in a smoother chattering but a larger steady-state estimation error. Consequently, a trade-off between the chattering effect and steady-state estimation error must be made through trial-and-error. In practice, a value closes to 0 is recommended.

Remark 1. When SMSPO is used to estimate the perturbation, the upper bound of the derivative of perturbation γ_2 is required to guarantee the estimation accuracy, and such upper bound will result in a conservative observer gain. However, the conservative gain is only included in the observer loop, not in the controller loop.

Remark 2. In assumption A.2, only the upper bound of the derivative of perturbation γ_2 is used. This may be reasonable when the control input is bounded in a real system. However, when a complete observer and controller system is investigated, the more reasonable and strict assumption is to include the controller definition in the assumption. If the Lipschitiz condition in Assumption A.2 is considered, an error convergence to the origin will be achieved [105].

Define an estimated sliding surface as

$$\hat{S}(x,t) = \sum_{i=1}^{n} \rho_i(\hat{x}_i - y_{\mathrm{d}}^{(i-1)}) \tag{3.3.5}$$

where the estimated sliding surface gains $\rho_i = C_{n-1}^{i-1}\lambda_{\mathrm{c}}^{n-i}$, $i = 1, \cdots, n$, place all poles of the estimated sliding surface at $-\lambda_{\mathrm{c}}$, where $\lambda_{\mathrm{c}} > 0$.

The POSMC for system (3.3.1) is designed as

$$u = \frac{1}{b_0}\left[y_{\mathrm{d}}^{(n)} - \sum_{i=1}^{n-1}\rho_i(\hat{x}_{i+1} - y_{\mathrm{d}}^{(i)}) - \zeta\hat{S} - \varphi\mathrm{sat}(\hat{S}) - \hat{\Psi}(\cdot)\right] \tag{3.3.6}$$

where ζ and φ are control gains which are chosen to fulfill the attractiveness of the estimated sliding surface $\hat{S}$.

Note that POSMC does not require an accurate system model and only one state measurement $y = x_1$ is needed. As the upper bound of perturbation $\Psi(\cdot)$ is replaced by the smaller bound of its estimation error $\tilde{\Psi}(\cdot)$, a smaller control gain is needed such that the over-conservativeness of SMC can be avoided [125]. **Remark 3.** The motivation to use SMSPO is due to the fact that the sliding-mode observer potentially offers advantages similar to those of sliding-mode controllers, in particular, inherent robustness to parameter uncertainty and external disturbances. It is a high-performance state estimator with a simple structure and is well suited for uncertain nonlinear systems. Moreover, it has the merits of simple structure and easy analysis of the closed-loop system stability compared to that of ADRC which uses a nonlinear observer while they can provide almost the same performance of perturbation estimation. The design procedure of POSMC for system (3.3.1) can be summarized as follows:

Step 1: Define perturbation (3.3.2) for the original nth-order system (3.3.1);

Step 2: Define a *fictitious state* $x_{n+1} = \Psi(\cdot)$ to represent perturbation (3.3.2);

Step 3: Extend the original nth-order system (3.3.1) into the extended $(n+1)$th-order system (3.3.3);

Step 4: Design the $(n+1)$th-order SMSPO (3.3.4) for the extended $(n+1)$th-order system (3.3.3) to obtain the state estimate $\hat{x}$ and the perturbation estimate $\hat{\Psi}(\cdot)$ by only the measurement of x_1;

Step 5: Design controller (3.3.6) for the original nth-order system (3.3.1), in which the estimated sliding surface $\hat{S}$ is calculated by (3.3.5).

3.3.2 Rectifier Controller Design

Choose the system output $y_{\mathrm{r}} = [y_{\mathrm{r}1}, y_{\mathrm{r}2}]^{\mathrm{T}} = [Q_1, V_{\mathrm{dc}1}]^{\mathrm{T}}$, let Q_1^* and $V_{\mathrm{dc}1}^*$ be the given references of the reactive power and DC voltage, respectively. Define the tracking error $e_{\mathrm{r}} = [e_{\mathrm{r}1}, e_{\mathrm{r}2}]^{\mathrm{T}} = [Q_1 - Q_1^*, V_{\mathrm{dc}1} - V_{\mathrm{dc}1}^*]^{\mathrm{T}}$, differentiate e_{r} for rectifier (4.2.1) until the control input appears explicitly, yields

$$\begin{bmatrix} \dot{e}_{\mathrm{r}1} \\ \ddot{e}_{\mathrm{r}2} \end{bmatrix} = \begin{bmatrix} f_{\mathrm{r}1} - \dot{Q}_1^* \\ f_{\mathrm{r}2} - \ddot{V}_{\mathrm{dc}1}^* \end{bmatrix} + B_{\mathrm{r}} \begin{bmatrix} u_{\mathrm{d}1} \\ u_{\mathrm{q}1} \end{bmatrix} \tag{3.3.7}$$

where

$$\begin{cases} f_{\mathrm{r}1} = \dfrac{3u_{\mathrm{sq}1}}{2}\left(-\dfrac{R_1}{L_1} i_{\mathrm{d}1} + \omega i_{\mathrm{q}1}\right) \\ f_{\mathrm{r}2} = \dfrac{3u_{\mathrm{sq}1}}{2C_1 V_{\mathrm{dc}1}}\left[-\omega i_{\mathrm{d}1} - \dfrac{R_1}{L_1} i_{\mathrm{q}1} - \dfrac{i_{\mathrm{q}1}}{V_{\mathrm{dc}1}}\left(\dfrac{3u_{\mathrm{sq}1} i_{\mathrm{q}1}}{2C_1 V_{\mathrm{dc}1}} - \dfrac{i_{\mathrm{L}}}{C_1}\right)\right] \\ \quad - \dfrac{1}{2R_0 C_1}\left(\dfrac{3u_{\mathrm{sq}1} i_{\mathrm{q}1}}{2C_1 V_{\mathrm{dc}1}} - \dfrac{i_{\mathrm{L}}}{C_1} - \dfrac{3u_{\mathrm{sq}2} i_{\mathrm{q}2}}{2C_2 V_{\mathrm{dc}2}} - \dfrac{i_{\mathrm{L}}}{C_2}\right) \end{cases}$$

and

$$B_{\mathrm{r}} = \begin{bmatrix} \frac{3u_{\mathrm{sq}1}}{2L_1} & 0 \\ 0 & \frac{3u_{\mathrm{sq}1}}{2C_1 L_1 V_{\mathrm{dc}1}} \end{bmatrix}$$

The determinant of matrix B_{r} is obtained as $|B_{\mathrm{r}}| = 9u_{\mathrm{sq}1}^2/(4C_1 L_1^2 V_{\mathrm{dc}1})$, which is non-zero within the operation range of the rectifier, thus system (3.3.7) is linearizable.

Assume all the nonlinearities are unknown, define the perturbations $\Psi_{\mathrm{r}1}(\cdot)$ and $\Psi_{\mathrm{r}2}(\cdot)$ as

$$\begin{bmatrix} \Psi_{\mathrm{r}1}(\cdot) \\ \Psi_{\mathrm{r}2}(\cdot) \end{bmatrix} = \begin{bmatrix} f_{\mathrm{r}1} \\ f_{\mathrm{r}2} \end{bmatrix} + (B_{\mathrm{r}} - B_{\mathrm{r}0}) \begin{bmatrix} u_{\mathrm{d}1} \\ u_{\mathrm{q}1} \end{bmatrix} \tag{3.3.8}$$

where the constant control gain $B_{\mathrm{r}0}$ is given by

$$B_{\mathrm{r}0} = \begin{bmatrix} b_{\mathrm{r}10} & 0 \\ 0 & b_{\mathrm{r}20} \end{bmatrix}$$

Then system (3.3.7) can be rewritten as

$$\begin{bmatrix} \dot{e}_{\mathrm{r}1} \\ \ddot{e}_{\mathrm{r}2} \end{bmatrix} = \begin{bmatrix} \Psi_{\mathrm{r}1}(\cdot) \\ \Psi_{\mathrm{r}2}(\cdot) \end{bmatrix} + B_{\mathrm{r}0} \begin{bmatrix} u_{\mathrm{d}1} \\ u_{\mathrm{q}1} \end{bmatrix} - \begin{bmatrix} \dot{Q}_1^* \\ \ddot{V}_{\mathrm{dc}1}^* \end{bmatrix} \tag{3.3.9}$$

Define $z'_{11} = Q_1$, a second-order sliding-mode perturbation observer (SMPO) is used to estimate $\Psi_{\mathrm{r1}}(\cdot)$ as

$$\begin{cases} \dot{\hat{z}}'_{11} = \hat{\Psi}_{\mathrm{r1}}(\cdot) + \alpha'_{\mathrm{r1}}\tilde{Q}_1 + k'_{\mathrm{r1}}\mathrm{sat}(\tilde{Q}_1) + b_{\mathrm{r10}}u_{\mathrm{d1}} \\ \dot{\hat{\Psi}}_{\mathrm{r1}}(\cdot) = \alpha'_{\mathrm{r2}}\tilde{Q}_1 + k'_{\mathrm{r2}}\mathrm{sat}(\tilde{Q}_1) \end{cases} \tag{3.3.10}$$

where observer gains k'_{r1}, k'_{r2}, α'_{r1}, and α'_{r2} are all positive constants.

Define $z_{11} = V_{\mathrm{dc1}}$ and $z_{12} = \dot{z}_{11}$, a third-order SMSPO is used to estimate $\Psi_{\mathrm{r2}}(\cdot)$ as

$$\begin{cases} \dot{\hat{z}}_{11} = \hat{z}_{12} + \alpha_{\mathrm{r1}}\tilde{V}_{\mathrm{dc1}} + k_{\mathrm{r1}}\mathrm{sat}(\tilde{V}_{\mathrm{dc1}}) \\ \dot{\hat{z}}_{12} = \hat{\Psi}_{\mathrm{r2}}(\cdot) + \alpha_{\mathrm{r2}}\tilde{V}_{\mathrm{dc1}} + k_{\mathrm{r2}}\mathrm{sat}(\tilde{V}_{\mathrm{dc1}}) + b_{\mathrm{r20}}u_{\mathrm{q1}} \\ \dot{\hat{\Psi}}_{\mathrm{r2}}(\cdot) = \alpha_{\mathrm{r3}}\tilde{V}_{\mathrm{dc1}} + k_{\mathrm{r3}}\mathrm{sat}(\tilde{V}_{\mathrm{dc1}}) \end{cases} \tag{3.3.11}$$

where observer gains k_{r1}, k_{r2}, k_{r3}, α_{r1}, α_{r2}, and α_{r3} are all positive constants.

The estimated sliding surface of system (3.3.7) is defined as

$$\begin{bmatrix} \hat{S}_{\mathrm{r1}} \\ \hat{S}_{\mathrm{r2}} \end{bmatrix} = \begin{bmatrix} \hat{z}'_{11} - Q_1^* \\ \rho_1(\hat{z}_{11} - V_{\mathrm{dc1}}^*) + \rho_2(\hat{z}_{12} - \dot{V}_{\mathrm{dc1}}^*) \end{bmatrix} \tag{3.3.12}$$

where ρ_1 and ρ_2 are the positive sliding surface gains.

The POSMC of system (3.3.7) is designed as

$$\begin{bmatrix} u_{\mathrm{d1}} \\ u_{\mathrm{q1}} \end{bmatrix} = B_{\mathrm{r0}}^{-1} \begin{bmatrix} -\hat{\Psi}_{\mathrm{r1}}(\cdot) + \dot{Q}_1^* - \zeta'_{\mathrm{r}}\hat{S}_{\mathrm{r1}} - \varphi'_{\mathrm{r}}\mathrm{sat}(\hat{S}_{\mathrm{r1}}) \\ -\hat{\Psi}_{\mathrm{r2}}(\cdot) + \ddot{V}_{\mathrm{dc1}}^* - \zeta_{\mathrm{r}}\hat{S}_{\mathrm{r2}} - \varphi_{\mathrm{r}}\mathrm{sat}(\hat{S}_{\mathrm{r2}}) \end{bmatrix} \tag{3.3.13}$$

where positive control gains ζ_{r}, ζ'_{r}, φ_{r}, and φ'_{r} are chosen to ensure the attractiveness of estimated sliding surface (3.3.12).

During the most severe disturbance, both the reactive power and DC voltage reduce from their initial value to around zero within a short period of time Δ. Thus the boundary values of the system state and perturbation estimates can be obtained as $|\hat{z}'_{11}| \leq |Q_1^*|$, $|\hat{\Psi}_{\mathrm{r1}}(\cdot)| \leq |Q_1^*|/\Delta$, $|\hat{z}_{11}| \leq |V_{\mathrm{dc1}}^*|$, $|\hat{z}_{12}| \leq |V_{\mathrm{dc1}}^*|/\Delta$, and $|\hat{\Psi}_{\mathrm{r2}}(\cdot)| \leq |V_{\mathrm{dc1}}^*|/\Delta^2$, respectively.

3.3.3 Inverter controller design

Choose the system output $y_{\mathrm{i}} = [y_{\mathrm{i1}}, y_{\mathrm{i2}}]^{\mathrm{T}} = [Q_2, P_2]^{\mathrm{T}}$, let Q_2^* and P_2^* be the given references of the reactive and active power, respectively. Define the tracking

error $e_{\mathrm{i}} = [e_{\mathrm{i}1}, e_{\mathrm{i}2}]^{\mathrm{T}} = [Q_2 - Q_2^*, P_2 - P_2^*]^{\mathrm{T}}$, differentiate e_{i} for inverter (3.2.2) until the control input appears explicitly, yields

$$\begin{bmatrix} \dot{e}_{\mathrm{i}1} \\ \dot{e}_{\mathrm{i}2} \end{bmatrix} = \begin{bmatrix} f_{\mathrm{i}1} - \dot{Q}_2^* \\ f_{\mathrm{i}2} - \dot{P}_2^* \end{bmatrix} + B_{\mathrm{i}} \begin{bmatrix} u_{\mathrm{d}2} \\ u_{\mathrm{q}2} \end{bmatrix} \tag{3.3.14}$$

where

$$\begin{cases} f_{\mathrm{i}1} = \dfrac{3u_{\mathrm{sq}2}}{2}\left(-\dfrac{R_2}{L_2} i_{\mathrm{d}2} + \omega i_{\mathrm{q}2}\right) \\ f_{\mathrm{i}2} = \dfrac{3u_{\mathrm{sq}2}}{2}\left(-\dfrac{R_2}{L_2} i_{\mathrm{q}2} - \omega i_{\mathrm{d}2}\right) \end{cases}$$

and

$$B_{\mathrm{i}} = \begin{bmatrix} \frac{3u_{\mathrm{sq}2}}{2L_2} & 0 \\ 0 & \frac{3u_{\mathrm{sq}2}}{2L_2} \end{bmatrix}$$

The determinant of matrix B_{i} is obtained as $|B_{\mathrm{i}}| = 9u_{\mathrm{s}2}^2/(4L_2^2)$, which is non-zero within the operation range of the inverter, thus system (3.3.14) is linearizable.

Assume all the nonlinearities are unknown, define the perturbations $\Psi_{\mathrm{i}1}(\cdot)$ and $\Psi_{\mathrm{i}2}(\cdot)$ as

$$\begin{bmatrix} \Psi_{\mathrm{i}1}(\cdot) \\ \Psi_{\mathrm{i}2}(\cdot) \end{bmatrix} = \begin{bmatrix} f_{\mathrm{i}1} \\ f_{\mathrm{i}2} \end{bmatrix} + (B_{\mathrm{i}} - B_{\mathrm{i}0}) \begin{bmatrix} u_{\mathrm{d}2} \\ u_{\mathrm{q}2} \end{bmatrix} \tag{3.3.15}$$

where the constant control gain $B_{\mathrm{i}0}$ is given by

$$B_{\mathrm{i}0} = \begin{bmatrix} b_{\mathrm{i}10} & 0 \\ 0 & b_{\mathrm{i}20} \end{bmatrix}$$

Then system (3.3.14) can be rewritten as

$$\begin{bmatrix} \dot{e}_{\mathrm{i}1} \\ \dot{e}_{\mathrm{i}2} \end{bmatrix} = \begin{bmatrix} \Psi_{\mathrm{i}1}(\cdot) \\ \Psi_{\mathrm{i}2}(\cdot) \end{bmatrix} + B_{\mathrm{i}0} \begin{bmatrix} u_{\mathrm{d}2} \\ u_{\mathrm{q}2} \end{bmatrix} - \begin{bmatrix} \dot{Q}_2^* \\ \dot{P}_2^* \end{bmatrix} \tag{3.3.16}$$

Similarly, define $z'_{21} = Q_2$ and $z_{21} = P_2$, two second-order SMPOs are used to estimate $\Psi_{\mathrm{i}1}(\cdot)$ and $\Psi_{\mathrm{i}2}(\cdot)$, respectively, as

$$\begin{cases} \dot{\hat{z}}'_{21} = \hat{\Psi}_{\mathrm{i}1}(\cdot) + \alpha'_{\mathrm{i}1}\tilde{Q}_2 + k'_{\mathrm{i}1}\mathrm{sat}(\tilde{Q}_2) + b_{\mathrm{i}10}u_{\mathrm{d}2} \\ \dot{\hat{\Psi}}_{\mathrm{i}1}(\cdot) = \alpha'_{\mathrm{i}2}\tilde{Q}_2 + k'_{\mathrm{i}2}\mathrm{sat}(\tilde{Q}_2) \end{cases} \tag{3.3.17}$$

where observer gains $k'_{\mathrm{i}1}$, $k'_{\mathrm{i}2}$, $\alpha'_{\mathrm{i}1}$, and $\alpha'_{\mathrm{i}2}$ are all positive constants.

$$\begin{cases} \dot{\hat{z}}_{21} = \hat{\Psi}_{\mathrm{i}2}(\cdot) + \alpha_{\mathrm{i}1}\tilde{P}_2 + k_{\mathrm{i}1}\mathrm{sat}(\tilde{P}_2) + b_{\mathrm{i}20}u_{\mathrm{q}2} \\ \dot{\hat{\Psi}}_{\mathrm{i}2}(\cdot) = \alpha_{\mathrm{i}2}\tilde{P}_2 + k_{\mathrm{i}2}\mathrm{sat}(\tilde{P}_2) \end{cases} \tag{3.3.18}$$

where observer gains $k_{\mathrm{i}1}$, $k_{\mathrm{i}2}$, $\alpha_{\mathrm{i}1}$, and $\alpha_{\mathrm{i}2}$ are all positive constants .

The estimated sliding surface of system (3.3.14) is defined as

$$\begin{bmatrix} \hat{S}_{\mathrm{i}1} \\ \hat{S}_{\mathrm{i}2} \end{bmatrix} = \begin{bmatrix} \hat{z}'_{21} - Q_2^* \\ \hat{z}_{21} - P_2^* \end{bmatrix} \tag{3.3.19}$$

The POSMC of system (3.3.14) is designed as

$$\begin{bmatrix} u_{\mathrm{d}2} \\ u_{\mathrm{q}2} \end{bmatrix} = B_{\mathrm{i}0}^{-1} \begin{bmatrix} -\hat{\Psi}_{\mathrm{i}1}(\cdot) + \dot{Q}_2^* - \zeta'_{\mathrm{i}}\hat{S}_{\mathrm{i}1} - \varphi'_{\mathrm{i}}\mathrm{sat}(\hat{S}_{\mathrm{i}1}) \\ -\hat{\Psi}_{\mathrm{i}2}(\cdot) + \dot{P}_2^* - \zeta_{\mathrm{i}}\hat{S}_{\mathrm{i}2} - \varphi_{\mathrm{i}}\mathrm{sat}(\hat{S}_{\mathrm{i}2}) \end{bmatrix} \tag{3.3.20}$$

where positive control gains ζ_{i}, ζ_{i}, φ_{i}, and φ'_{i} are chosen to ensure the attractiveness of estimated sliding surface (3.3.19).

Similarly, the boundary values of the system state and perturbation estimates can be obtained as $|\hat{z}'_{21}| \leq |Q_2^*|$, $|\hat{\Psi}_{\mathrm{i}1}(\cdot)| \leq |Q_2^*|/\Delta$, $|\hat{z}_{21}| \leq |P_2^*|$, and $|\hat{\Psi}_{\mathrm{i}2}(\cdot)| \leq |P_2^*|/\Delta$, respectively.

The overall controller structure of the VSC-HVDC system is illustrated by Fig. 4.6, in which only reactive power Q_1 and DC voltage $V_{\mathrm{dc}1}$ need to be measured for rectifier controller (5.3.7), while active power P_2 and reactive power Q_2 for inverter controller (5.3.16).

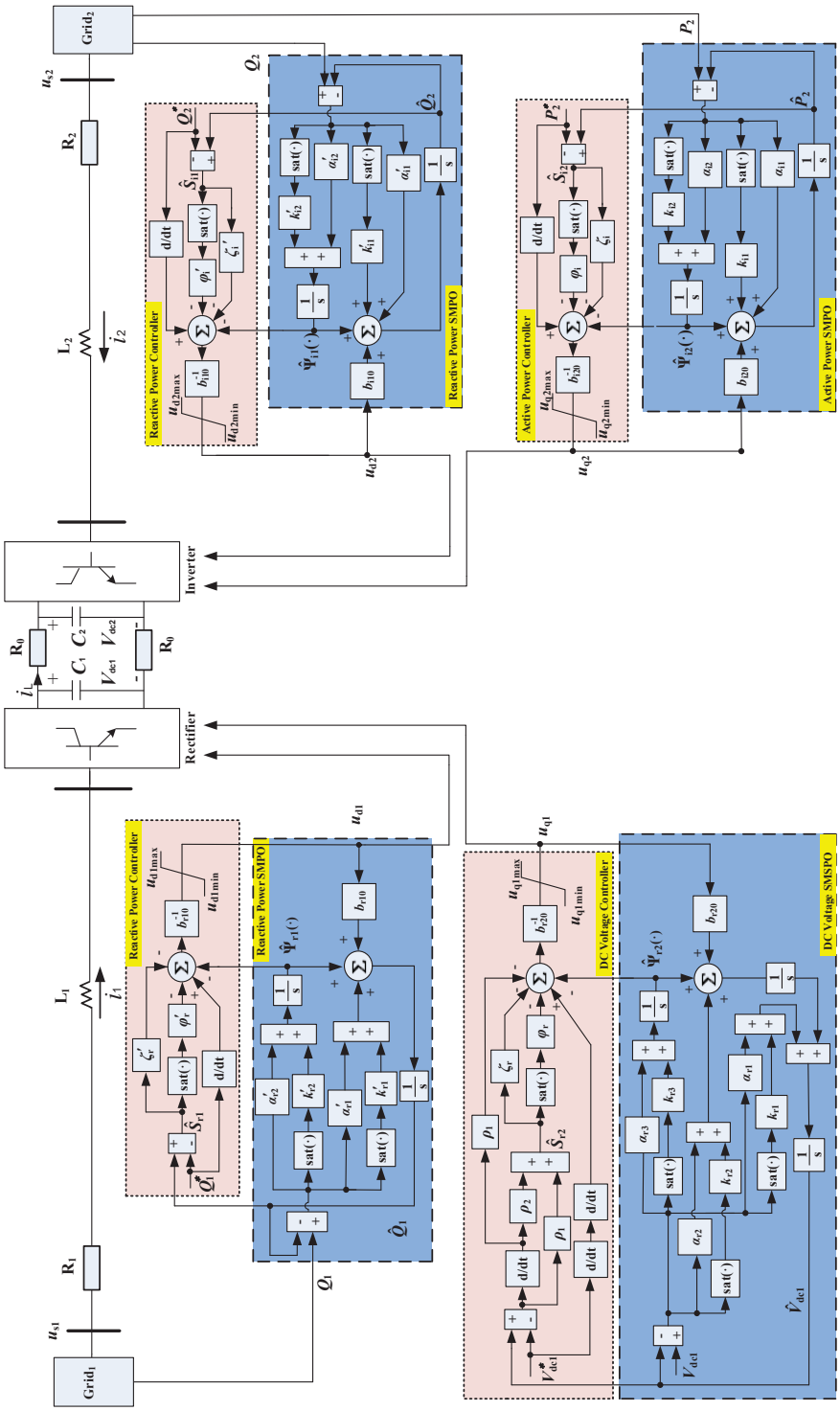

Figure 3.2: The overall controller structure of the VSC-HVDC system.

Table 3.1: The VSC-HVDC system parameters

AC system based voltage	$V_{\mathrm{AC}_{\mathrm{base}}}$	100 kV
DC cable base voltage	$V_{\mathrm{DC}_{\mathrm{base}}}$	150 kV
System base power	S_{base}	100 MVA
AC system resistance (25 km)	R_1, R_2	0.05 Ω/km
AC system inductance (25 km)	L_1, L_2	0.026 mH/km
DC cable resistance (50 km)	R_0	0.21 Ω/km
DC bus capacitance	C_1, C_2	11.94 μF

3.4 Simulation Results for Two-terminal VSC-HVDC System

Proposed POSMC is applied on the VSC-HVDC system illustrated in Fig. 5.5. The AC grid frequency is 50 Hz and VSC-HVDC system parameters are given in Table 5.1. POSMC parameters are provided in Table 3.2, in which the observer poles are allocated as $\lambda_{\alpha_{\mathrm{r}}} = 100$ and $\lambda_{\alpha'_{\mathrm{r}}} = \lambda_{\alpha_{\mathrm{i}}} = \lambda_{\alpha'_{\mathrm{i}}} = 20$, while control inputs are bounded as $|u_{\mathrm{q}i}| \leq 80$ kV and $|u_{\mathrm{d}i}| \leq 60$ kV, where $i = 1, 2$. The boundary value mentioned above is set via d-q transform algorithm on converter voltage. And corresponding converter voltage boundary is obtained via trial and error on the system model. The control performance of POSMC is evaluated under various operation conditions in a wide neighbourhood of initial operation points and compared to that of VC [76] and FLSMC [88].

1) Case 1: Active and reactive power tracking: The references of active and reactive power are set to be a series of step change occurs at $t = 0.2$ s, $t = 0.4$ s, and restores to the original value at $t = 0.6$ s, while DC voltage is regulated at the rated value $V^*_{\mathrm{dc1}} = 150$ kV. The system responses are illustrated by Fig. 3.4. One can find that POSMC has the fastest tracking rate and maintains a consistent control performance under different operation conditions.

2) Case 2: 5-cycle line-line-line-ground (LLLG) fault at AC bus 1. A 5-cycle LLLG fault occurs at AC bus 1 when $t = 0.1$ s. Due to the fault, AC voltage at the corresponding bus is decreased to a critical level. Fig. 3.6 shows that POSMC can

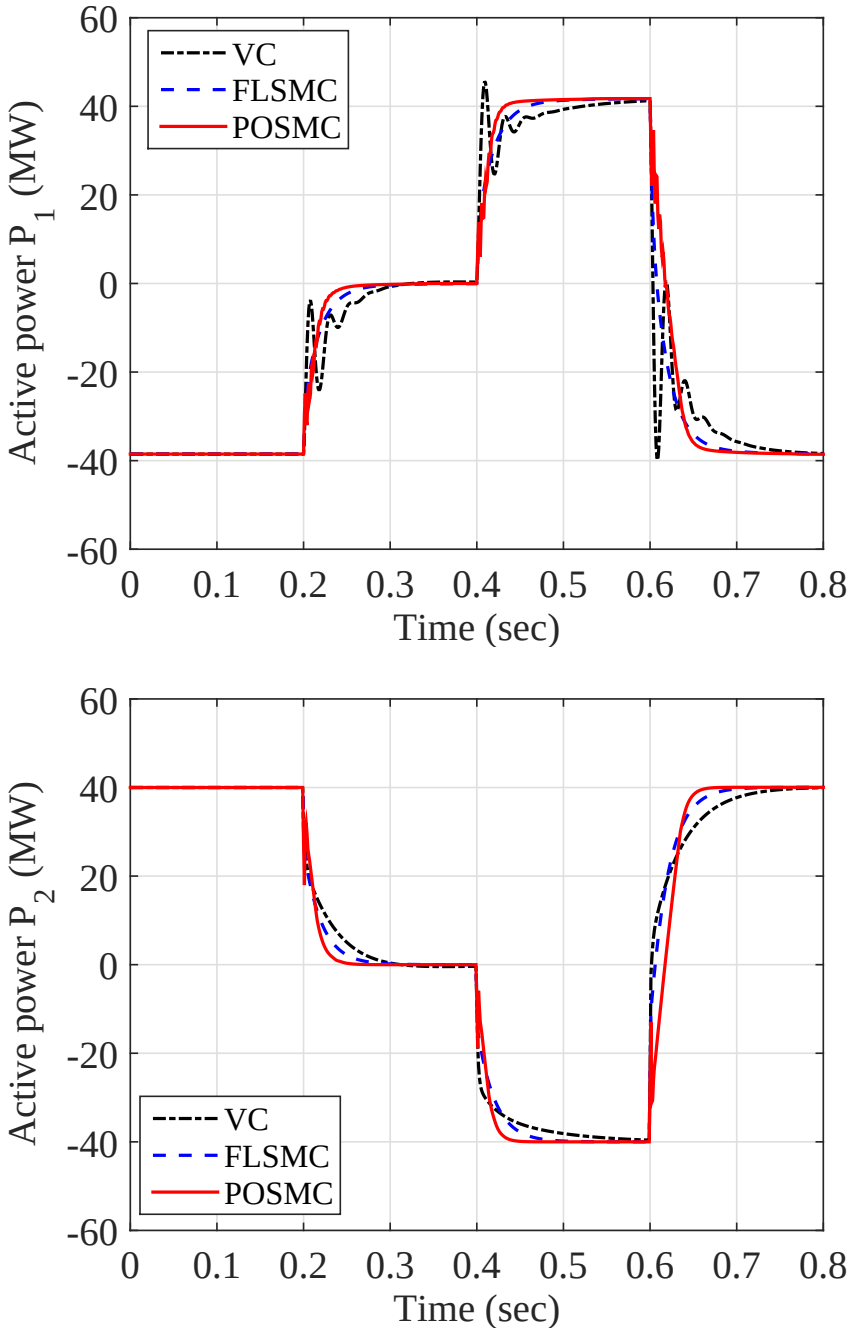

Figure 3.3: System responses obtained under the active and reactive power tracking-1.

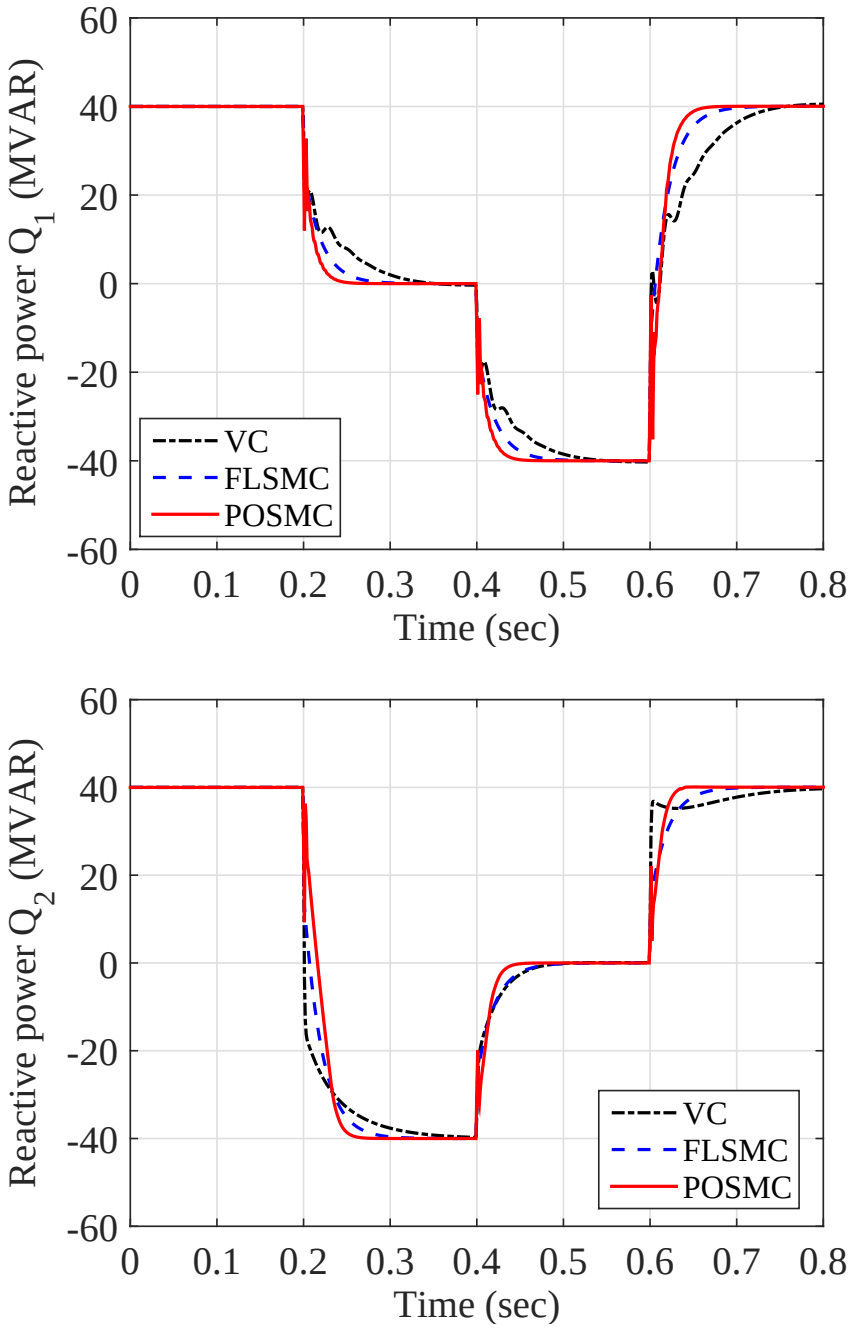

Figure 3.4: System responses obtained under the active and reactive power tracking-2.

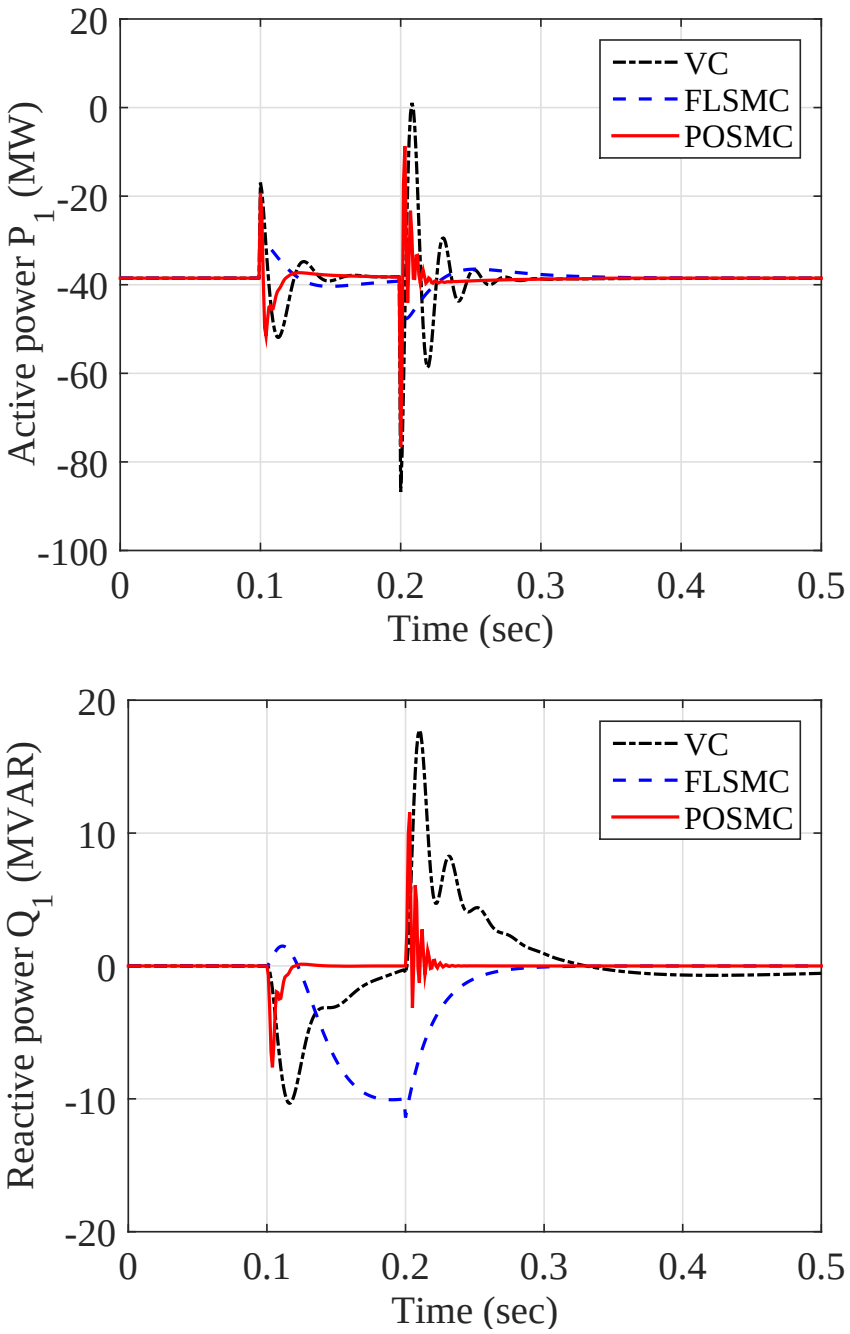

Figure 3.5: System responses obtained under the 5-cycle LLLG fault at AC bus 1-1.

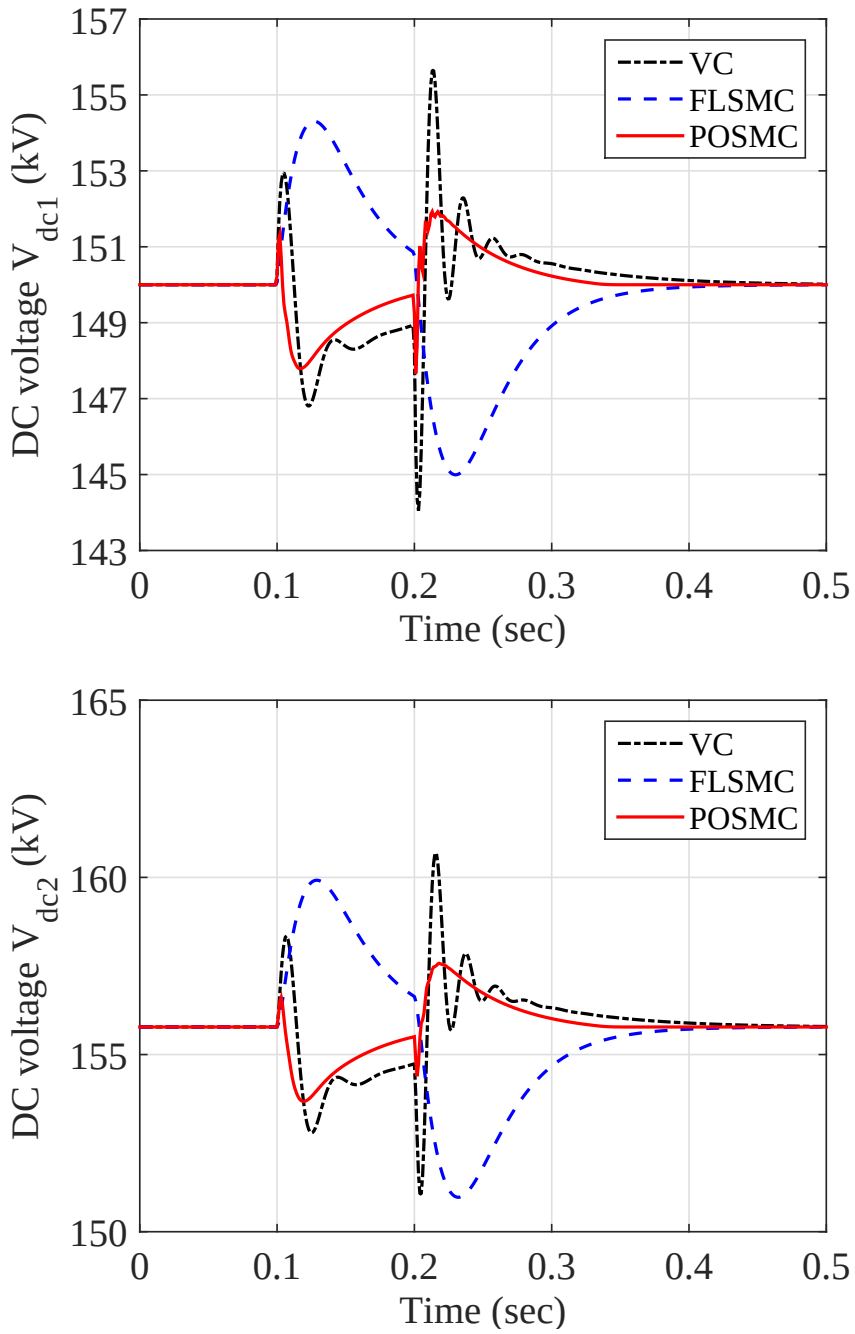

Figure 3.6: System responses obtained under the 5-cycle LLLG fault at AC bus 1-2.

Table 3.2: POSMC parameters for the VSC-HVDC system

Rectifier Controller Gains			
$b_{\mathrm{r}10} = 100$	$b_{\mathrm{r}20} = 7000$	$\rho_1 = 800$	$\rho_2 = 1$
$\zeta_{\mathrm{r}} = 20$	$\zeta'_{\mathrm{r}} = 10$	$\varphi_{\mathrm{r}} = 20$	$\varphi'_{\mathrm{r}} = 20$
Rectifier Observer Gains			
$\alpha_{\mathrm{r}1} = 300$	$\alpha'_{\mathrm{r}1} = 40$	$\alpha_{\mathrm{r}2} = 3 \times 10^4$	$\alpha'_{\mathrm{r}2} = 400$
$\alpha_{\mathrm{r}3} = 10^6$	$\Delta = 0.01$	$\epsilon = 0.1$	$k_{\mathrm{r}1} = 100$
$k'_{\mathrm{r}1} = 75$	$k_{\mathrm{r}2} = 10^5$	$k'_{\mathrm{r}2} = 3.75 \times 10^4$	$k_{\mathrm{r}3} = 2.5 \times 10^7$
Inverter Controller Gains			
$b_{\mathrm{i}10} = 50$	$b_{\mathrm{i}20} = 50$	$\zeta_{\mathrm{i}} = 10$	$\zeta'_{\mathrm{i}} = 10$
$\varphi_{\mathrm{i}} = 10$	$\varphi'_{\mathrm{i}} = 10$		
Inverter Observer Gains			
$\alpha_{\mathrm{i}1} = 40$	$\alpha'_{\mathrm{i}1} = 40$	$\alpha_{\mathrm{i}2} = 400$	$\alpha'_{\mathrm{i}2} = 400$
$k_{\mathrm{i}1} = 75$	$k'_{\mathrm{i}1} = 75$	$k_{\mathrm{i}2} = 3.75 \times 10^4$	$k'_{\mathrm{i}2} = 3.75 \times 10^4$

effectively restore the system with smallest active power oscillations. In contrast, the transient response of FLSMC is unsatisfactory as its design is sensitive to system parameter variations. Response of perturbation estimation is demonstrated in Fig. 3.7, which shows the observers can estimate the perturbations with a fast tracking rate.

3) Case 3: Weak AC grid connection: The AC grids are assumed to be sufficiently strong such that AC bus voltages are ideal constants. It is worth considering a weak AC grid connected to the rectifier, e.g., offshore wind farms, which voltage $u_{\mathrm{s}1}$ is no longer a constant but a time-varying function. A voltage fluctuation occurs from 0.15 s to 1.05 s caused by the wind speed variation is simulated, which corresponds to $u_{\mathrm{s}1} = 1 + 0.15\sin(0.2\pi t)$. System responses are presented in Fig. 3.9, it illustrates that both DC voltage and reactive power are oscillatory, while POSMC can effectively suppress the oscillation with the smallest fluctuation of DC voltage and reactive power.

4) Case 4: System parameter uncertainties: When there is a fault in the transmission or distribution grid, the resistance and inductance values of the grid may change

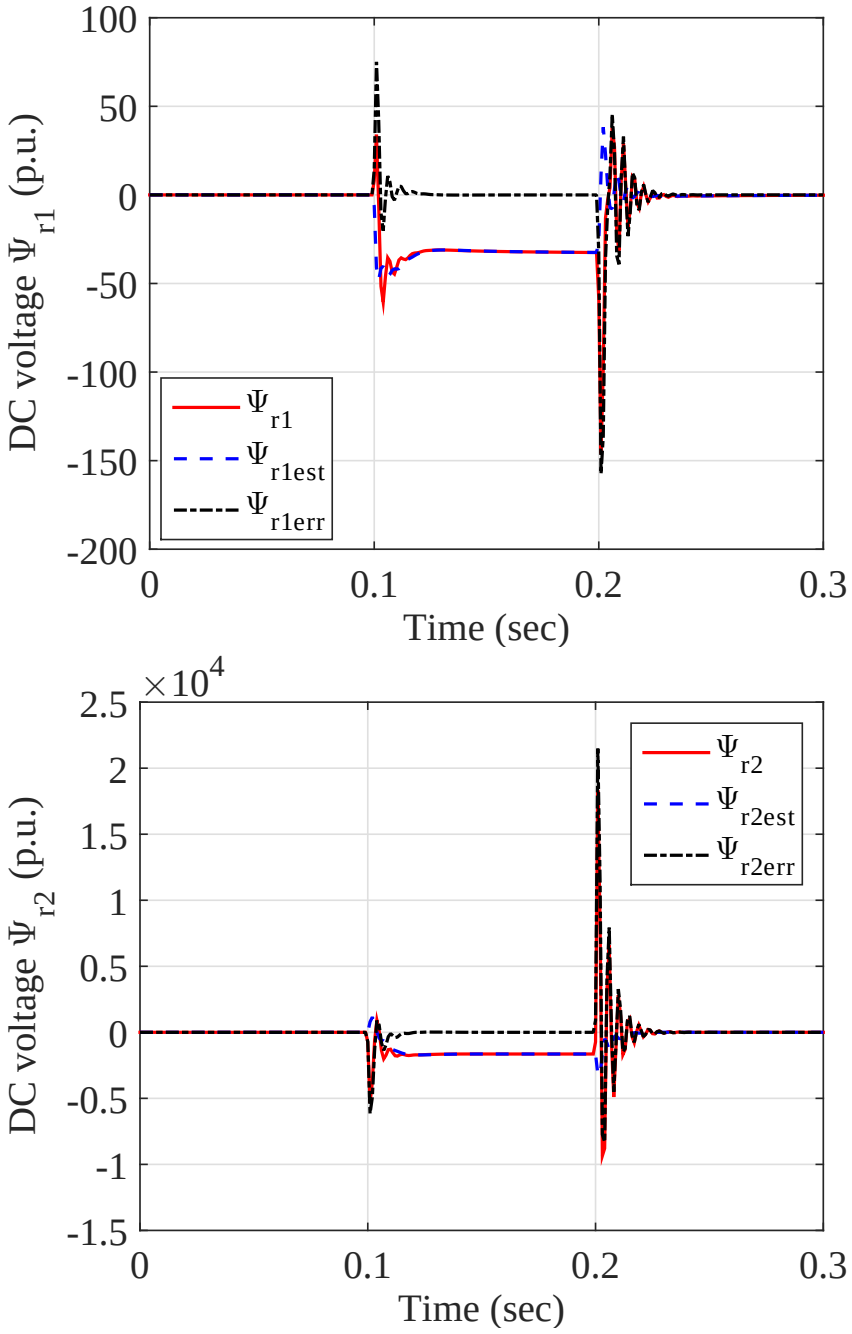

Figure 3.7: Estimation errors of the perturbations obtained under the 5-cycle LLLG fault at AC bus 1.

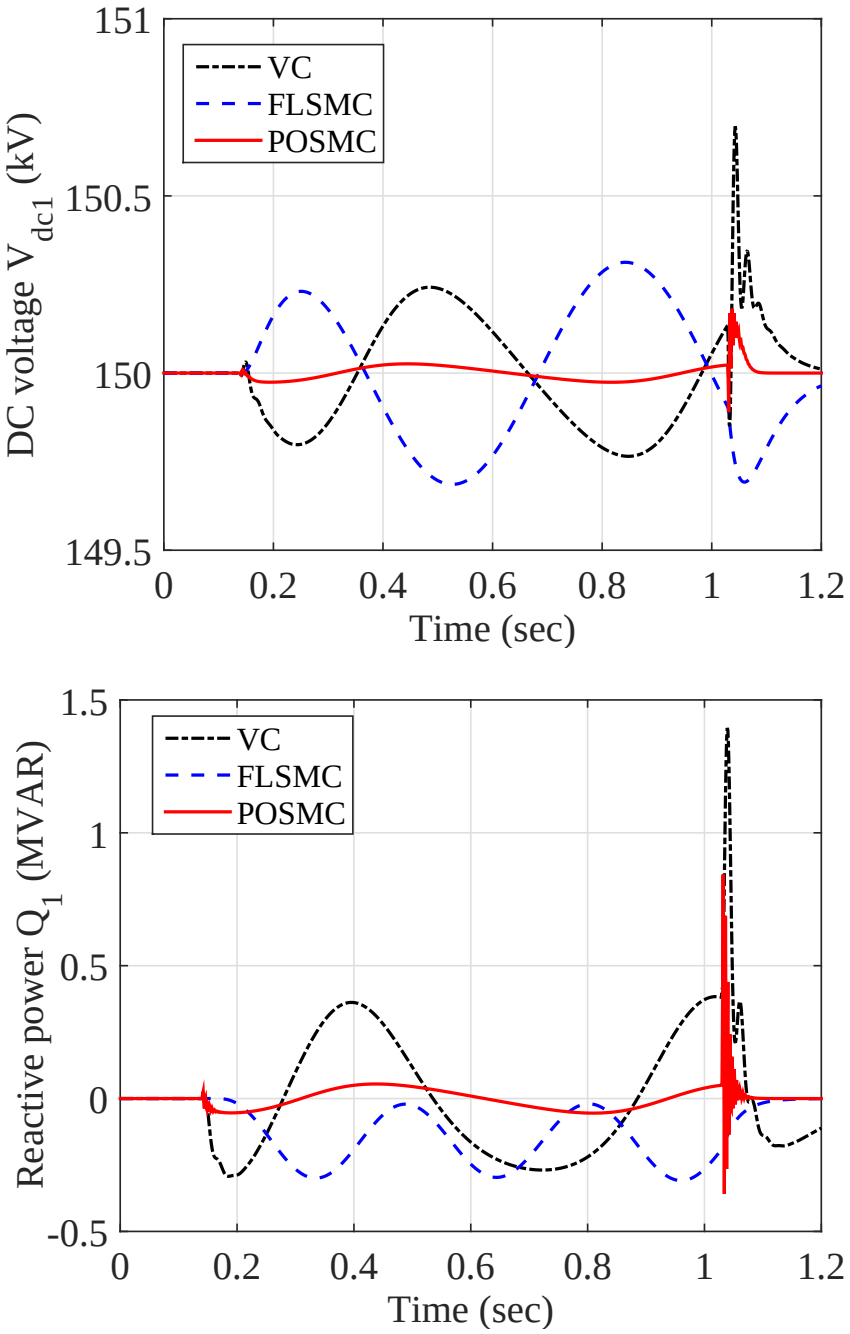

Figure 3.8: System responses obtained with the weak AC grid connection-1.

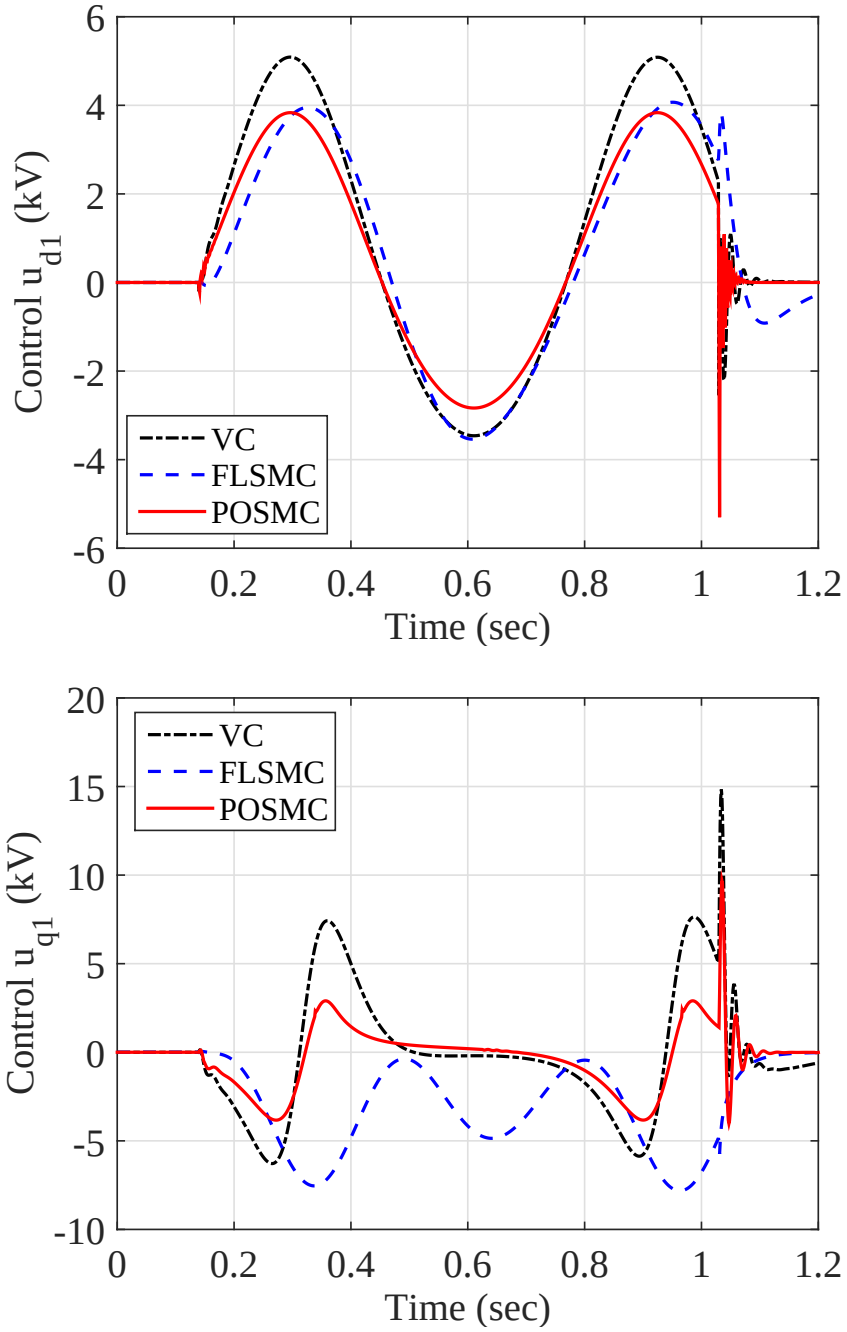

Figure 3.9: System responses obtained with the weak AC grid connection-2.

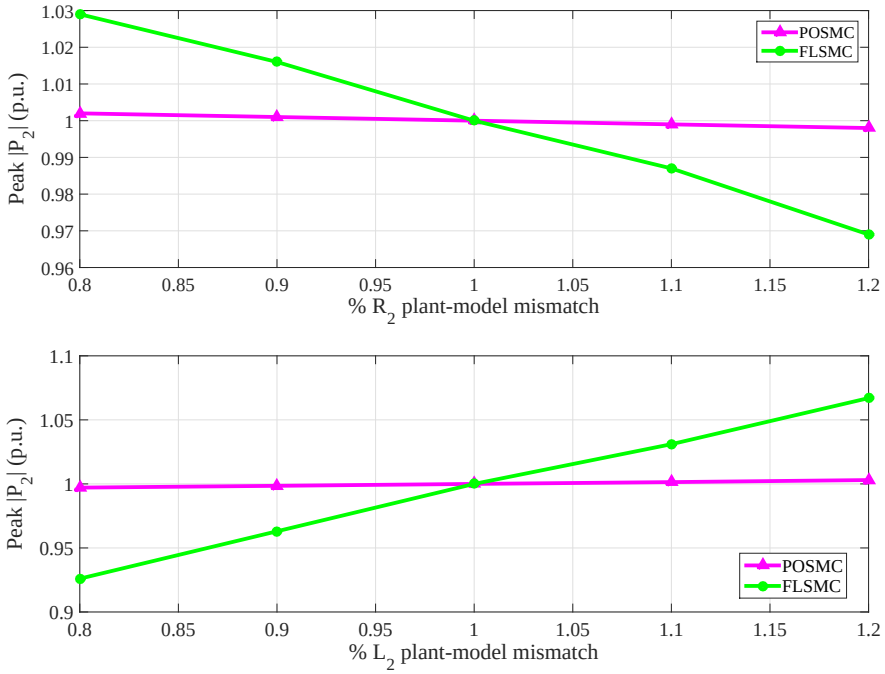

Figure 3.10: The peak active power $|P_2|$ (in p.u.) to a -120 A in the DC cable current i_{L} at nominal grid voltage for plant-model mismatches in the range of 20% (one parameter changes and others keep constant).

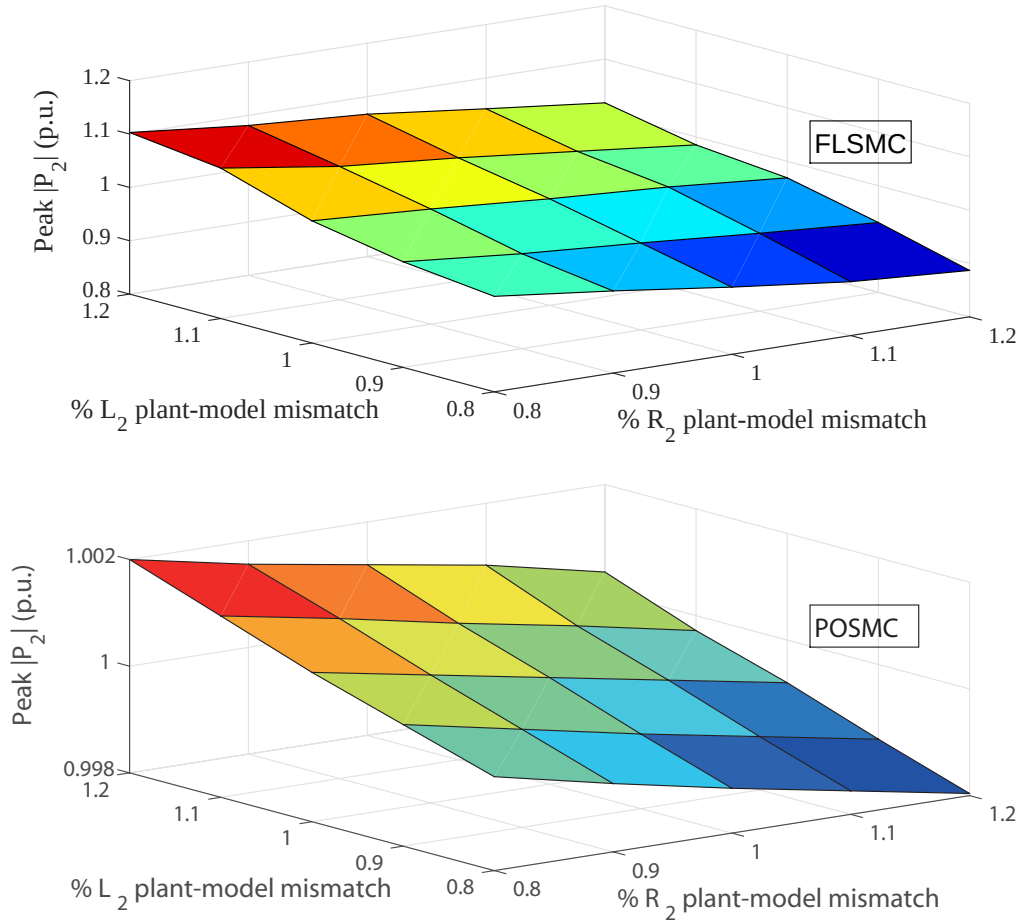

Figure 3.11: The peak active power $|P_2|$ (in p.u.) to a -120 A in the DC cable current i_{L} at nominal grid voltage for plant-model mismatches in the range of 20% (different parameters may change at the same time).

significantly. Several simulations are performed for plant-model mismatches of R_2 and L_2 with $\pm 20\%$ uncertainties. All tests are undertaken under the nominal grid voltage and a corresponding -120 A in the DC cable current i_{L} at 0.1 s. The peak active power $|P_2|$ is recorded which uses per unit (p.u.) value for a clear illustration of system robustness. It can be found from Fig. 3.10 that the peak active power $|P_2|$ controlled by POSMC is almost not affected, while FLSMC has relatively large range of variation, i.e., around 3% to R_2 and 8% to L_2, respectively. Responses to mismatch of R_2 and L_2 changing at the same time are illustrated in Fig. 3.11. The magnitude of changes is around 10% under FLSMC and almost does not change under POSMC. This is because POSMC estimates all uncertainties and does not need an accurate system model and thus has better robustness than that of FLSMC which requires the accurate system parameters.

Table 3.3: IAE indices (in p.u.) of different control schemes calculated in case studies

Method \ Case	Power tracking			
	$\mathrm{IAE_{Q_1}}$	$\mathrm{IAE_{V_{dc1}}}$	$\mathrm{IAE_{Q_2}}$	$\mathrm{IAE_{P_2}}$
VC	3.83E-02	4.44E-03	2.13E-02	2.71E-02
FLSMC	2.19E-02	1.73E-03	2.23E-02	2.18E-02
POSMC	2.33E-02	2.00E-03	2.42E-02	2.33E-02
Method \ Case	5-cycle LLLG fault		Weak AC grid connection	
	$\mathrm{IAE_{Q_1}}$	$\mathrm{IAE_{V_{dc1}}}$	$\mathrm{IAE_{Q_1}}$	$\mathrm{IAE_{V_{dc1}}}$
VC	2.62E-02	2.15E-03	4.53E-03	4.13E-03
FLSMC	1.13E-02	4.13E-03	4.08E-03	3.33E-03
POSMC	5.64E-03	1.38E-03	3.88E-04	6.78E-04

The integral of absolute error (IAE) indices of each approach calculated in case studies are tabulated in Table 5.3. Here $\mathrm{IAE}_{Q_1} = \int_0^T |Q_1 - Q_1^*|\mathrm{d}t$, $\mathrm{IAE}_{V_{\mathrm{dc1}}} = \int_0^T |V_{\mathrm{dc1}} - V_{\mathrm{dc1}}^*|\mathrm{d}t$, $\mathrm{IAE}_{Q_2} = \int_0^T |Q_2 - Q_2^*|\mathrm{d}t$ and $\mathrm{IAE}_{P_2} = \int_0^T |P_2 - P_2^*|\mathrm{d}t$. The simulation time T=3 s. Note that POSMC has a little bit higher IAE than that of FLSMC in the power tracking due to the estimation error, while it can provide much

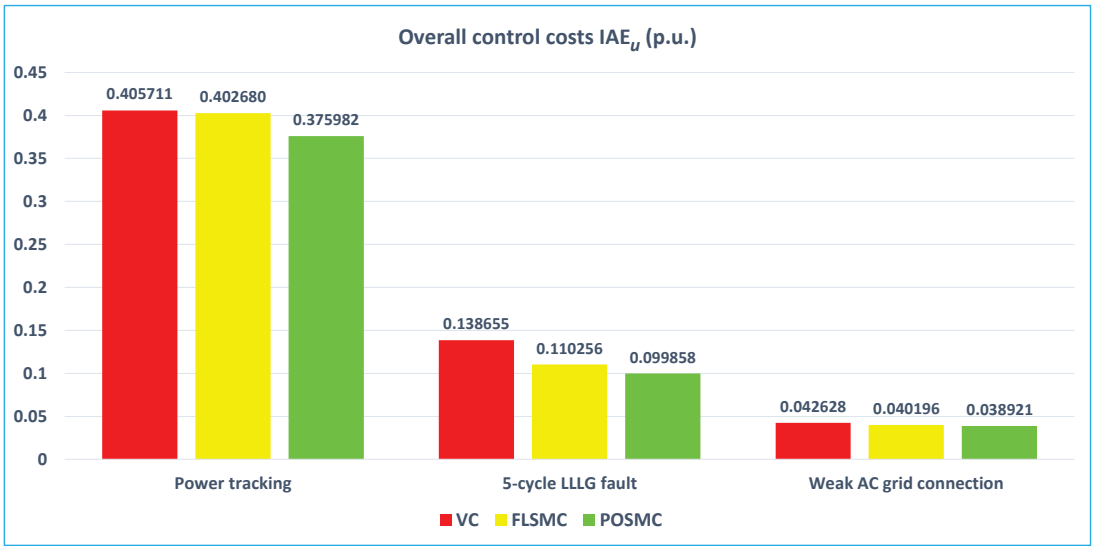

Figure 3.12: Overall control costs $\mathrm{IAE_u}$ (in p.u.) obtained in three cases.

better robustness in the case of 5-cycle LLLG fault and weak AC grid connection. In particular, its IAE_{Q_1} and $\mathrm{IAE}_{V_{\mathrm{dc1}}}$ are only 8.57% and 9.51% of those of VC, 16.42% and 20.36% of those of FLSMC with the weak AC grid connection. The overall control costs are illustrated in Fig. 3.12, with $\mathrm{IAE}_u = \int_0^T (|u_{\mathrm{d1}}| + |u_{\mathrm{q1}}| + |u_{\mathrm{d2}}| + |u_{\mathrm{q2}}|)\mathrm{d}t$. It is obvious that POSMC has the lowest control costs in all cases, which is resulted from the merits that the upper bound of perturbation is replaced by the smaller bound of its estimation error, thus an over-conservative control input can be avoided.

3.5 Hardware-in-the-loop Test Results

A dSPACE simulator based HIL test is used to validate the implementation feasibility of POSMC, which configuration and experiment platform are given by Fig. 3.13 and Fig. 5.11, respectively. The rectifier controller (5.3.7) and inverter controller (5.3.16) are implemented on one dSPACE platform (DS1104 board) with a sampling frequency $f_{\mathrm{c}} = 1$ kHz, and the VSC-HVDC system is simulated on another dSPACE platform (DS1006 board) with the limit sampling frequency $f_{\mathrm{s}} = 50$ kHz to make HIL simulator as close to the real plant as possible. The measurements

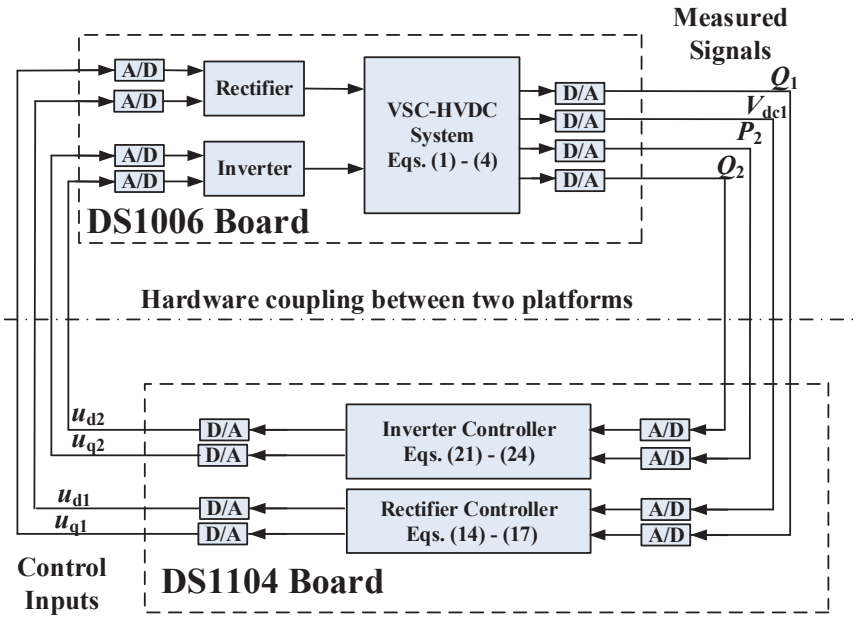

Figure 3.13: The configuration of the HIL test.

of the reactive power Q_1, DC voltage V_{dc1}, active power P_2 and reactive power Q_2 are obtained from the real-time simulation of the VSC-HVDC system on the DS1006 board, which are sent to two controllers implemented on the DS1104 board for the control inputs calculation.

It has been found from the author's previous work that an unexpected high-frequency oscillation in control inputs may emerge as the large observer poles would result in high gains, which lead to highly sensitive observer dynamics to the measurement disturbances in the HIL test [61]. Note that this phenomenon does not exist in the simulation. One effective way to alleviate such malignant effect is to reduce the observer poles. Through trial-and-error, an observer pole in the range of $\lambda_{\alpha_{\mathrm{r}}} \in [15, 25]$ and $\lambda_{\alpha'_{\mathrm{r}}} = \lambda_{\alpha_{\mathrm{i}}} = \lambda_{\alpha'_{\mathrm{i}}} \in [3, 10]$ can avoid such oscillation but with almost similar transient responses, thus the reduced poles $\lambda_{\alpha_{\mathrm{r}}} = 20$ and $\lambda_{\alpha'_{\mathrm{r}}} = \lambda_{\alpha_{\mathrm{i}}} = \lambda_{\alpha'_{\mathrm{i}}} = 5$, with $b_{\mathrm{r10}} = 50$, $b_{\mathrm{r20}} = 5000$, $b_{\mathrm{i10}} = 20$, and $b_{\mathrm{i20}} = 20$, are chosen in the HIL test.

1) Case 1: Active and reactive power tracking: The references of active and reactive power changes at $t = 0.4$ s, $t = 0.9$ s, and restores to the original value at $t = 1.4$ s, while DC voltage is regulated at the rated value $V^*_{\mathrm{dc1}} = 150$ kV. The

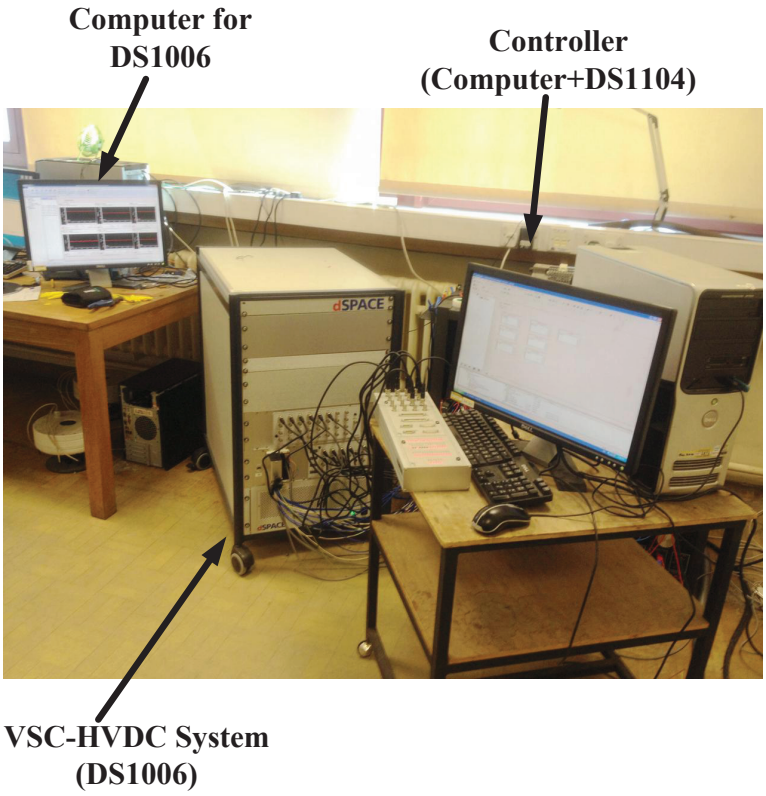

Figure 3.14: The experiment platform of the HIL test.

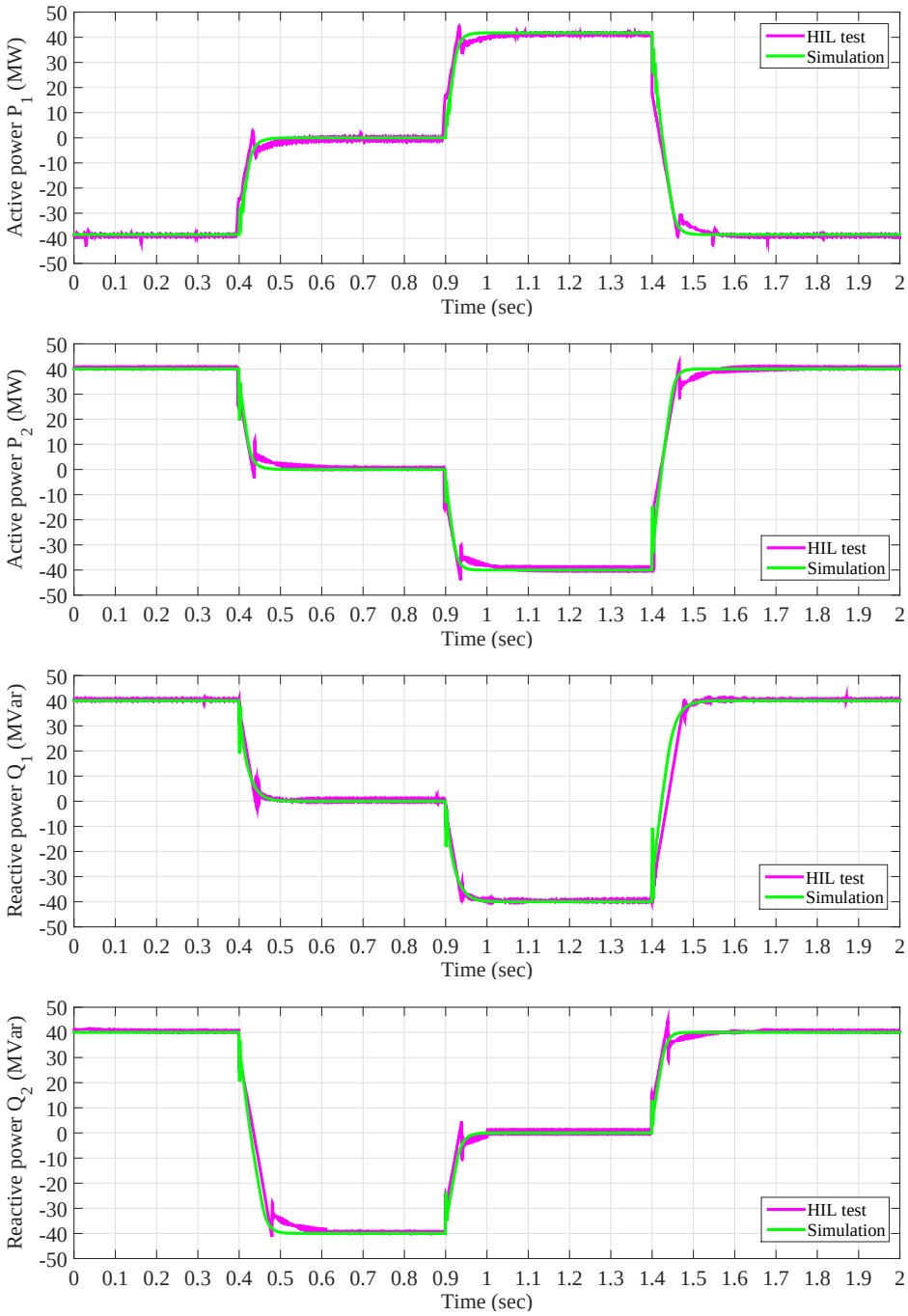

Figure 3.15: HIL test results of system responses obtained under the active and reactive power tracking.

system responses obtained under the HIL test and simulation are illustrated by Fig. 5.12, which shows that the HIL test have almost the same results as that of the simulation.

2) Case 2: 5-cycle line-line-line-ground (LLLG) fault at AC bus 1. A 5-cycle LLLG fault occurs at AC bus 1 when $t = 0.1$ s. Fig. 5.13 demonstrates that the system can be rapidly restored and the system responses obtained by the HIL test is similar to that of simulation.

3) Case 3: Weak AC grid connection: The same voltage variation on u_{s1} is applied between 0.87 s to 2.45 s. It can be readily seen from Fig. 3.17 that the results of the HIL test and simulation match very well.

The difference of the obtained results between the HIL test and simulation is possibly due to the following three reasons:

- There exist measurement disturbances in the HIL test which are however not taken into account in the simulation, a filter could be used to remove the measurement disturbances thus the control performance can be improved.
- The discretization of the HIL test and sampling holding may bring in an additional amount of error compared to that of the continuous control used in the simulation.
- The computational delay of the real-time controller, in which the accurate computational delay is difficult to obtain. A time delay $\tau = 3$ ms has been assumed and added in the simulation to consider the effect of the computational delay.

3.6 Conclusion

This chapter has developed a POSMC scheme based on ESO for the VSC-HVDC system. The combinatorial effect of nonlinearities, parameter uncertainties, unmodelled dynamics and time-varying external disturbances is aggregated into a perturbation, which is estimated and compensated online. As the upper bound

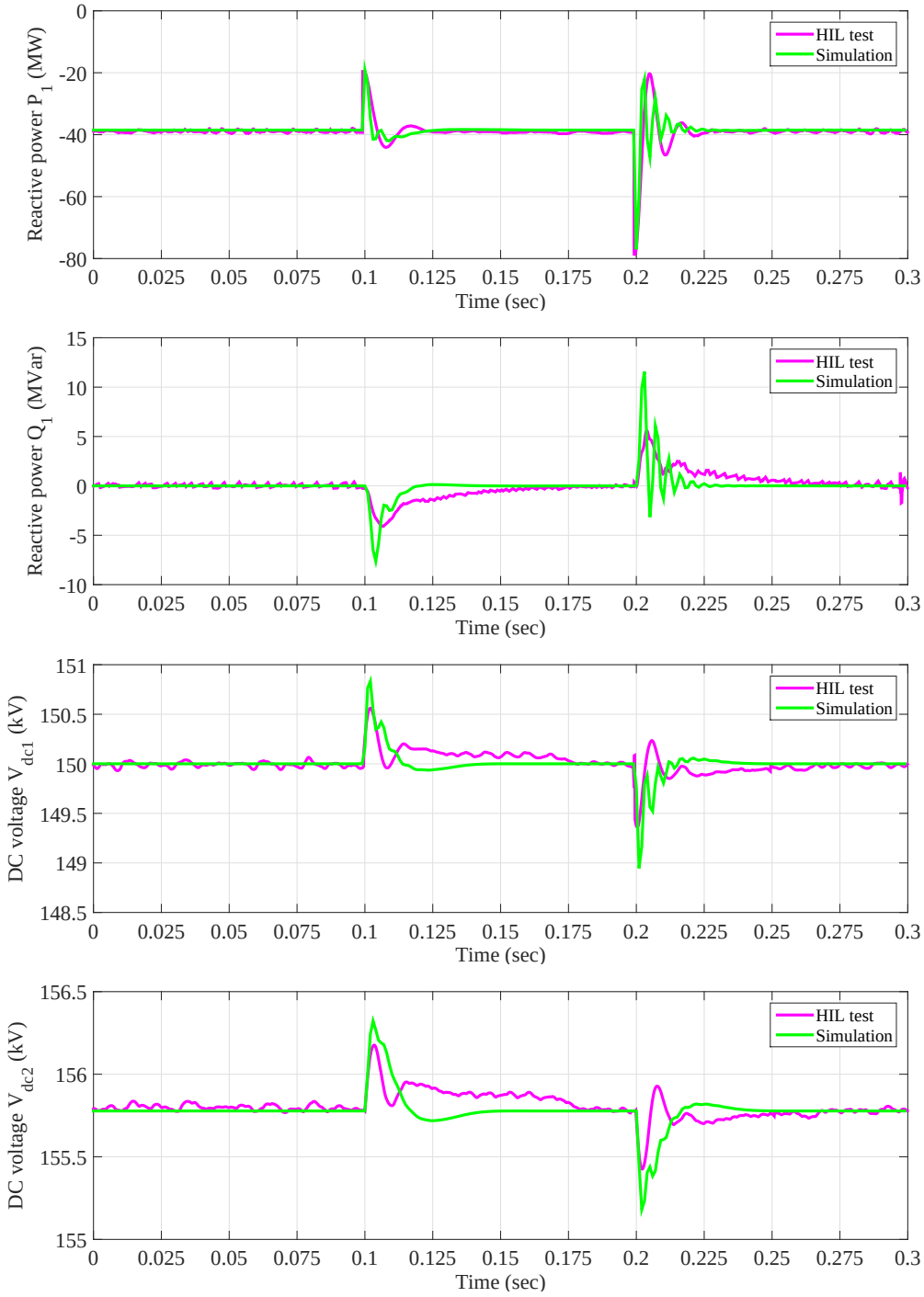

Figure 3.16: HIL test results of system responses obtained under the 5-cycle LLLG fault at AC bus 1.

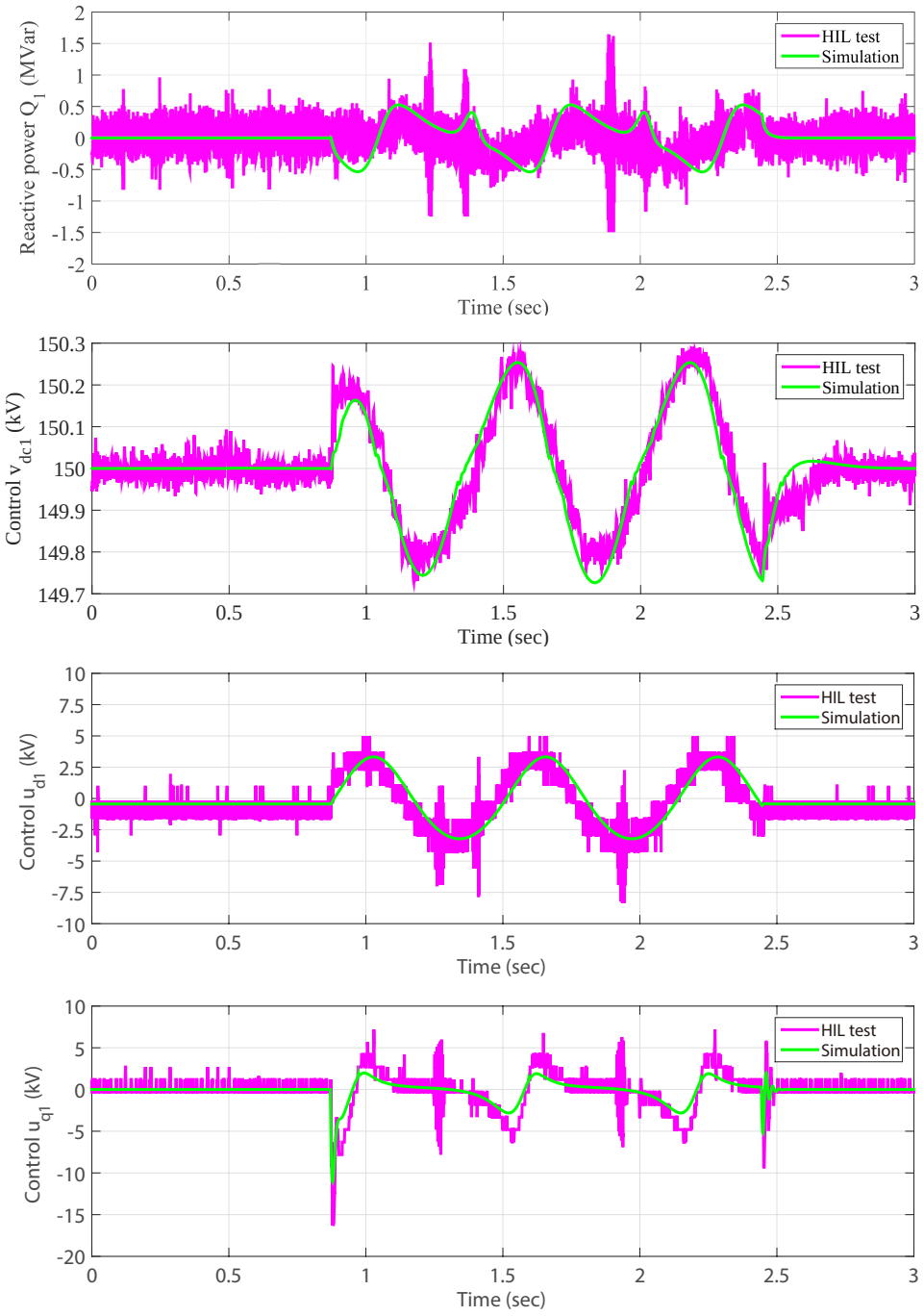

Figure 3.17: HIL test results of system responses obtained with the weak AC grid connection.

of perturbation is replaced by the smaller bound of its estimation error, an over-conservative control input is avoided such that the tracking accuracy can be improved. POSMC does not require an accurate system model and only the active and reactive power, and DC voltage need to be measured. Four case studies have been undertaken to evaluate the control performance of the proposed approach, including active and reactive power tracking, AC bus fault, system parameter uncertainties and weak AC gird connection. Simulation results verify that POSMC can maintain a consistent control performance and provide significant robustness under various operation conditions. An HIL test has been carried out to validate the implementation feasibility of the proposed approach.

As presented in this chapter, the POSMC based control strategy is applied to the point-to-point VSC-HVDC system for bulk power transmission, and corresponding dynamic performance has been improved. In the next chapter, the control strategy which is applied to VSC-HVDC system for offshore wind farm integration will be modified for enhancing system fault ride-through capability.

Chapter 4

Nonlinear Adaptive Control for Fault Ride-Through Capability Enhancement of VSC-HVDC Transmission Systems with Offshore Wind Farm Integration

4.1 Introduction

In the past decade, the ratings of offshore wind farm are increasing rapidly and being planned far from grid connection point [106]. However, the conventional AC transmission through submarine cables produce significant amount of reactive current due to its high capacitance which reduces current-carrying capacity and often require extra reactive power compensation devices [131].

Voltage-source converter based high voltage direct current (VSC-HVDC) transmission system is the favorable solution for offshore DC connection since that it does not require a strong offshore or onshore AC grid and can even start up against a dead network (black-start capability). VSC-HVDC transmission system also allows the independent control of active and reactive power, which reduces the requirement

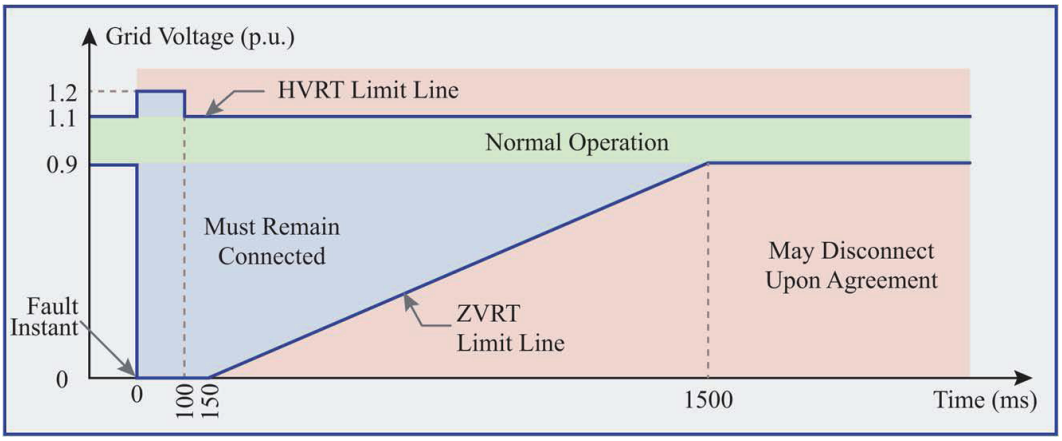

Figure 4.1: FRT profiles according to E.ON regulation [110]

for reactive-power compensation and is able to contribute to the stabilization of the connected onshore AC grid [107].

However, one inevitable challenge for VSC-HVDC transmission systems which are applied for integrating offshore wind farm is the fault ride-through (FRT) capability which is stipulated by grid codes [108]. FRT capability enables offshore wind farm to be remained connected during abnormal onshore AC grid conditions like voltage deviations [109]. Fig. 4.1 demonstrates a FRT time-voltage profiles set by the German Transmission and Distribution Utility (E.ON) regulation [110]. The FRT requirement is a broad category covering zero voltage ride-through (ZVRT), low-voltage ride-through (LVRT) and high-voltage ride-through (HVRT). The ZVRT and LVRT are the investigation objectives in this chapter.Fig. 4.2 demonstrates the reactive current requirement for supporting grid voltage during grid failure according to German grid code [111]. Although FRT attracted many research works, most of them are mainly studying FRT capability of individual wind turbine and these proposed works all caused considerable efforts in large-scale wind farm which is formed by huge amounts of wind turbine. Investigating FRT capability on VSC-HVDC transmission system is regarded as a smarter way. There are two major types of approaches to enhance the FRT capability, one for control improvement and the other one for hardware modification.

FRT capability can be enhanced by installing additional protection devices, such

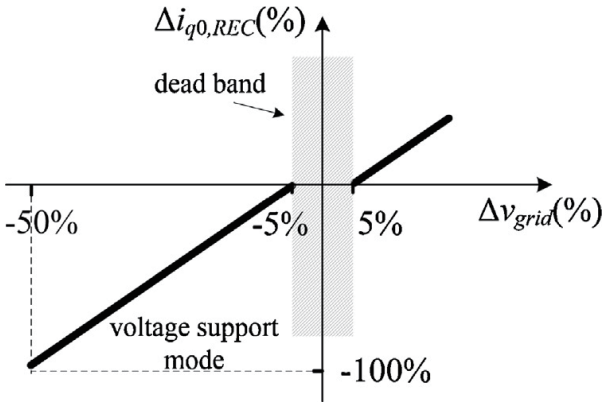

Figure 4.2: Required reactive current for voltage support according to German grid code [111]

as DC choppers with braking resistors [106], flywheel energy storage system [112] and novel topology like nine switch converter [113]. Installing extra devices used for providing voltage compensation, energy consumption or storage are effective yet being limited by the high cost and heat dissipation capacity. These methods also bring the complicated control of energy storage circuits or novel converter. Another effective alternative putting forward to enhance the FRT of the HVDC is to modifying the control strategies applied on the converters. In [114], fuzzy logic controller for temporary blocking the VSC converter is proposed during AC grid fault. However even when the insulated gate bipolar transistors (IGBTs) in the sending-end VSC are blocked, the reverse current flowing via antiparallel diodes will still cause the power transmitting to the DC side [113]. Different control strategies are applied for power reduction (de-loading strategies) to enhance the FRT performance but are designed based on linear mode like mentioned in [115, 106, 116, 117]. However, existing linear approaches can not provide consistently satisfactory performance since that they are all tuned specially based on one operation point and the time-varying nonlinearities and uncertainties are not being fully compensated. Due to the poor off standard operation point behavior during AC network faults, inrush faulty grid-side current can not be limited rapidly and may cause converter components damaged since that the power electronics in converter are very sensitive to transient current surges [118]. Feedback linearizing control (FLC) has been proposed in [118] for solving the nonlinearity problem to improve the FRT performance of in-

dividual wind turbine. However, the FLC requires the accurate system model and hence FLC will degrade dramatically in the presence of parameter uncertainties and external disturbances which has adverse impacts on FRT performance. On the other hand, most FLC based controllers require full state feedback and many measured variables to calculate the nonlinear controller. Since co-operating with de-loading strategy will introduce more parameter uncertainties and disturbances caused by transients of slower mechanical response and can hardly provide real-time full state feedback, FLC is not suitable to be applied to this application. To solve these issues occurs with applying FLC, extended-order state and perturbation observer (ESPO) based nonlinear adaptive controller is proposed which using estimate of perturbation to compensate real perturbation and achieve the adaptive feedback linearizing control.

In order to fulfill the FRT requirement for offshore wind farm integration and effectively reduce the extremely high transient current when the grid voltage dips to zero during faults, this chapter develops a perturbation estimation based nonlinear adaptive control (NAC) scheme with proper de-loading strategy for the FRT capability enhancement of VSC-HVDC systems. The combinatorial effect of nonlinearities, system parameter uncertainties and external disturbances is aggregated into a perturbation, which is estimated by a high-gain perturbation observer (HGPO) [119, 120, 121]. NAC is proposed to solve the nonlinearity problem and considered as the suitable method to enhance the FRT capability with de-loading strategy. NAC-based VSC-HVDC converter controller only requires the measurement of active and reactive power and DC voltage, thus it provides the merit of inherently easy implementation in real systems. The effectiveness of proposed strategy is verified by simulation under several cases, e.g., voltage sags and LLLG faults. Robustnesses against system parameter uncertainties and control efforts of conventional converter vector control (VC) without de-loading strategy, conventional VC with de-loading control and proposed NAC-based converter control with de-loading control are analysing and comparing. Then the proposed controller is compiled and downloaded into the dSPACE processor for hardware-in-the-loop (HIL) test, in which the I/O interface of dSPACE simulator enables the real-time sampling of inputs from

measurements and output control signals with detailed system plant models. HIL test results validate the implementation feasibility of the proposed approach with measurement communication noises and unmodelled dynamics.

4.2 System Configuration and Modelling

Fig. 4.3 shows the typical configuration of the offshore wind farm need to be integrated. The model of the wind power plants in the offshore wind farm are represented by one aggregated wind turbine model which behaves like the sum of all of them. Hence the typical point to point VSC-HVDC transmission system with wind power integrated is shown in Fig. 5.5. The wind power generated is transmitted from sending end VSC station (SEC) which regulates the active and reactive power to the receiving end VSC station (REC) which maintains the DC voltage and regulates reactive power. The reactive power control channel is used to support the grid voltage during faults. The VSC state-space representation [88] in VSC-HVDC transmission system after Park transformation into *dq*-axis:

$$\begin{cases} L\frac{\mathrm{d}i_\mathrm{d}}{\mathrm{d}t} = -Ri_\mathrm{d} + \omega L i_\mathrm{q} + V_\mathrm{sd} - V_\mathrm{cd} \\ L\frac{\mathrm{d}i_\mathrm{q}}{\mathrm{d}t} = -Ri_\mathrm{q} - \omega L i_\mathrm{d} + V_\mathrm{sq} - V_\mathrm{cq} \end{cases} \tag{4.2.1}$$

where i_d and i_q are the *dq* components of current at point of common coupling (PCC), u_sd and u_sq are the *dq* components of voltage at PCC, u_cd and u_cq are the *dq* components of voltage at VSC terminal, R and L are the equivalent series resistance and inductance of the filter and transformer between the VSC terminal and corresponding PCC.

The instantaneous active power and reactive power at PCC can be expressed as follows without considering the power losses during the switching process:

$$\begin{cases} P(t) = \frac{3}{2}(V_\mathrm{sq} i_\mathrm{q} + V_\mathrm{sd} i_\mathrm{d}) \\ Q(t) = \frac{3}{2}(V_\mathrm{sq} i_\mathrm{d} - V_\mathrm{sd} i_\mathrm{q}) \end{cases} \tag{4.2.2}$$

The DC cables in VSC-HVDC transmission system are modelled as a nominal Pi configuration which use approximated lumped-parameter models which are ex-

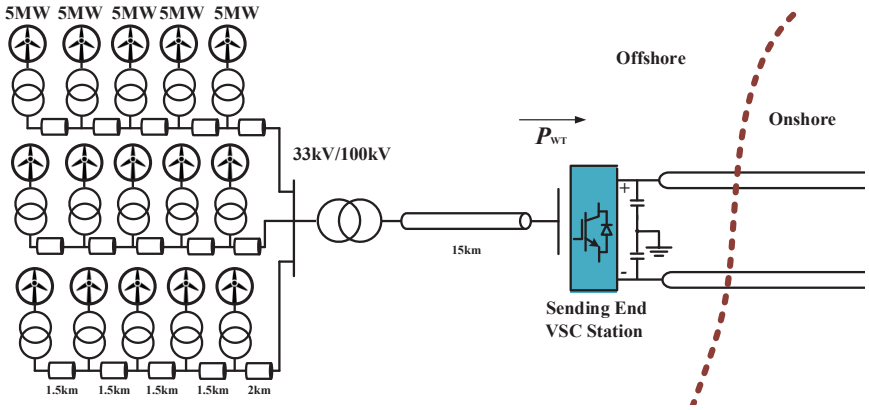

Figure 4.3: The configuration of the offshore wind farm that need to be integrated

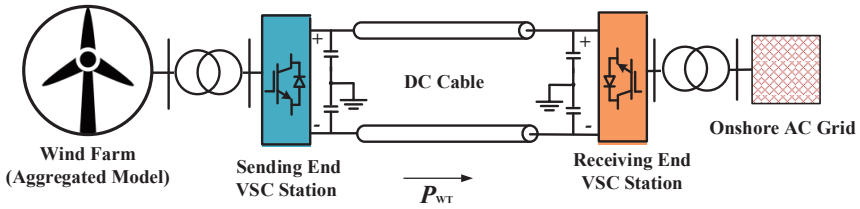

Figure 4.4: The configuration of the VSC-HVDC system

pressed as following;

$$\begin{cases} \frac{\mathrm{d}V_{\mathrm{dc}}}{\mathrm{d}t} = \frac{1}{V_{\mathrm{dc}}C_{dc}}P(t) - \frac{1}{C_{\mathrm{dc}}}I_{\mathrm{dc}} \\ \frac{\mathrm{d}I_{\mathrm{dc}}}{\mathrm{d}t} = \frac{1}{L_{\mathrm{dc}}}\Delta V_{\mathrm{dc}} - \frac{R_{\mathrm{dc}}}{L_{\mathrm{dc}}}I_{\mathrm{dc}} \end{cases} \tag{4.2.3}$$

where ΔV_{dc} is the DC voltage difference between VSC terminals, C_{dc} is one equivalent DC cable capacitance which is divided equivalently from cable shunt capacitance, each placed at the sending and receiving ends of the cable, I_{dc} is the current flowing through DC cables, R_{dc} and L_{dc} are the resistance and inductance of DC cable. The Phase-locked loops (PLL) is assumed in a steady state, therefore V_{sq} equals 0 [122]. The global mathematical model of overall VSC-HVDC system is expressed as follows;

$$\begin{cases} \frac{\mathrm{d}i_{\mathrm{d1}}}{\mathrm{d}t} = -\frac{R_1}{L_1}i_{\mathrm{d1}} + \omega i_{\mathrm{q1}} + \frac{V_{\mathrm{sd1}}-V_{\mathrm{cd1}}}{L_1} \\ \frac{\mathrm{d}i_{\mathrm{q1}}}{\mathrm{d}t} = -\frac{R_1}{L_1}i_{\mathrm{q1}} - \omega i_{\mathrm{d1}} - \frac{V_{\mathrm{cq1}}}{L_1} \\ \frac{\mathrm{d}i_{\mathrm{d2}}}{\mathrm{d}t} = -\frac{R_2}{L_2}i_{\mathrm{d2}} + \omega i_{\mathrm{q2}} + \frac{V_{\mathrm{sd2}}-V_{\mathrm{cd2}}}{L_2} \\ \frac{\mathrm{d}i_{\mathrm{q2}}}{\mathrm{d}t} = -\frac{R_2}{L_2}i_{\mathrm{q2}} - \omega i_{\mathrm{d2}} - \frac{V_{\mathrm{cq2}}}{L_2} \\ \frac{\mathrm{d}V_{\mathrm{dc1}}}{\mathrm{d}t} = \frac{3V_{\mathrm{sq1}}i_{\mathrm{q1}}}{2C_{\mathrm{dc1}}V_{\mathrm{dc1}}} - \frac{I_{\mathrm{dc}}}{C_{\mathrm{dc1}}} \\ \frac{\mathrm{d}V_{\mathrm{dc2}}}{\mathrm{d}t} = \frac{3V_{\mathrm{sq2}}i_{\mathrm{q2}}}{2C_{\mathrm{dc2}}V_{\mathrm{dc2}}} - \frac{I_{\mathrm{dc}}}{C_{\mathrm{dc2}}} \\ \frac{\mathrm{d}I_{\mathrm{dc}}}{\mathrm{d}t} = \frac{1}{L_{\mathrm{dc}}}(V_{\mathrm{dc1}} - V_{\mathrm{dc2}}) - \frac{R_{\mathrm{dc}}}{L_{\mathrm{dc}}}I_{\mathrm{dc}} \end{cases} \tag{4.2.4}$$

The active and reactive powers entering both REC and SEC can be expressed as;

$$\begin{cases} P_1 = \frac{3}{2}\left(V_{\mathrm{sq1}}i_{\mathrm{q1}} + V_{\mathrm{sd1}}i_{\mathrm{d1}}\right) = \frac{3}{2}V_{\mathrm{sq1}}i_{\mathrm{q1}} \\ Q_1 = \frac{3}{2}\left(V_{\mathrm{sq1}}i_{\mathrm{d1}} - V_{\mathrm{sd1}}i_{\mathrm{q1}}\right) = \frac{3}{2}V_{\mathrm{sq1}}i_{\mathrm{d1}} \\ P_2 = \frac{3}{2}\left(V_{\mathrm{sq2}}i_{\mathrm{q2}} + V_{\mathrm{sd2}}i_{\mathrm{d2}}\right) = \frac{3}{2}V_{\mathrm{sq2}}i_{\mathrm{q2}} \\ Q_2 = \frac{3}{2}\left(V_{\mathrm{sq2}}i_{\mathrm{d2}} - V_{\mathrm{sd2}}i_{\mathrm{q2}}\right) = \frac{3}{2}V_{\mathrm{sq2}}i_{\mathrm{d2}} \end{cases} \tag{4.2.5}$$

where number 1, 2 subscript denote the variable corresponding to REC and SEC. Type-4 WECS configuration owns second highest share now and is announced by the wind turbine manufacturers that the this type technology would take over the wind energy market in coming years [110]. Type-4 WECS configuration is attractive for the use of full-scale power converters as shown in Fig. 4.5. The permanent magnetic synchronous generator (PMSG), wound rotor synchronous generator (WRSG), and squirrel cage induction generator (SCIG) have all found applications

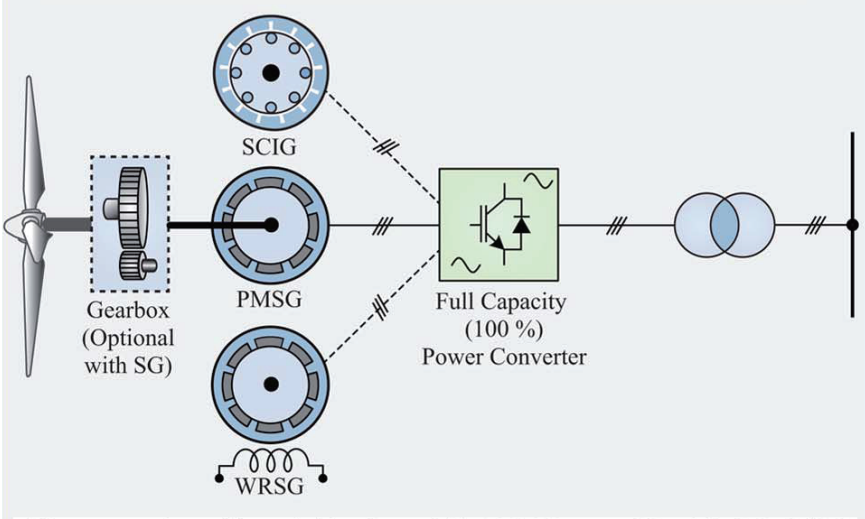

Figure 4.5: The configuration of the Type-4 WECS with SCIG and SG [110]

in this type of configuration with a power rating of up to several megawatts. PMSG is chosen as the investigated objective.

With the full-scale power converters, the generator is theoretically fully decoupled from the grid and operated at full speed range. The adopted power converters can also support the grid with reactive power compensation and smooth grid connection. This configuration can also provide the highest wind energy conversion efficiency comparing with other types. For FRT capability without installing external hardware devices, best compliance can be achieved with full-scale power converters comparing with other types. However, the FRT capability is still required to be improved for that mechanical system response is much slower than the electrical response, and thus the transient active power injected by wind turbine is critical to the stability of whole system. The extra injected power which is called as surplus energy needs to be handled carefully. There is various proposed strategy , and the adopted strategy is described in the next section.

The equivalent aggregated type-4 wind turbine generator with PMSG model [123, 124] is applied for simulation as shown below. The mechanical power P_m extracted by the wind turbine is expressed by

$$P_{\mathrm{m}} = \frac{1}{2}\rho A_{\mathrm{r}} c_{\mathrm{p}}(\lambda, \theta) v_{\omega}^{3} \tag{4.2.6}$$

where P_m is the power extracted from the wind, ρ is air density, A_{r} is the area covered by the rotor, v_ω is the wind speed, and c_{p} is the performance coefficient or power coefficient. Within c_{p}, θ is the pitch angle of rotor blades, λ is the tip speed ratio which $\lambda = \frac{v_{\mathrm{t}}}{v_\omega}$. Where v_{t} is blade tip speed.

$$c_{\mathrm{p}}(\lambda, \theta) = 0.73(\frac{151}{\lambda_i} - 0.58\theta - 0.002\theta^{2.14} - 13.2)e^{-18.4/\lambda_i} \tag{4.2.7}$$

Where

$$\lambda_i = \frac{1}{\frac{1}{\lambda - 0.02\theta} - \frac{0.003}{\theta^3 + 1}} \tag{4.2.8}$$

Under normal operation, the dynamics of shaft system and mechanical torque are expressed by

$$T_{\mathrm{m}} - T_{\mathrm{e}} - D\omega_{\mathrm{m}} = 2H\frac{\mathrm{d}\omega_{\mathrm{m}}}{\mathrm{dt}} \tag{4.2.9}$$

$$T_{\mathrm{e}} = p[(L_{\mathrm{d}} - L_{\mathrm{q}})i_{\mathrm{d}}i_{\mathrm{q}} + \phi_{\mathrm{m}}i_{\mathrm{q}}] \tag{4.2.10}$$

$$T_{\mathrm{m}} = \frac{1}{2\lambda^3}\rho\pi R^5 c_{\mathrm{p}}(\lambda, \theta)\omega_{\mathrm{m}}^2 \tag{4.2.11}$$

where T_{m} is the mechanical torque, T_{e} is generator electrical torque, ω_{m} is mechanical rotation speed of wind turbine, H is the summation of wind turbine inertia constant and generator inertia constant. D is the viscous damping coefficient which is taken to be 0 here, L_{d} and L_{q} are the inductances in the $d-q$ axis, ψ_{m} is the permanent magnetic flux given by the magnets, R is the blade radius of wind turbine and p is the number of pole pairs.

The equivalent circuit model of the studied wind turbine generator can be expressed in $d-q$ axis, which the q-axis is fixed on the machine rotor and rotates at rotor speed,

$$\begin{cases} V_{\mathrm{d}} = i_{\mathrm{d}}R_{\mathrm{s}} + L_{\mathrm{d}}\frac{\mathrm{di_d}}{\mathrm{dt}} - \omega_{\mathrm{e}}L_{\mathrm{q}}i_{\mathrm{q}} \\ V_{\mathrm{q}} = i_{\mathrm{q}}R_{\mathrm{s}} + L_{\mathrm{q}}\frac{\mathrm{di_q}}{\mathrm{dt}} - \omega_{\mathrm{e}}(L_{\mathrm{d}}i_{\mathrm{d}} + \phi_{\mathrm{m}}) \end{cases} \tag{4.2.12}$$

where V_{d} and V_{q} are the stator voltages in the $d-q$ axis, i_{d} and i_{q} are the currents in the $d-q$ axis, R_{s} is the stator resistance, ω_{e} is electrical rotation speed which equals $p\omega_{\mathrm{m}}$.

4.3 Design for Proposed FRT Capability Enhancement Strategy

This section presents the design of the perturbation observer based NAC. For each subsystem in the VSC-HVDC transmission system with wind farm integrated, a lumped perturbation terms is defined to contain all time-varying external disturbances, subsystem nonlinearities and interactions between subsystems. Extended-order high-gain state and perturbation observers are employed in the adaptive linearization and decoupled control to estimate each subsystem state and perturbation term. The estimates are implemented via introducing fictitious states. The design of the proposed NAC is illustrated in the following subsections.

4.3.1 The high-gain state and perturbation observer

Consider a canonical control form of studied system as follows

$$\begin{cases} \dot{x}_1 &= x_2 \\ &\vdots \\ \dot{x}_n &= f(x) + g(x)u \\ y &= x_1 \end{cases} \tag{4.3.1}$$

and define a fictitious state to represent the system perturbation, i.e., $x_{n+1} = \Psi$, this transforms the state equation into

$$\begin{cases} \dot{x}_1 &= x_2 \\ &\vdots \\ \dot{x}_n &= x_{n+1} + g_0 u \\ \dot{x}_{n+1} &= \dot{\Psi}(\cdot) \\ y &= x_1 \end{cases} \tag{4.3.2}$$

where $\Psi = f(x) + [g(x) - g_0]u$, g_0 is the nominal control gain. The following assumptions are made on the system (4.3.2).

A.1. g_0 is chosen to satisfy: $|g(x)/g_0 - 1| \leq \theta < 1$, where θ is a positive constant.

A.2. The function $\Psi(x, u, t) : R^n \times R \times R^+ \to R$ and $\dot{\Psi}(x, u, t) : R^n \times R \times R^+ \to R$

are locally Lipschitz in their arguments over the domain of interest and are globally bounded in x:

$$\mid \Psi(x,u,t) \mid \leq \gamma_1, \quad \mid \dot{\Psi}(x,u,t) \mid \leq \gamma_2 \tag{4.3.3}$$

where γ_1 and γ_2 are positive constants. In addition, $\Psi(0,0,0) = 0$ and $\dot{\Psi}(0,0,0) = 0$. Assumption $A.2$ guarantees that the origin is an equilibrium point of the open-loop system.

Here the high-gain observer in [119] is employed to obtain the on-line estimate of the perturbation. Under the assumptions $A.1$ and $A.2$, $f(x)$ and $g(x)$ are unknown continuous functions. Assume only one state $x_1 = y$ is available, a (n+1)th-order HGSPO can be designed as

$$\begin{cases} \dot{\hat{x}}_1 &= \hat{x}_2 + h_1(y - \hat{x}_1) \\ & \cdots \\ \dot{\hat{x}}_n &= \hat{x}_{n+1} + h_n(y - \hat{x}_1) + g_0 u \\ \dot{\hat{x}}_{n+1} &= h_{n+1}(y - \hat{x}_1), \end{cases} \tag{4.3.4}$$

where $h_i = \alpha_i/\epsilon^i$, $i = 1, \cdots, n+1$ are gains of the observer, $\epsilon \ll 1$ is a positive constant to be specified and the positive constants α_i, $i = 1, \cdots, n+1$, are chosen such that the roots of

$$s^{n+1} + \alpha_1 s^n + \cdots + \alpha_n s + \alpha_{n+1} = 0 \tag{4.3.5}$$

are in the open left-half complex plan.

4.3.2 NAC for VSC-HVDC transmission system

The proposed NAC uses the estimate of perturbation term $\Psi(\cdot)$ to compensate the real system perturbation and achieves the adaptive feedback linearizing control, without requiring a detailed and accurate system model in conventional feedback linearization control. The more details can be found in previous work [125, 119, 126]. Throughout this thesis, $\hat{x}$ is denoted as the estimate of x.

For the REC side, the system output is chosen as $y_{\rm rec} = [y_{\rm rec1}, y_{\rm rec2}]^{\rm T} = [Q_1 - Q_1^*, V_{\rm dc1} - V_{\rm dc1}^*]^{\rm T}$, where Q_1^* and $V_{\rm dc1}^*$ are the reference values of reactive power Q_1

and DC voltage V_{dc1}, respectively. Hence the DC voltage level can be maintained and the reactive power can be controlled and be used to support the main onshore grid voltage during fault. Differentiate y_{rec} until the control input appears explicitly, it yields

$$\dot{y}_{\mathrm{rec1}} = \Psi_{\mathrm{rec1}} + b_{\mathrm{rec10}} u_{\mathrm{recd}} \tag{4.3.6}$$

$$\ddot{y}_{\mathrm{rec2}} = \Psi_{\mathrm{rec2}} + b_{\mathrm{rec20}} u_{\mathrm{recq}} \tag{4.3.7}$$

where b_{rec10} and b_{rec20} are constant control gains. The perturbations are given as follows

$$\begin{aligned}
\Psi_{\mathrm{rec1}} &= \frac{3u_{\mathrm{sq1}}}{2}\left(-\frac{R_1}{L_1} i_{\mathrm{d1}} + \omega i_{\mathrm{q1}}\right) - \dot{Q}_1^* + \frac{3u_{\mathrm{sq1}}}{2L_1} u_{\mathrm{recd}} - b_{\mathrm{rec10}} u_{\mathrm{recd}} \\
\Psi_{\mathrm{rec2}} &= \frac{3u_{\mathrm{sq1}}}{2C_1 V_{\mathrm{dc1}}}\left(-\omega i_{\mathrm{d1}} - \frac{R_1}{L_1} i_{\mathrm{q1}} - \frac{i_{\mathrm{q1}}}{V_{\mathrm{dc1}}}\left(\frac{3u_{\mathrm{sq1}} i_{\mathrm{q1}}}{2C_1 V_{\mathrm{dc1}}} - \frac{i_{\mathrm{L}}}{C_1}\right)\right) \\
&\quad - \frac{\dot{i}_{\mathrm{L}}}{C_1} - \ddot{V}_{\mathrm{dc1}}^* + \frac{3u_{\mathrm{sq1}}}{2C_1 L_1 V_{\mathrm{dc1}}} u_{\mathrm{recq}} - b_{\mathrm{rec20}} u_{\mathrm{recq}}
\end{aligned}$$

A second-order high-gain perturbation observer (HGPO) [119] is designed to estimate Ψ_{rec1} as

$$\begin{cases}
\dot{\hat{Q}}_1 = \hat{\Psi}_{\mathrm{rec1}} + \frac{\alpha_{\mathrm{rec1}}}{\epsilon}(Q_1 - \hat{Q}_1) + b_{\mathrm{rec10}} u_{\mathrm{recd}} \\
\dot{\hat{\Psi}}_{\mathrm{rec1}} = \frac{\alpha_{\mathrm{rec2}}}{\epsilon^2}(Q_{\mathrm{rec}} - \hat{Q}_1)
\end{cases} \tag{4.3.8}$$

A third-order high-gain state and perturbation observer (HGSPO) [119] is designed to estimate Ψ_{rec2} as

$$\begin{cases}
\dot{\hat{V}}_{\mathrm{dc1}} = \frac{\alpha'_{\mathrm{rec1}}}{\epsilon}(V_{\mathrm{dc1}} - \hat{V}_{\mathrm{dc1}}) \\
\ddot{\hat{V}}_{\mathrm{dc1}} = \hat{\Psi}_{\mathrm{rec2}} + \frac{\alpha'_{\mathrm{rec2}}}{\epsilon^2}(V_{\mathrm{dc1}} - \hat{V}_{\mathrm{dc1}}) + b_{\mathrm{rec20}} u_{\mathrm{recq}} \\
\dot{\hat{\Psi}}_{\mathrm{rec2}} = \frac{\alpha'_{\mathrm{rec3}}}{\epsilon^3}(V_{\mathrm{dc1}} - \hat{V}_{\mathrm{dc1}})
\end{cases} \tag{4.3.9}$$

where α_{rec1}, α_{rec2}, α'_{rec1}, α'_{rec2}, and α'_{rec3} are the positive constants and $1 \gg \epsilon > 0$.

The NAC for the rectifier side using the estimates of perturbation is designed as

$$\begin{cases}
u_{\mathrm{recd}} = b_{\mathrm{rec10}}^{-1}(-\hat{\Psi}_{\mathrm{rec1}} - k_{\mathrm{rec1}}(\hat{Q}_1 - Q_1^*) + \dot{Q}_1^*) \\
u_{\mathrm{recq}} = b_{\mathrm{rec20}}^{-1}[-\hat{\Psi}_{\mathrm{rec2}} - k'_{\mathrm{rec1}}(\hat{V}_{\mathrm{dc1}} - V_{\mathrm{dc1}}^*) - k'_{\mathrm{rec2}}(\dot{\hat{V}}_{\mathrm{dc1}} - \dot{V}_{\mathrm{dc1}}^*) \\
\quad + \ddot{V}_{\mathrm{dc1}}^*]
\end{cases} \tag{4.3.10}$$

where k_{rec1}, k'_{rec1} and k'_{rec2} are positive feedback control gains, which place the poles of the closed-loop system in the left-half plane (LHP).

For the SEC side, the system output is chosen as $y_{\mathrm{sec}} = [y_{\mathrm{sec1}}, y_{\mathrm{sec2}}]^{\mathrm{T}} = [Q_2 - Q_2^*, P_2 - P_2^*]^{\mathrm{T}}$, where Q_2^* and P_2^* are the reference values of reactive power Q_2 and active power P_2, respectively. Differentiate y_{sec} until the control input appears explicitly, it yields

$$\dot{y}_{\mathrm{sec1}} = \Psi_{\mathrm{sec1}} + b_{\mathrm{sec10}} u_{\mathrm{secd}} \tag{4.3.11}$$

$$\dot{y}_{\mathrm{sec2}} = \Psi_{\mathrm{sec2}} + b_{\mathrm{sec20}} u_{\mathrm{secq}} \tag{4.3.12}$$

where b_{sec10} and b_{sec20} are constant control gains. The perturbations are given as follows

$$\Psi_{\mathrm{sq2}} = \frac{3u_{\mathrm{sec2}}}{2}\left(-\frac{R_2}{L_2} i_{\mathrm{d2}} + \omega i_{\mathrm{q2}}\right) - \dot{Q}_2^* + \frac{3u_{\mathrm{sq2}}}{2L_2} u_{\mathrm{secd}} - b_{\mathrm{sec10}} u_{\mathrm{secd}}$$

$$\Psi_{\mathrm{sq2}} = \frac{3u_{\mathrm{sec2}}}{2}\left(-\frac{R_2}{L_2} i_{\mathrm{q2}} - \omega i_{\mathrm{d2}}\right) - \dot{P}_2^* + \frac{3u_{\mathrm{sq2}}}{2L_2} u_{\mathrm{secq}} - b_{\mathrm{sec20}} u_{\mathrm{secq}}$$

Similarly, two second-order HGPOs are designed to estimate Ψ_{sec1} and Ψ_{sec2}, respectively:

$$\begin{cases} \dot{\hat{Q}}_2 = \hat{\Psi}_{\mathrm{sec1}} + \frac{\alpha_{\mathrm{sec1}}}{\epsilon}(Q_2 - \hat{Q}_2) + b_{\mathrm{sec10}} u_{\mathrm{secd}} \\ \dot{\hat{\Psi}}_{\mathrm{sec1}} = \frac{\alpha_{\mathrm{sec2}}}{\epsilon^2}(Q_2 - \hat{Q}_2) \end{cases} \tag{4.3.13}$$

$$\begin{cases} \dot{\hat{P}}_2 = \hat{\Psi}_{\mathrm{sec2}} + \frac{\alpha'_{\mathrm{sec1}}}{\epsilon}(P_2 - \hat{P}_2) + b_{\mathrm{sec20}} u_{\mathrm{secq}} \\ \dot{\hat{\Psi}}_{\mathrm{sec2}} = \frac{\alpha'_{\mathrm{sec2}}}{\epsilon^2}(P_2 - \hat{P}_2) \end{cases} \tag{4.3.14}$$

where α_{sec1}, α_{sec2}, α'_{sec1}, and α'_{sec2} are the positive constants.

The NAC for the inverter side using the estimates of perturbation is designed as

$$\begin{cases} u_{\mathrm{secd}} = b_{\mathrm{sec10}}^{-1}(-\hat{\Psi}_{\mathrm{sec1}} - k_{\mathrm{sec1}}(\hat{Q}_2 - Q_2^*) + \dot{Q}_2^*) \\ u_{\mathrm{secq}} = b_{\mathrm{sec20}}^{-1}(-\hat{\Psi}_{\mathrm{sec2}} - k'_{\mathrm{sec1}}(\hat{P}_2 - P_2^*) + \dot{P}_2^*) \end{cases} \tag{4.3.15}$$

where k_{sec1} and k'_{sec1} are positive feedback control gains, which place the poles of the closed-loop system in the LHP.

Notice that control laws (5.3.7) and (5.3.16) require only one state measurement for its control design, that is, the DC voltage V_{dc1}, active power P_2, reactive powers Q_1 and Q_2.

4.3.3 De-loading strategy of wind turbine generator

For the VSC-HVDC transmission system fault ride-through in the event of onshore main grid fault, the wind turbine generator power is required to be rapidly reduced (de-loaded) via reducing the reference generator torque or block the output powers via adjusting active power currents proportional to DC link voltage rise [106].

Since the DC link voltage is suppressed rapidly via adopting NAC in VSC controller of VSC-HVDC [127], DC link voltage rise can not be adopted for accurate de-loaded reference in linear vector control in WECS. Original AC grid voltage is required to be directly real-time measured and adopted in proposed de-loading strategy. As aforementioned, mechanical system response is much slower than the electrical response, mechanical rotation speed and mechanical torque adjustment is critical during de-loading strategy for FRT capability enhancement. The controllers of motor side converter (MSC) and grid side converter (GSC) in the type-4 wind turbine generator are very similar to the SEC and REC mentioned above. The design of detailed corresponding controllers is based on [121, 128]. The existing peak power tracking controller mentioned in [128] is designed to regulate the turbine rotating speed for capturing maximum wind. For proposed de-loading strategy, it is shifted to regulate another specific value according to the reference torque mentioned below rather than the value obtained by existing peak power tracking controller when fault being detected. The reference stator current in the $q-$ axis is calculated by set-point torque which is received by dictated order by de-loading strategy shown below. The droop gain in de-loading loop is multiplied by the torque demand coming from the 1p.u. which is set as the steady state AC voltage value. The proposed strategy is designed based on de-loading strategy mentioned in [116], but it replaced the increasing DC voltage by measured onshore main grid AC voltage directly. The reduction of reference electrical torque is still set as proportional to the difference of real-time measured faulty AC voltage and nominal AC voltage by de-loading droop.

$$\frac{T_{\mathrm{e}}^{*}}{T_{\mathrm{SP}}} = K_{\mathrm{d}} \frac{V_{\mathrm{sq2f}}}{V_{\mathrm{sq2n}}} \tag{4.3.16}$$

Where the T_{e}^{*} is the reference input for WECS controller, and the T_{SP} is the orig-

inal set-point torque output generated by maximum power point tracking (MPPT) look-up table. K_{d} is the droop gain applied in de-loading strategy. V_{sq2f} is the measured onshore main grid voltage in $q-$axis during fault. V_{sq2n} is the measured nominal onshore main grid voltage in $q-$axis. Hence the electrical power reference for WECS which also being sent to the HVDC SEC converter controller is obtained as flows

$$P_{\mathrm{e}}^{*} = K_{\mathrm{d}} T_{\mathrm{SP}} \omega_{\mathrm{e}} \frac{V_{\mathrm{sq2f}}}{V_{\mathrm{sq2n}}} \tag{4.3.17}$$

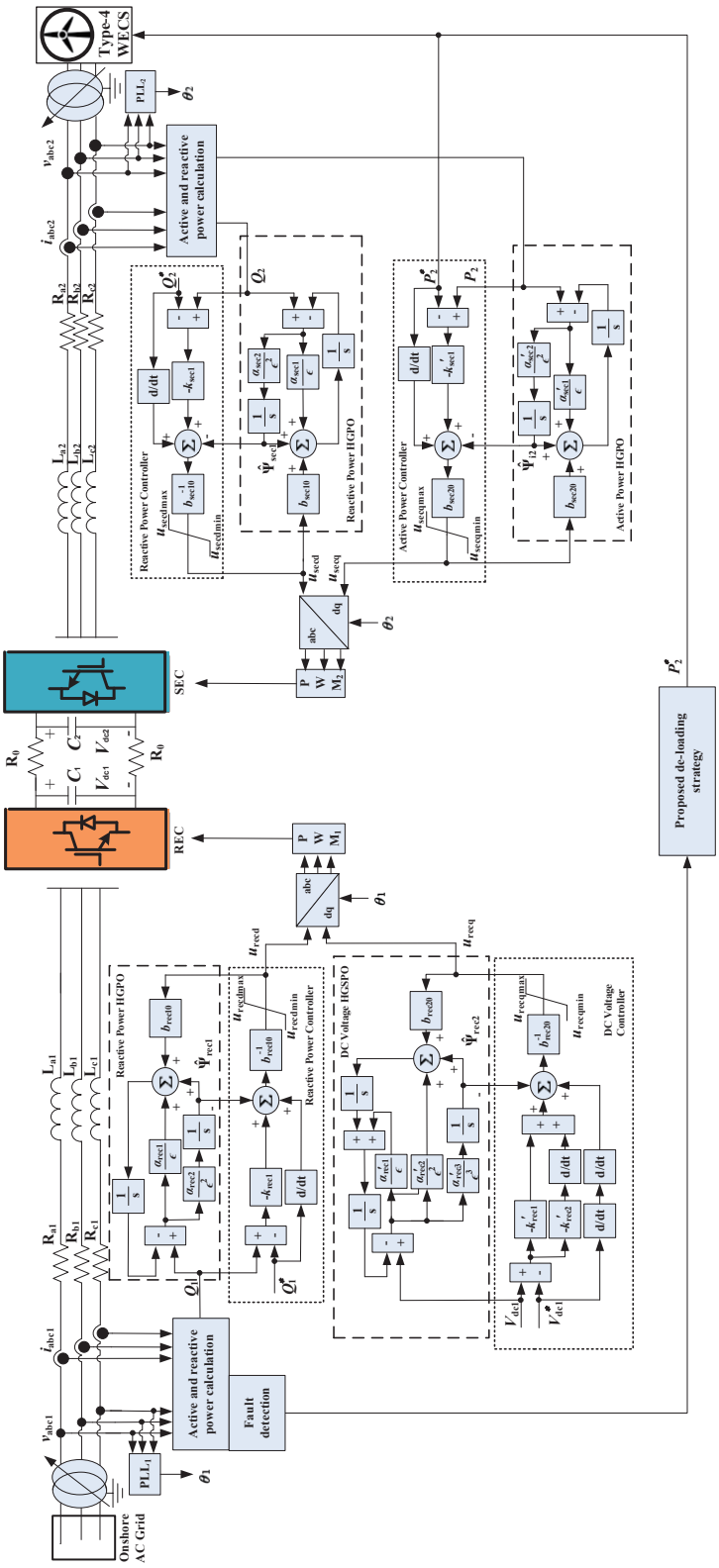

Figure 4.6: The overall control structure of NAC-based REC controller and SEC controller of the VSC-HVDC systems with type-4 WECS.

Table 4.1: System parameters used in the simulation

AC grids frequency	f	50 Hz
AC grids base voltage	$V_{\mathrm{AC}_{\mathrm{base}}}$	100 kV
DC cable base voltage	$V_{\mathrm{DC}_{\mathrm{base}}}$	150 kV
System base power	S_{base}	100 MVA
AC grids line resistance (25 km)	R_1, R_2	0.05 Ω/km
AC grids line inductance (25 km)	L_1, L_2	0.026 mH/km
DC cable resistance (50 km)	R_0	0.21 Ω/km
DC bus capacitance	C_1, C_2	11.94 μF

4.4 Case Studies

The proposed approach is applied on the system illustrated by Fig. 5.5. System parameters adopted in this thesis is set according to VSC-HVDC system benchmark shown in appendix which is widely accepted by industry and academia. Various research in literature review section like [76] and [116] which have been cited over a thousand times used the similar system to demonstrate the effectiveness of their proposed controllers. The FRT performance of proposed de-loading NAC is compared with that of conventional vector control (VC) [76] and de-loading VC [116].

The system parameters used in the simulation are listed in Table 5.1. The values of system variables are used in the per unit (p.u.) value. The NAC parameters illustrated in Table 3.2 are tuned considering for the application of de-loading strategy, while control inputs are bounded as $|u_{\mathrm{d}i}| \leq 1$ p.u. and $|u_{\mathrm{q}i}| \leq 1$ p.u., $i = 1, 2$, respectively. Moreover, the time period of the boundary values $\Delta = 0.05$ s.

Table 4.2: Controller parameters used in Chapter 4.

Rectifier controller			
Control gains	$k_{\mathrm{r1}} = 40$	$k'_{\mathrm{r1}} = 400$	$k'_{\mathrm{r2}} = 40$
	$b_{\mathrm{r10}} = 105$	$b_{\mathrm{r20}} = -3000$	$k'_{11} = 70$
Observer gains	$\alpha_{\mathrm{r1}} = 80$	$\alpha_{\mathrm{r2}} = 1600$	$\alpha'_{\mathrm{r1}} = 120$
	$\alpha'_{\mathrm{r2}} = 4800$	$\alpha'_{\mathrm{r3}} = 6.4 \times 10^4$	$\epsilon = 0.1$
Inverter controller			
Control gains	$k_{\mathrm{i1}} = 20$	$k'_{\mathrm{i1}} = 20$	$b_{\mathrm{i10}} = 100$
	$b_{\mathrm{i20}} = -100$		
Observer gains	$\alpha_{\mathrm{i1}} = 60$	$\alpha_{\mathrm{i2}} = 900$	$\alpha'_{\mathrm{i1}} = 60$
	$\alpha'_{\mathrm{i2}} = 900$	$\epsilon = 0.1$	

(1) *System response to voltage sag at onshore AC grid*: The FRT capability is tested with voltage sat at different reduced voltage levels. Take the voltage sag at 35% of nominal voltage as an example, the response comparison of using proposing de-loading NAC with de-loading VC and conventional VC without de-loading process is displayed in Fig. 4.8 and Fi.g 4.9. From analysing the response obtained from REC, it can be seen as the voltage sag occurs at 0.2 and lasts 0.3s. From comparing the overshoots in (b) (c) (d) of Fig. 4.8, the proposed de-loading NAC can provide most smooth performance during voltage sags. For better comparison, the AC current measured from REC is converted into the d-q axis and shown in (e) of Fig. 4.8. From comparing three control strategies in the d-q axis, it can be seen that proposed NAC could suppress current oscillations significantly. And with the help of de-loading strategy, the proposed control strategy can significantly reduce the peak current of the onshore grid. From analysing the response obtained from SEC which is shown in Fig. 4.9, the voltage of HVDC link can also be reduced significantly comparing with conventional controllers. Hence, the FRT capability is

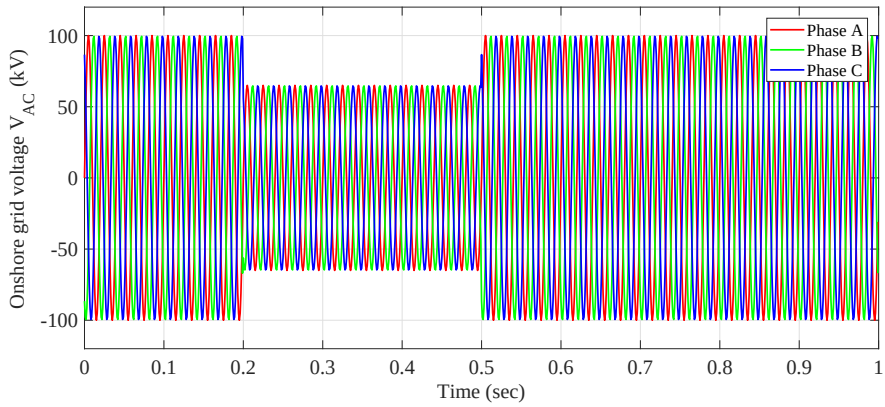

(a)

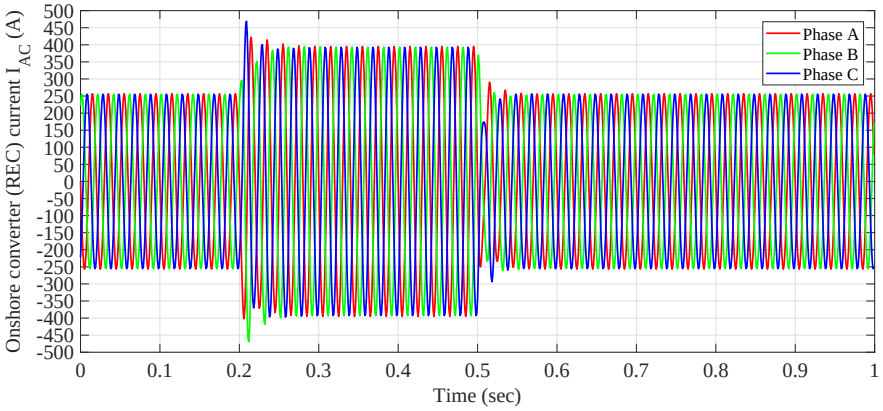

(b)

Figure 4.7: System responses obtained through REC with 35% voltage sag at onshore AC grid-1.

enhanced by proposed NAC de-loading strategy.

(2) *System response to line-line-line-ground (LLLG) fault at on shore AC bus*: In this section, more severe fault is considered for the grid codes of some states. For example, German grid code stipulate that all types of generating plants should remain connected during AC grid voltage reduced down to 0% for 150ms [110, 111]. From (a) of Fig. 4.10 it can be seen that a 0.15s LLLG fault is simulated at onshore AC bus from 0.2 s to 0.35 s. Due to the severe fault, the conventional VC without de-loading strategy or any extra FRT equipment loses the stability after fault finished because of extremely far operation point shift. From (b) of Fig. 4.10, it can be seen

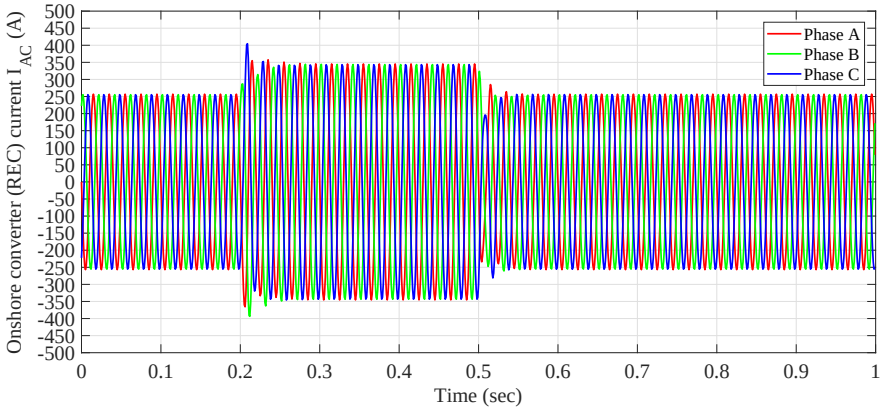

(a)

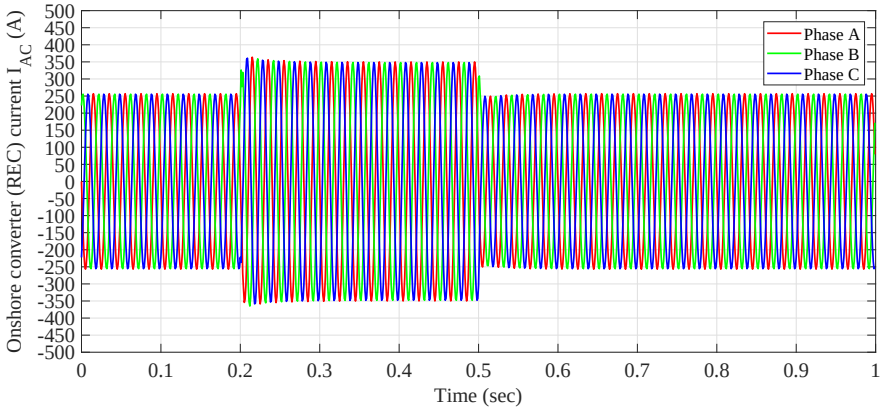

(b)

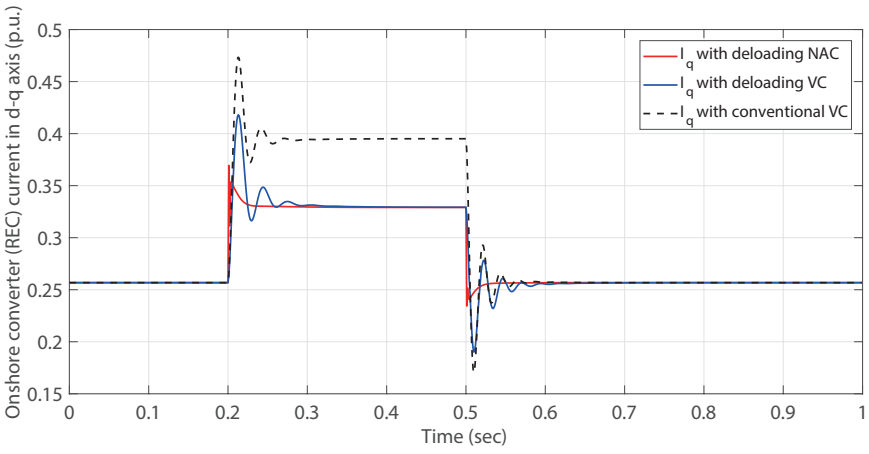

(c)

Figure 4.8: System responses obtained through REC with 35% voltage sag at onshore AC grid-2.

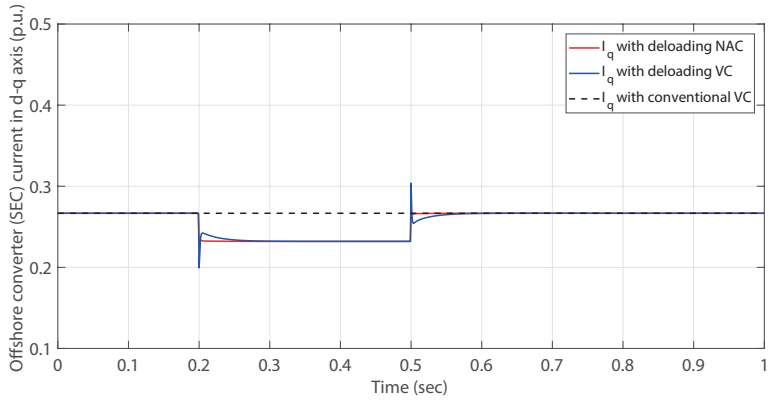

(a)

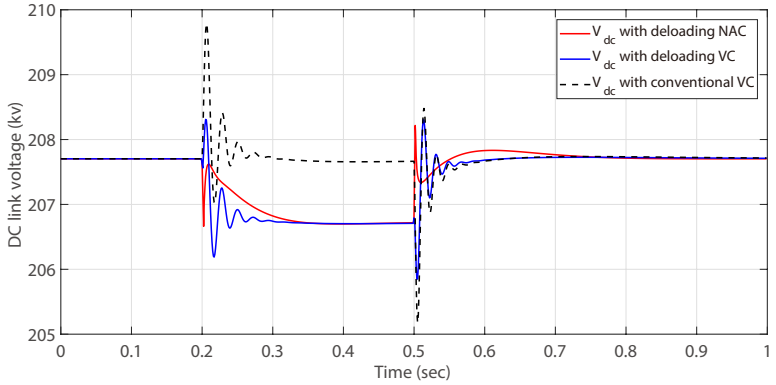

(b)

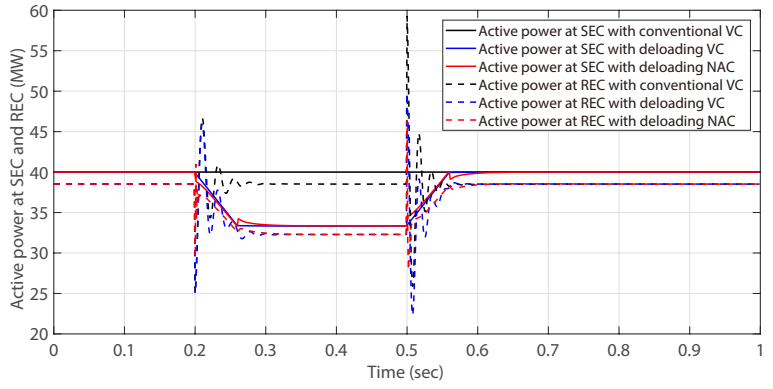

(c)

Figure 4.9: System responses obtained through SEC with 35% voltage sag at onshore AC grid.

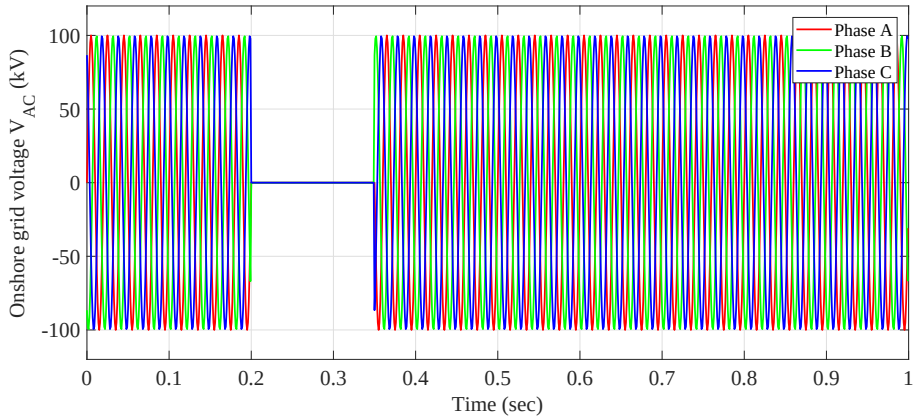

(a)

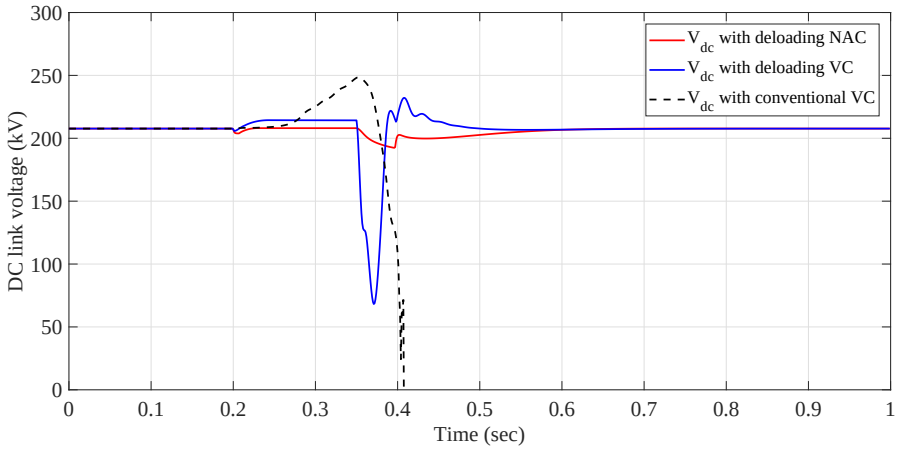

(b)

Figure 4.10: System responses obtained with 0.15s duration of LLLG fault at onshore AC grid.

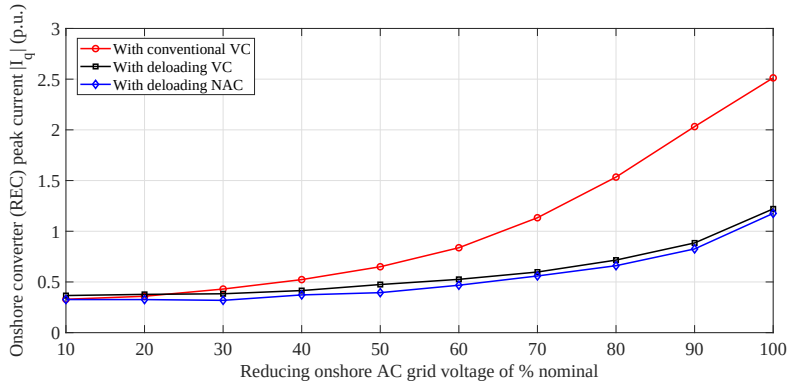

(a)

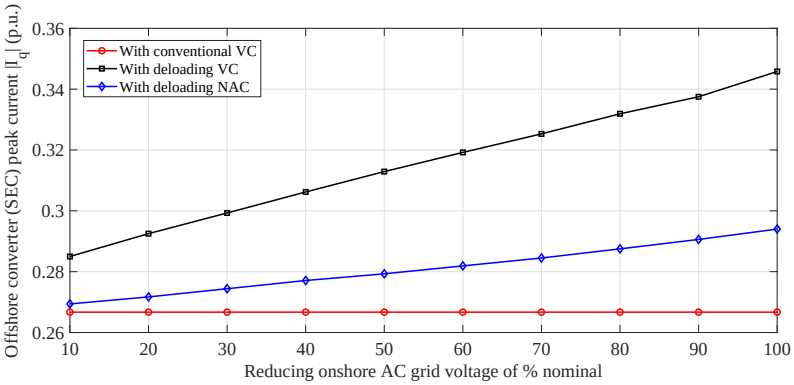

(b)

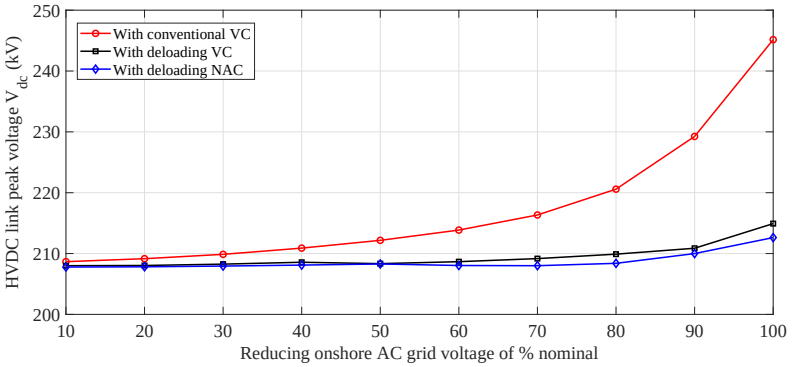

(c)

Figure 4.11: System responses obtained with 0.02s duration of different reduced voltage levels at onshore AC grid.

that the conventional VC can not recover the nominal HVDC link voltage after so long LLLG fault. From comparing the HVDC link voltage curve of de-loading VC and de-loading NAC, The proposed de-loading NAC is able to restore the system more rapidly with less voltage surge. Thus, NAC can significantly enhance the FRT capability of the VSC-HVDC systems with de-loading strategy.

(3) *System response to different reduced voltage levels at onshore AC grid*: For more comparing three methods in detail with numerical values, simulations with different reducing voltage levels from 100% to 10% at onshore AC grid are implemented in this section and displayed in Fig. 5.9. Since conventional control strategy can not restore the system and maintain stability after LLLG fault which is longer than 0.02s, it needs to be noticed that the fault in this part is selected to be cleared after 0.02s for whole range comparison which is different from the previous sections. For such short time fault, the proposed de-loading NAC can not present obvious advantage with de-loading VC in comparing currents at REC side and DC voltage. However the proposed strategy still can provide slightly improvement on them and especially significantly suppression on regulating currents at SEC side.

(4) *System response to AC grid with parameters variations*: Since the main AC grid is extremely complex which consists of large amounts of electrical devices with difficulties in fully detailed modelling like coupling reactors, transformers, AC filters different types of transmission lines or cables and REC itself, the parameter variation at onshore AC grid side is regards as common phenomenon due to temperature effects, minor internal faults, load change and aging of these components. The parameter variation will cause mismatched and uncertain equivalent line impedance in simulating system model. The robustness against AC grid parameter uncertainties is tested and the comparison of two de-loading control strategies is illustrated in this section. The mismatches on reactance and resistance will cause different equally severe impact on FRT performance. Hence different level of mismatches are also evaluated in this section. From (a) and (b) of Fig. 4.13 with the simulation of 30% mismatch at onshore AC gird equivalent impedance, the proposed de-loading NAC strategy can provide better transient performance comparing with de-loading VC strategy. From comparing (c) and (d) of Fig. 4.13, the proposed de-loading

NAC strategy can provide relatively smaller peak current and can relieve the impact on power electronics devices in systems. From comparing (e) and (f) of Fig. 4.13, the overshoots of DC voltage are also reduced via adopting the proposed de-loading NAC strategy.

(5) *System response to HVDC link with parameters variations*: Besides mismatched parameters of on shore AC grid, VC controller is more sensitive to mismatched parameters of HVDC link. The (a) and (b) of Fig. 4.15 demonstrate that the mismatched impedance of HVDC link will cause more severe oscillation when regulating DC voltage and AC currents during onshore AC grid voltage sag. Similarly, (c)-(f) of of Fig. 4.15 are used for evaluating the FRT performance under different level of mismatches of reactance and resistance. Unlike mismatches of parameters in AC grids which mismatches of resistance and reactance play equally important roles on FRT performance, the mismatches of resistance play relatively severe impact on DC link comparing the mismatches of reactance. From (c) and (d) of Fig. 4.15, the peak AC current is suppressed and maintained into a relatively small range via adopting the proposed de-loading NAC strategy. From (e) and (f) of Fig. 4.15, although the overshoots of DC voltage varied obviously with fluctuation of resistance and the peak value increases linearly with the equivalent resistance value, the proposed de-loading NAC strategy still suppresses the DC voltage effectively comparing with conventional de-loading strategy.

(6) *System response for evaluating the de-loading strategy with different droop gains*: For evaluating the FRT performance of adopting proposed de-loading strategy with different droop gains, different droop gain K_{d} is adopted in de-loading control strategies. K_{d} is selected from 0.2 to 0.4 and then the system response of different droop gains is illustrated in Fig.4.17. From comparing the simulation results with different droop gains, for both VC and NAC, larger droop gains can suppress AC currents and DC voltage overshoots more effectively. However, besides the FRT performance there is control performance need to be considered. To compare the control performance of each schemes in difference droop gains, the overall control costs is calculated and provided in Table 4.3. Here control cost of SEC controller $\int_0^T(|u_{\mathrm{secd}}-u_{\mathrm{secdini}}|+|u_{\mathrm{secd}}-u_{\mathrm{secdini}}|)\mathrm{d}t$, where u_{ini} is the initial value which being set

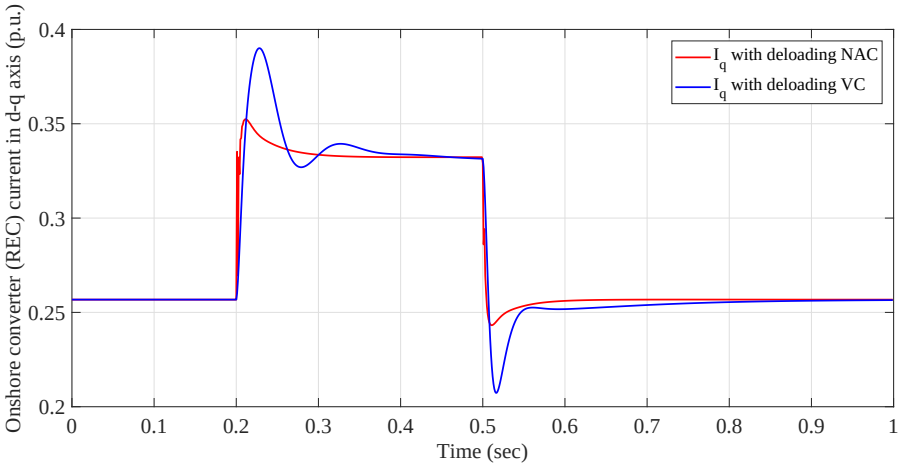

(a)

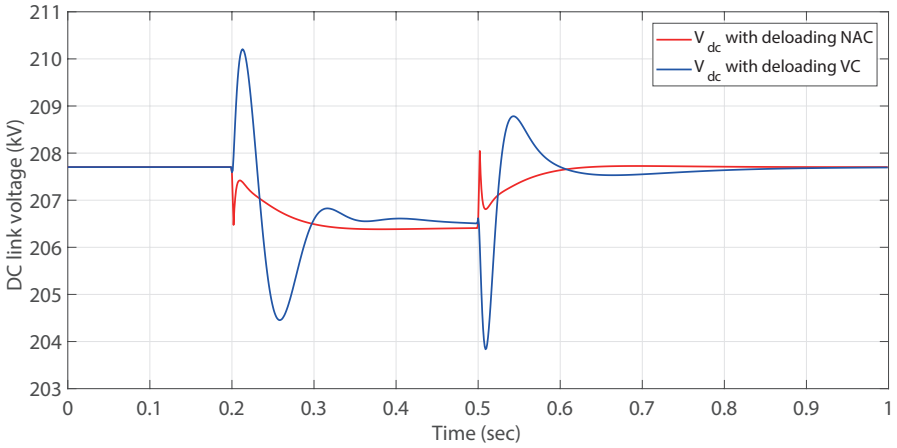

(b)

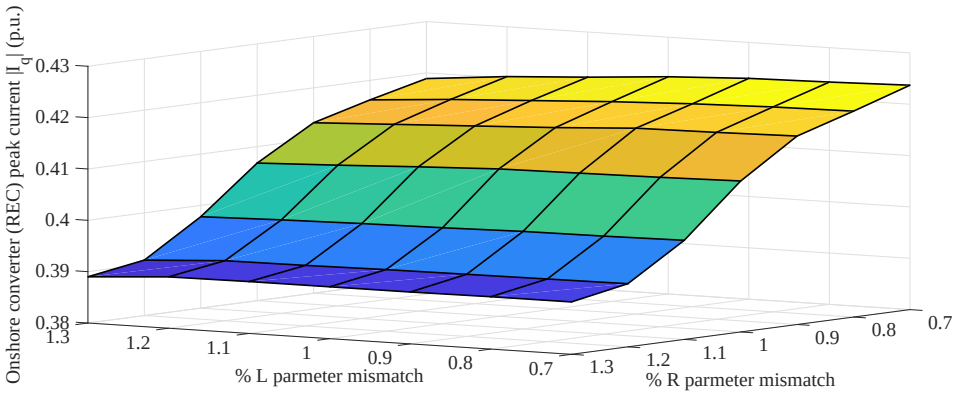

(c)

Figure 4.12: System responses obtained with 0.3s duration of 30% voltage sag at onshore AC grid with grid parameter uncertainties-1.

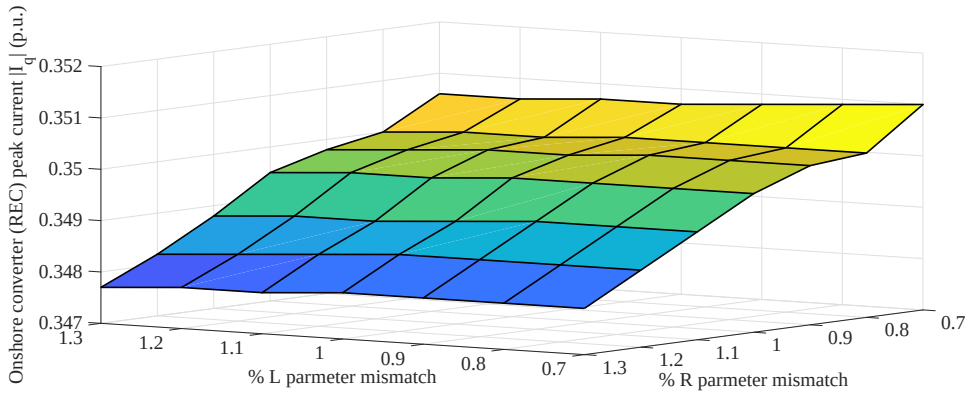

(a)

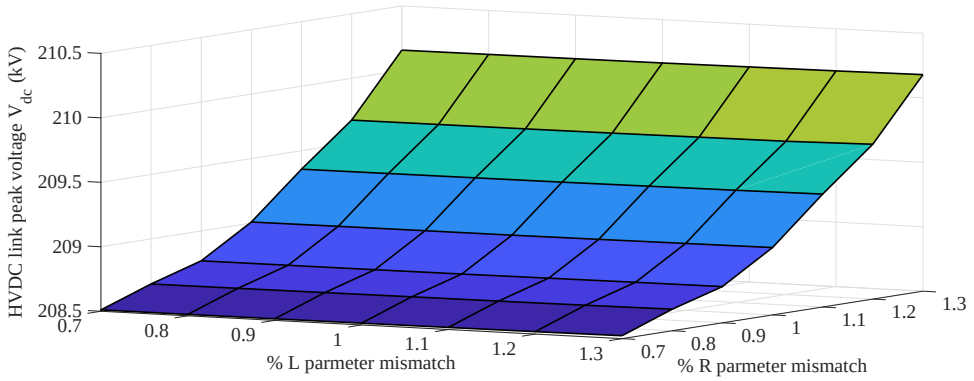

(b)

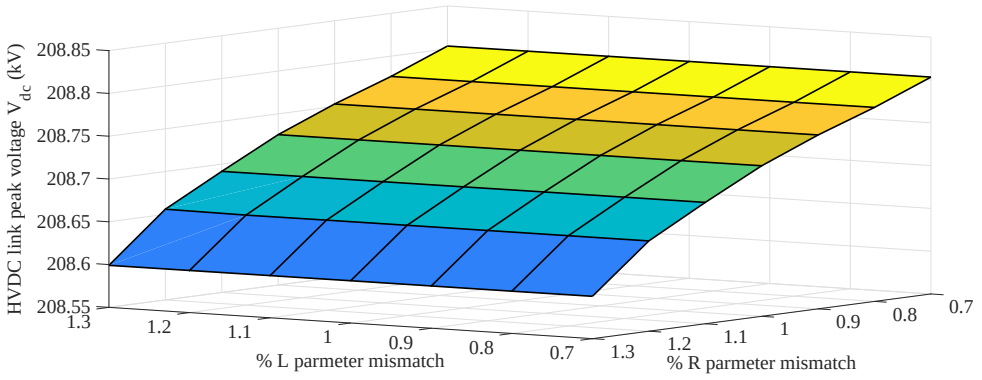

(c)

Figure 4.13: System responses obtained with 0.3s duration of 30% voltage sag at onshore AC grid with grid parameter uncertainties-2.

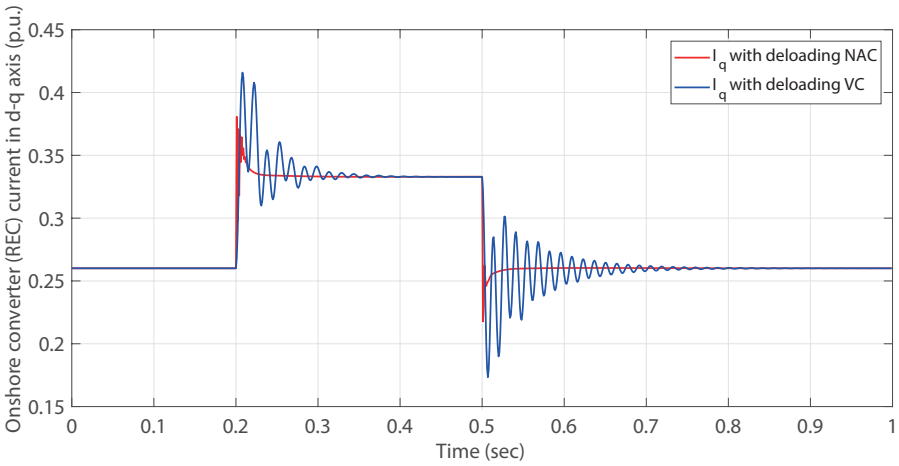

(a)

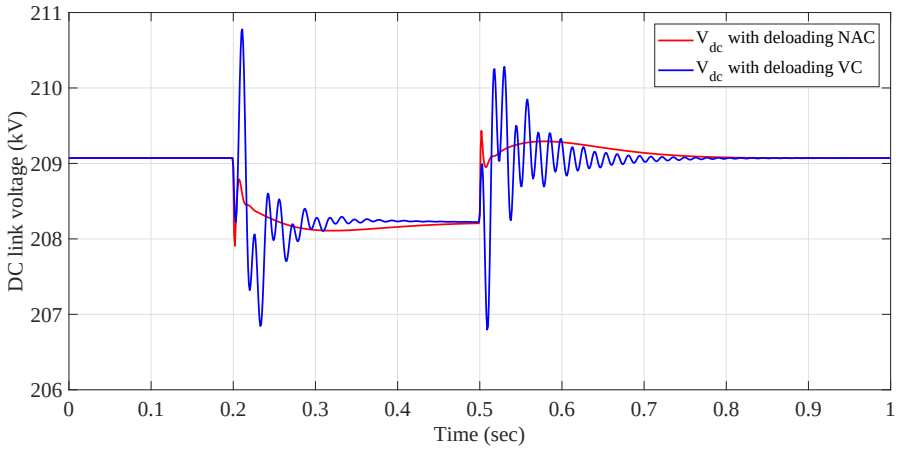

(b)

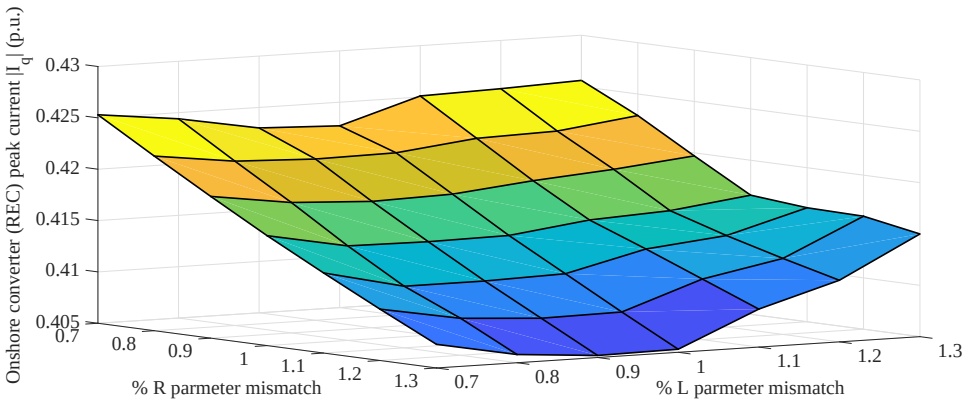

(c)

Figure 4.14: System responses obtained with 0.3s duration of 30% voltage sag at onshore AC grid with DC link parameter uncertainties-1.

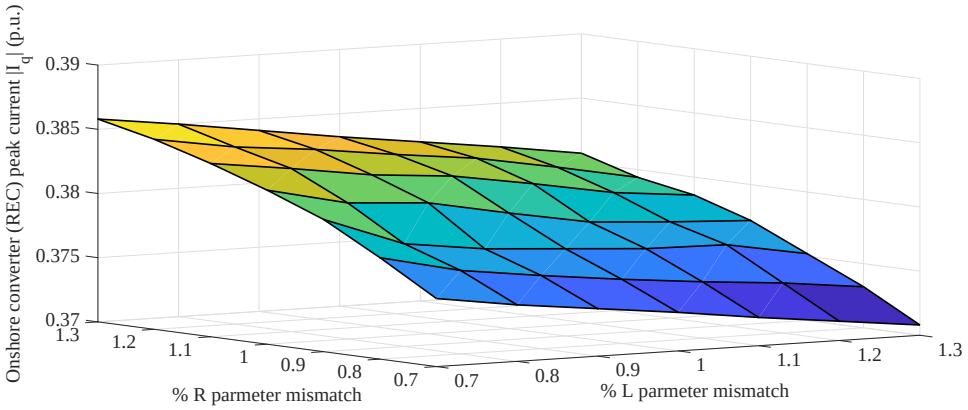

(a)

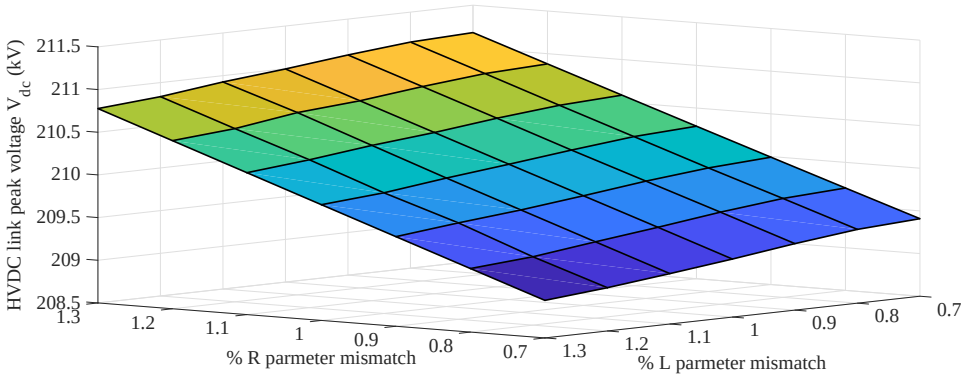

(b)

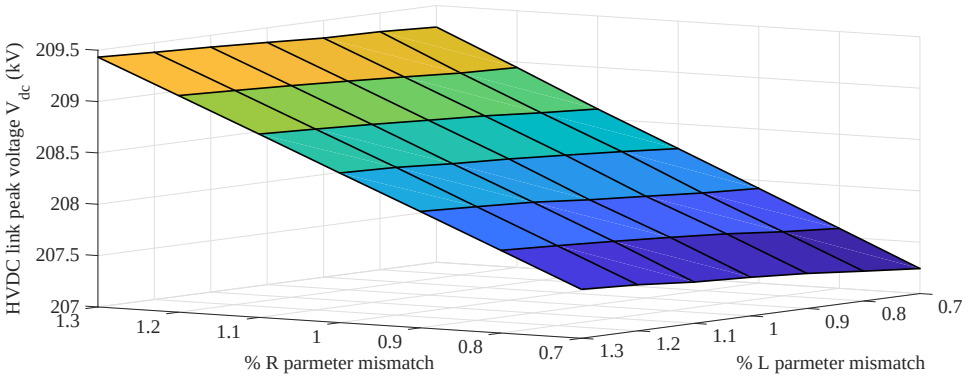

(c)

Figure 4.15: System responses obtained with 0.3s duration of 30% voltage sag at onshore AC grid with DC link parameter uncertainties-2.

Table 4.3: Overall control costs of different control schemes with varying de-loading droop gain

Droop gain K_{d}	0.2	0.25	0.3	0.35	0.4
Deloading VC	0.00965	0.01165	0.01365	0.01701	0.0197
Deloading NAC	0.00969	0.01177	0.01385	0.01733	0.02008

in advance. The units of system variables are p.u.. The simulation time $T = 6$ s such that all system states can converge to the equilibrium point after AC grid voltage sag. Note that under the nominal model, NAC has a little bit higher IAE than VC due to the estimation error, which the difference is only 0.414%, 1.02%, 1.46%, 1.89% and 1.93% of the de-loading VC. For evaluating the different droop gains, it can be found that increasing the droop gains although enhances the FRT performance and also increases the control costs. In order to get satisfied FRT performance and also maintain the acceptable control efforts, 0.3 is chosen for proposed control strategy.

4.5 Hardware-in-the-loop Test

4.5.1 Experimental platform

In order to validate the implementation feasibility of the proposed controller, a HIL test is carried out based on dSPACE simulator. The experimental platform is illustrated by Fig. 4.18. The configuration of the HIL test platform arrangement is illustrated by Fig. 4.19. For the HIL test, since the pulse width modulation (PWM) and IGBT switching processes are added into system emulation machine and however the controller is still designed for system-level, the gate signal sampling time step is significantly smaller than the system-level time step [129] and there is sampling time resolution difference. Besides sampling time difference, processes of PWM and IGBT switching bring extra dynamics to the system modelling which is regarded as unmodelled dynamics to the model which is used for controller designing process mentioned in section II, hence the HIL test can also validate the effectiveness of proposed FRT strategy in the presence of unmodelled dynamics. As demonstrated in Fig. 4.19, the proposed SEC and REC controllers are embed-

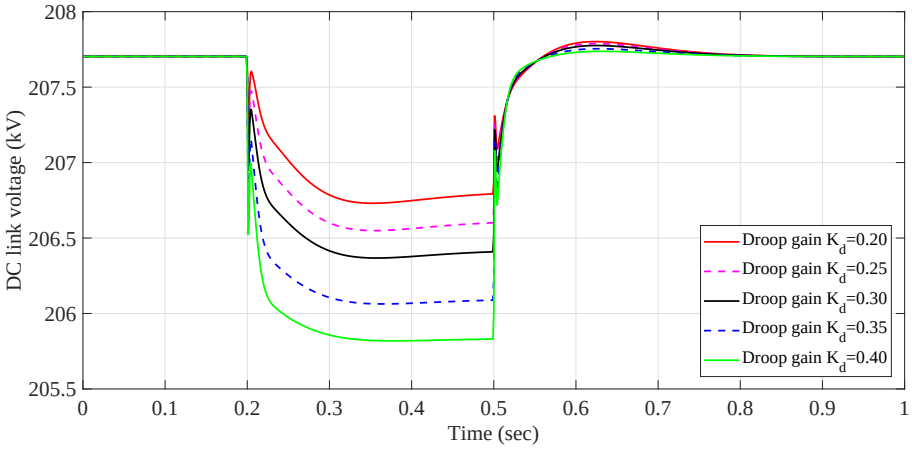

(a)

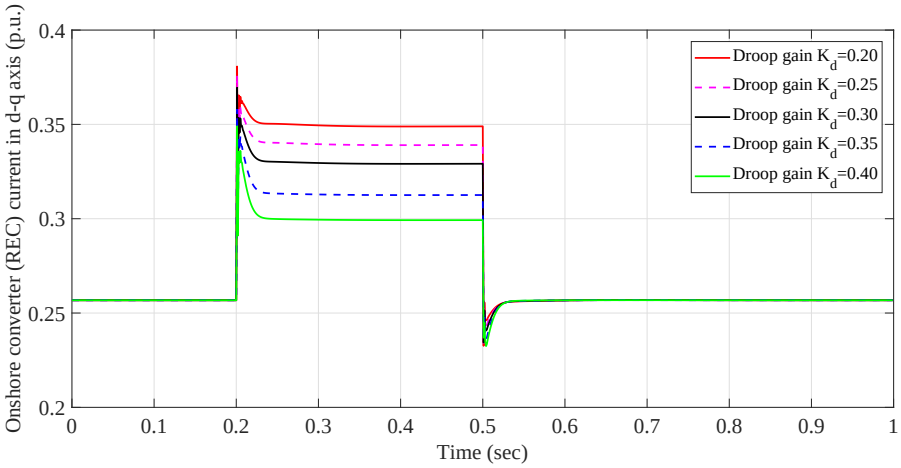

(b)

Figure 4.16: System responses obtained with 0.3s duration of voltage sag with different de-loading droop gains-1.

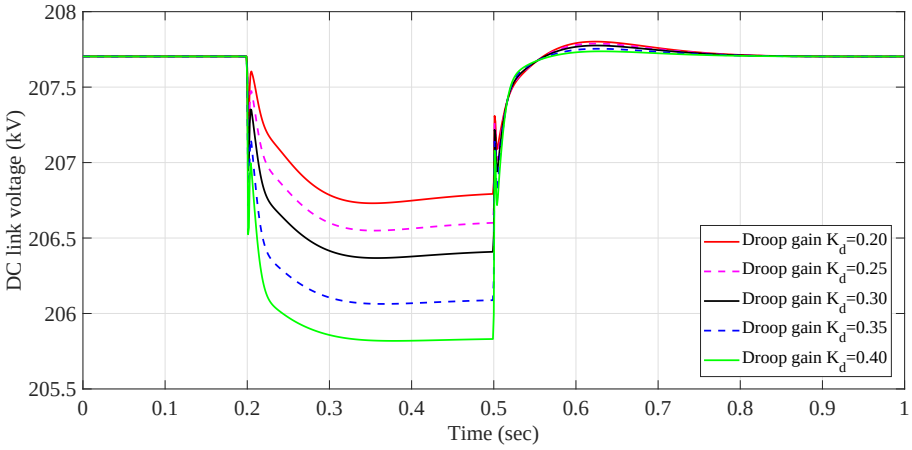

(a)

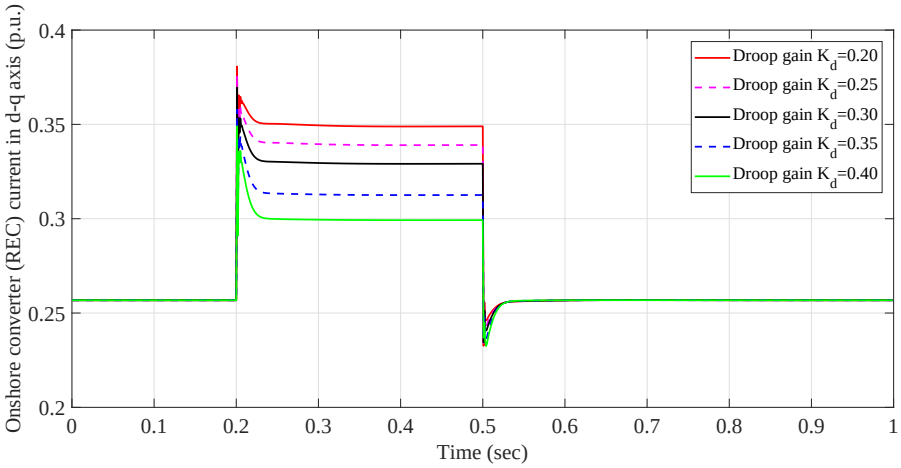

(b)

Figure 4.17: System responses obtained with 0.3s duration of voltage sag with different de-loading droop gains-2.

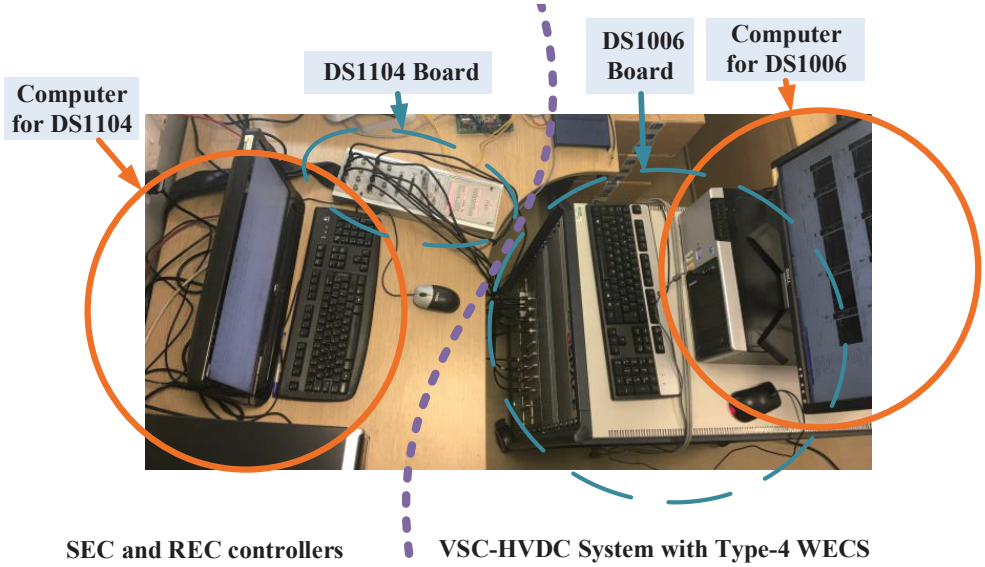

Figure 4.18: The HIL test platform based on the dSPACE simulator.

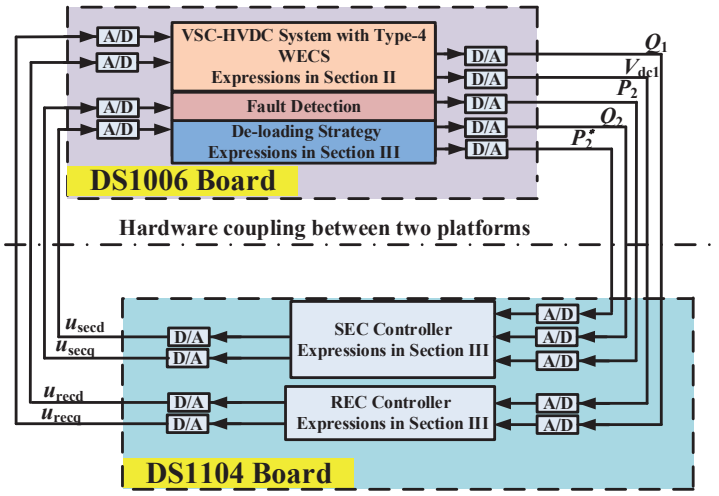

Figure 4.19: The block diagram for HIL test.

ded into on one DSP board (dSPACEDS1104) with a sampling frequency $f_1 = 0.5$ kHz, Meanwhile the VSC-HVDC system with type-4 WECS which includes fault detection and de-loading strategy are simulated on another dSPACE platform (DS1006 board) with the limit sampling frequency $f_2 = 50$kHz to make the emulating system with detailed model as close to the real plant as possible. The necessary measurements obtained from DS1006 platform is sent to SEC and REC controller on another DSP board (dSPACEDS1104) for calculating required converter voltage and sent back to DS1006 for corresponding converter PWM process via coaxial cable with Bayonet Neill-Concelman (BNC) connector. Since the communication link is not very long as shown in Fig. 4.18, the communication delay is just few clock cycles at most and can be normally regelated. However there is sampling frequency difference between the controller and system emulator, so that the communication process will still generates noises to the whole system and will cause fluctuation to final FRT performance.

4.5.2 FRT performance during voltage sags

To verifying the effectiveness of the proposed FRT strategy, voltage sags with different reduced voltage level is simulated at the onshore main AC grid in the DS1006 board. The HIL test result is shown in the Fig. 4.20. The test is taken at 1s, 3s and 5s with 30%, 50% and 70% voltage sags. DC voltage is recorded as an example for their explicit original curves and being compared with the system response obtained from simulation. From the comparison shown in the Fig. 4.20, the system response obtained from HIL test has almost same performance as that of the simulation test besides some inevitable fluctuations mentioned above. Therefore The effectiveness of proposed de-loading NAC strategy is verified.

4.6 Conclusion

In this chapter, a novel NAC based REC controller and SEC controller have been developed for VSC-HVDC transmission systems with wind farm integrated, which can provide significant robustness against system uncertainties and rapid response

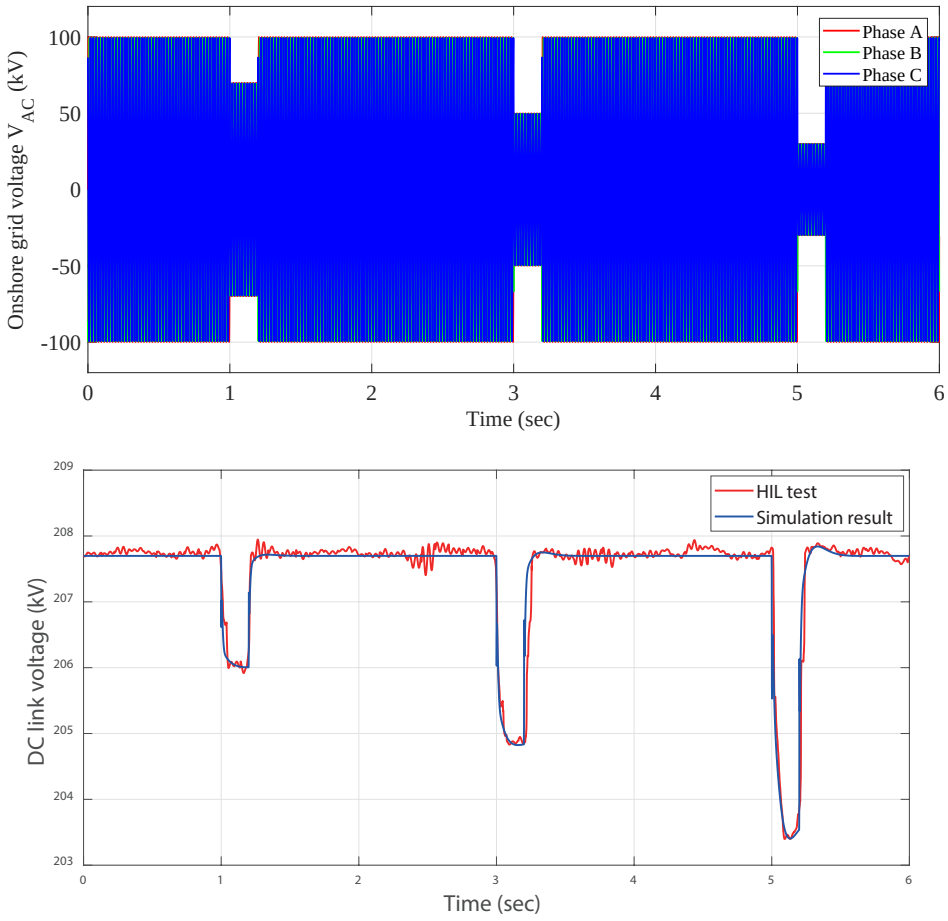

Figure 4.20: System responses obtained from the HIL test for comparison with simulation results.

to the de-loading process for enhancing the FRT capability. The proposed FRT strategy effectively suppresses peak AC current surge and DC voltage rise during AC mainland grid fault and hence preventing serious mechanical stress to the power electronic devices. The proposed NAC adopts HGPOs and HGSPOs to obtain estimates of the system states and perturbation terms. Therefore it can compensate the perturbation in real-time and provide optimal performance over whole system operation range and control performance will not degrade for the system nonlinearity during severe faults. Simulation results verify that the effectiveness of proposed FRT strategy of enhancing the FRT capability, especially in the presence of system parameter uncertainties. Then the proposed controller is embedded into the dSPACE simulator for HIL test, results validate its implementation feasibility.

As presented in this chapter, the NAC based control strategy is applied to the VSC-HVDC system with offshore wind farm integration for whole system fault ride through capability enhancement. In the next chapter, the control strategy which is applied to multi-terminal VSC-HVDC system with offshore wind farm integration will be modified.

Chapter 5

Perturbation Observer based Robust Passivity-based Control for VSC-MTDC Systems

5.1 Introduction

Large-scale integration of offshore wind power to the main grid presents a number of technical, economical, and environmental challenges [130]. With the capacity and distance of offshore wind farm increases, conventional AC transmission system displays serious drawbacks, e.g., long AC cables usually produce significant amount of capacitive current which often limits the transmission capacity and requires extra reactive power compensation. Besides, AC connections require to be operated synchronously between the wind farm and the power grid. Therefore, all faults occur in either grid are propagated in the other [131].

Currently, line-commutated converter (LCC) based HVDC (LCC-HVDC) is regarded as a mature technology on overhead lines and an economical solution with higher power ratings. Conventional LCC-HVDC transmission using line-commutated thyristor valves has higher power rating and is capable of very high transmission voltage. It is also characterized by higher transmission efficiency. However, for connecting offshore wind farms, its disadvantages are obvious: coarser reactive power

control and cannot control the active power and reactive power independently, requiring strong AC power source to maintain operation and own black-start capability, requiring AC&DC harmonic filter to eliminate generated harmonic distortion. Moreover, extra auxiliary equipments like filter and power source comparing with VSC cannot meet the space requirements of offshore substation application. Therefore, there is no LCC-HVDC offshore substation in operation. In contrast, voltage source converter based high voltage direct current (VSC-HVDC) technology using pulse-width modulation (PWM) with lower harmonic distortion of AC-side voltage, as well as fewer auxiliary filters, attracts noticeable attention around the globe. It is more suitable for offshore wind farm connection, in which active and reactive power can be independently controlled and VSCs are able to operate in weak or even passive networks [72]. In the Nanao project [132] which is the world's first multi-terminal VSC-HVDC transmission project in operation. The project is designed with ratings of $\pm$ 160kV/200MW-100MW-50MW to transmit dispersed, intermittent wind power generated on Nanao island into the mainland. A crucial task of VSC-HVDC system is how to design proper control schemes to achieve satisfactory system performance.

In general, linear control methods using proportional-integral (PI) loops are widely adopted for VSC-HVDC systems. However, the VSC-HVDC systems with wind farm connection are highly nonlinear resulted from converters, wind turbine aerodynamics, highly stochastic wind speed, and power grids with various system uncertainties like power angle and uncertain output impedance. Hence, their control performance may be dramatically degraded as its control parameters are determined from one-point linearization model [76]. In order to tackle this thorny problem, robust controller for VSC-HVDC systems is required to ensure a consistent control performance under various system uncertainties, such as adaptive backstepping [79] and robust sliding-mode control [88], which have been developed to greatly improve system robustness via estimation compensation of unknown constant or slow-varying system parameters. However, the parameter estimates via these estimation functions may drift in the presence of measurement noise and greatly increase the energy consumption.

Furthermore, the above applications are merely applied to two-terminal VSC-HVDC systems. In the multi-terminal VSC-HVDC (VSC-MTDC) system framework, not only the DC voltage and power transmission stability need to be self-controlled, but also an appropriate coordination among different terminals are needed. Thus far, several coordinated control schemes have been developed for VSC-MTDC systems, such as adaptive droop control [58], which can share the burden according to the available headroom of each converter station. Meanwhile, an adaptive backstepping droop controller is proposed in [59], which can adaptively tune the droop gains to enhance control performance of traditional droop controllers by considering DC cable dynamics. Moreover, power-dependent droop-based control strategy is proposed in [60] so as to offer enhanced dynamic responses during AC/DC faults and large power scheduling changes.

Generally speaking, the aforementioned approaches merely consider the control problems as a pure mathematical issue, while the physical/engineering background of the given object is somehow ignored. In order to enable the power sharing among each controlled converter of the MTDC system at the same time without communications, advanced control is required. The passivity-based control (PC) offers a powerful tool to beneficially exploit the physical property of a given engineering problem, upon energy interconnection and assignment, to achieve a satisfactory transient response with relatively low control efforts [61]. Because of relatively low control efforts, PC is very attractive when operating the MTDC with offshore wind farm integration. Relatively high-frequency reactive and active power regulation in MTDC with offshore wind farm integration strengthen the advantage of PC. However, conventional PC [133] is highly sensitive to the uncertain system parameters and requires a detailed system model. To handle such issue, a perturbation observer based robust passivity-based control (PORPC) scheme is proposed for an N-terminal VSC-MTDC system, in which the combinatorial effect of interaction between different terminals, unmodelled dynamics and unknown time-varying external disturbances is aggregated into a perturbation, which is estimated online by a high-gain state and perturbation observer (HGSPO) [121, 63] and can be represented as a chained-integrator system associated with matched nonlinearities and

disturbances. Moreover, PORPC does not require an accurate VSC-MTDC model and only the DC voltage, active and reactive power need to be measured. Furthermore, it provides a faster transient response with low control efforts as passification [133] is adopted to carefully reshape the system damping.

The main novelties and contributions of this chapter can be summarized as follows:

• The active/reactive power control can achieve reliable and robust decoupling control with fast responses in randomly time-varying wind power outputs and severe grid faults;

• Compared to reference [63], there are three improvements listed as follows, (1) a DC link voltage droop controller with appropriate droop constant is introduced into PORPC of each terminal, which can provide immediate response to the grid unbalanced conditions, (2) The wind farm modelling is considered during the controller design process, in which the controller parameters are modified during this case, (3) The implementation feasibility of PORPC is validated through several case studies on Simulink and real-time hardware in-loop (HIL) test based on dSPACE platform;

• The DC voltage regulation control aims to rapidly compensate various DC cable modelling uncertainties, such as unpredictable power losses, inaccurate series resistance and inductance, and external disturbances resulted from randomly time-varying wind speed conditions;

5.2 N-terminal VSC-MTDC System with Offshore Wind Farm Modelling

As same as the previous chapters, the mathematical model of investigated N-terminal VSC-MTDC system which is illustrated in this sections is established under the synchronous *dq* frame. Lumped parameter model of the AC system is considered in this modelling section. The AC network is represented via series connection of

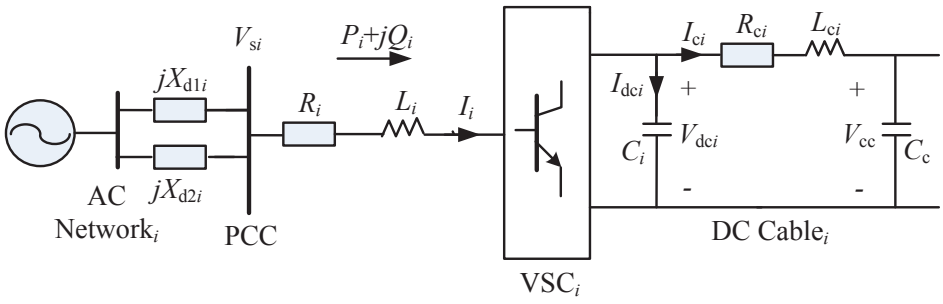

Figure 5.1: One terminal in an N-terminal VSC-MTDC system.

AC power systems and transmission lines. The corresponding AC system which is interfaced to a VSC at the point of common coupling (PCC) through the transformer. VSCs in N-terminal VSC-MTDC system are represented by averaged model during modeling the N-terminal VSC-MTDC system in this section. As mentioned, since the synchronous *dq* frame is adopted in the modelling part, the *dq* frame is placed on corresponding AC system terminals firstly. The same PLL used in Chapter 4 is applied for the transformation from the *abc* frame to the *dq* frame. During the transformation the d-axis is locked with the voltage $V_{\mathrm{s}i}$ for decoupled control in the VSCs. As same as the model mentioned previously, the AC system is assumed as balanced, i.e., the three phases are identical while each phase shifts 120° between themselves.

Take one terminal of an N-terminal VSC-MTDC system as an example which is illustrated in Fig. 5.1. On AC side of the VSC, the system dynamics can be expressed at the angular frequency ω_i as [58]

$$\begin{cases} \dot{I}_{\mathrm{d}i} = -\frac{R_i}{L_i} I_{\mathrm{d}i} + \omega_i I_{\mathrm{q}i} + \frac{V_{\mathrm{sq}i}}{L_i} + \frac{u_{\mathrm{d}i}}{L_i} \\ \dot{I}_{\mathrm{q}i} = -\frac{R_i}{L_i} I_{\mathrm{q}i} + \omega_i I_{\mathrm{d}i} + \frac{V_{\mathrm{sd}i}}{L_i} + \frac{u_{\mathrm{q}i}}{L_i} \end{cases} \tag{5.2.1}$$

where $I_{\mathrm{d}i}$ and $I_{\mathrm{q}i}$ are the *i*th d-axis and q-axis AC current; $V_{\mathrm{sd}i}$ and $V_{\mathrm{sq}i}$ are the *i*th d-axis and q-axis AC voltage, in the synchronous frame $V_{\mathrm{sd}i} = 0$ and $V_{\mathrm{sq}i} = V_{\mathrm{s}}$; $u_{\mathrm{d}i}$ and $u_{\mathrm{q}i}$ are the *i*th d-axis and q-axis control inputs; R_i and L_i are the *i*th resistance and inductance of the VSC transformer and phase reactor.

Since the resistance of the VSC reactor and switching losses (around 2% of the whole power ratings) are not considered, the active power P_i and reactive power Q_i

on the *i*th VSC can be expressed as follows [58]

$$\begin{cases} P_i = \frac{3}{2}(V_{\mathrm{sq}i}I_{\mathrm{q}i} + V_{\mathrm{sd}i}I_{\mathrm{d}i}) = \frac{3}{2}V_{\mathrm{sq}i}I_{\mathrm{q}i} \\ Q_i = \frac{3}{2}(V_{\mathrm{sq}i}I_{\mathrm{d}i} - V_{\mathrm{sd}i}I_{\mathrm{q}i}) = \frac{3}{2}V_{\mathrm{sq}i}I_{\mathrm{d}i} \end{cases} \tag{5.2.2}$$

Corresponding DC cable dynamics are expressed by [58]

$$\begin{cases} \dot{V}_{\mathrm{dc}i} = \frac{1}{V_{\mathrm{dc}i}C_i}P_i - \frac{1}{C_i}I_{\mathrm{c}i} \\ \dot{I}_{\mathrm{c}i} = \frac{1}{L_{\mathrm{c}i}}V_{\mathrm{dc}i} - \frac{R_{\mathrm{c}i}}{L_{\mathrm{c}i}}I_{\mathrm{c}i} - \frac{1}{L_{\mathrm{c}i}}V_{\mathrm{cc}} \end{cases} \tag{5.2.3}$$

where C_i and C_{c} are the *i*th and common DC capacitance which voltages are denoted by $V_{\mathrm{dc}i}$ and V_{cc}, respectively; $R_{\mathrm{c}i}$ and $L_{\mathrm{c}i}$ are the resistance and inductance of the *i*th DC cable; and $I_{\mathrm{c}i}$ is the current flowing through the *i*th DC cable.

The dynamics of the common DC capacitor can be expressed according to the Kirchhoff's current law and shown below

$$\dot{V}_{\mathrm{cc}} = \frac{1}{C_{\mathrm{c}}}\sum_{i=1}^{N} I_{\mathrm{c}i} \tag{5.2.4}$$

The global model of the N-terminal VSC-MTDC system is summarized as follows

$$\begin{cases} \dot{I}_{\mathrm{d}i} = -\frac{R_i}{L_i}I_{\mathrm{d}i} + \omega_i I_{\mathrm{q}i} + \frac{V_{\mathrm{sq}i}}{L_i} + \frac{u_{\mathrm{d}i}}{L_i} \\ \dot{I}_{\mathrm{q}i} = -\frac{R_i}{L_i}I_{\mathrm{q}i} + \omega_i I_{\mathrm{d}i} + \frac{u_{\mathrm{q}i}}{L_i} \\ \dot{V}_{\mathrm{dc}i} = \frac{3V_{\mathrm{sq}i}I_{\mathrm{q}i}}{2V_{\mathrm{dc}i}C_i} - \frac{1}{C_i}I_{\mathrm{c}i} \\ \dot{I}_{\mathrm{c}i} = \frac{1}{L_{\mathrm{c}i}}V_{\mathrm{dc}i} - \frac{R_{\mathrm{c}i}}{L_{\mathrm{c}i}}I_{\mathrm{c}i} - \frac{1}{L_{\mathrm{c}i}}V_{\mathrm{cc}} \\ \dot{V}_{\mathrm{cc}} = \frac{1}{C_{\mathrm{c}}}\sum_{i=1}^{N} I_{\mathrm{c}i} \end{cases} \quad , i = 1, \ldots, N \tag{5.2.5}$$

Besides normal grid models which are usually considered as fixed power sources that connect to the VSC-MTDC model, the grid with high wind power penetration (20%) is considered as well. The offshore wind farm simulated in this chapter adopts an aggregated model such that a lumped wind turbine is used to represent the whole wind farm [134]. In particular, the wind turbine dynamics is represented by a two-mass model while the blade pitch angle is assumed to be a constant. According to wind turbine aerodynamics, the mechanical power P_{m} extracted from wind is described as follows [136, 135]

$$P_{\mathrm{m}} = \frac{1}{2}\rho A_{\mathrm{r}} c_{\mathrm{p}}(\lambda, \theta) v_{\omega}^3 \tag{5.2.6}$$

where P_{m} is the power extracted from the wind; ρ is air density; A_{r} is the area covered by the rotor; v_ω is the wind speed; and c_{p} is the power coefficient; θ is the pitch angle of rotor blades; λ is the tip speed ratio which $\lambda = \frac{v_{\mathrm{t}}}{v_\omega}$ with v_{t} is blade tip speed [137, 138]. Here c_{p} can be described by

$$c_{\mathrm{p}}(\lambda,\theta) = 0.73(\frac{151}{\lambda_i} - 0.58\theta - 0.002\theta^{2.14} - 13.2)e^{-18.4/\lambda_i} \tag{5.2.7}$$

where

$$\lambda_i = \frac{1}{\frac{1}{\lambda - 0.02\theta} - \frac{0.003}{\theta^3+1}} \tag{5.2.8}$$

5.3 PORPC Design for N-terminal VSC-MTDC System

5.3.1 Rectifier Controller Design

Denote the first VSC as the rectifier such that DC voltage V_{dc1} and reactive power Q_1 can be regulated to their references V^*_{dc1} and Q^*_1, respectively. Define the tracking error

$\mathbf{e}_1 = [e_{11}, e_{12}]^{\mathrm{T}} = [V_{\mathrm{dc1}} - V^*_{\mathrm{dc1}}, Q_1 - Q^*_1]^{\mathrm{T}}$,

Differentiate $\mathbf{e}_1$ until control inputs u_{q1} and u_{d1} appear explicitly, gives

$$\begin{cases} \ddot{e}_{11} & = \frac{3V_{\mathrm{sq1}}}{2C_1V_{\mathrm{dc1}}}\Big[- \frac{R_1}{L_1}I_{\mathrm{q1}} + \omega_1 I_{\mathrm{d1}} \\ & \quad - \frac{I_{\mathrm{q1}}}{C_jV_{\mathrm{dc1}}}\Big(\frac{3V_{\mathrm{sq1}}I_{\mathrm{q1}}}{2V_{\mathrm{dc1}}} - I_{\mathrm{c1}}\Big)\Big] + \frac{3V_{\mathrm{sq1}}}{2C_1L_1V_{\mathrm{dc1}}}u_{\mathrm{q1}} \\ & \quad - \frac{1}{C_1L_{\mathrm{c1}}}(V_{\mathrm{dc1}} - R_{\mathrm{c1}}I_{\mathrm{c1}} - V_{\mathrm{cc}}) - \ddot{V}^*_{\mathrm{dc1}} \\ \dot{e}_{12} & = \frac{3V_{\mathrm{sq1}}}{2}\Big(-\frac{R_1}{L_1}I_{\mathrm{d1}} + \omega_1 I_{\mathrm{q1}} + \frac{V_{\mathrm{sq1}}}{L_1}\Big) + \frac{3V_{\mathrm{sq1}}}{2L_1}u_{\mathrm{d1}} - \dot{Q}^*_1 \end{cases} \tag{5.3.1}$$

It can be seen that system (5.3.1) includes two decoupled SISO subsystems, in which V_{dc1} is controlled by u_{q1} and Q_1 is controlled by u_{d1}, respectively.

The perturbations of system (5.3.1) are defined as

$$\begin{aligned}\Psi_{11}(\cdot) = &\frac{3V_{\mathrm{sq1}}}{2C_1V_{\mathrm{dc1}}}\Big[-\frac{R_1}{L_1}I_{\mathrm{q1}}+\omega_1 I_{\mathrm{d1}}\\ &-\frac{I_{\mathrm{q1}}}{C_1V_{\mathrm{dc1}}}\Big(\frac{3V_{\mathrm{sq1}}I_{\mathrm{q1}}}{2V_{\mathrm{dc1}}}I_{\mathrm{c1}}\Big)\Big]\\ &-\frac{1}{C_1L_{\mathrm{c1}}}(V_{\mathrm{dc1}}-R_{\mathrm{c1}}I_{\mathrm{c1}}-V_{\mathrm{cc}})\\ &+(\frac{3V_{\mathrm{sq1}}}{2C_1L_1V_{\mathrm{dc1}}}-b_{11})u_{\mathrm{q1}} \qquad (5.3.2)\\ \Psi_{12}(\cdot) = &\frac{3V_{\mathrm{sq1}}}{2}\left(-\frac{R_1}{L_1}I_{\mathrm{d1}}+\omega_1 I_{\mathrm{q1}}+\frac{V_{\mathrm{sq1}}}{L_1}\right)\\ &+(\frac{3V_{\mathrm{sq1}}}{2L_1}-b_{12})u_{\mathrm{d1}} \qquad (5.3.3)\end{aligned}$$

And system (5.3.1) can be expressed by

$$\begin{cases}\ddot{e}_{11} = \Psi_{11}(\cdot)+b_{11}u_{\mathrm{q1}}-\ddot{V}^*_{\mathrm{dc1}}\\ \dot{e}_{12} = \Psi_{12}(\cdot)+b_{12}u_{\mathrm{d1}}-\dot{Q}^*_1\end{cases} \qquad (5.3.4)$$

where b_{11} and b_{12} are constant control gains.

A third-order HGSPO is designed to estimate $\Psi_{11}(\cdot)$ as

$$\begin{cases}\dot{\hat{V}}_{\mathrm{dc1}} = \frac{\alpha_{11}}{\epsilon}(V_{\mathrm{dc1}}-\hat{V}_{\mathrm{dc1}})+\hat{\dot{V}}_{\mathrm{dc1}}\\ \dot{\hat{V}}_{\mathrm{dc1}} = \hat{\Psi}_{11}(\cdot)+\frac{\alpha_{12}}{\epsilon^2}(V_{\mathrm{dc1}}-\hat{V}_{\mathrm{dc1}})+b_{11}u_{\mathrm{q1}}\\ \dot{\hat{\Psi}}_{11}(\cdot) = \frac{\alpha_{13}}{\epsilon^3}(V_{\mathrm{dc1}}-\hat{V}_{\mathrm{dc1}})\end{cases} \qquad (5.3.5)$$

Then a second-order high-gain perturbation observer (HGPO) is designed to estimate $\Psi_{12}(\cdot)$ as

$$\begin{cases}\dot{\hat{Q}}_1 = \hat{\Psi}_{12}(\cdot)+\frac{\alpha'_{11}}{\epsilon}(Q_1-\hat{Q}_1)+b_{12}u_{\mathrm{d1}}\\ \dot{\hat{\Psi}}_{12}(\cdot) = \frac{\alpha'_{12}}{\epsilon^2}(Q_1-\hat{Q}_1)\end{cases} \qquad (5.3.6)$$

where α_{11}, α_{12}, α_{13}, α'_{11}, and α'_{12} are observer gains, with $0<\epsilon\ll 1$.

The PORPC for system (5.3.1) using the estimate of states and perturbations is designed as

$$\begin{cases}u_{\mathrm{q1}} &= b_{11}^{-1}[-\hat{\Psi}_{11}(\cdot)-k_{11}(\hat{V}_{\mathrm{dc1}}-V^*_{\mathrm{dc1}})\\ &\quad -k_{12}(\hat{\dot{V}}_{\mathrm{dc1}}-\dot{V}^*_{\mathrm{dc1}})+\ddot{V}^*_{\mathrm{dc1}}+\nu_{11}]\\ u_{\mathrm{d1}} &= b_{12}^{-1}(-\hat{\Psi}_{12}(\cdot)-k'_{11}(\hat{Q}_1-Q^*_1)+\dot{Q}^*_1+\nu_{12})\end{cases} \qquad (5.3.7)$$

where k_{11}, k_{12} and k'_{11} are feedback control gains and $\mathbf{V}_1 = [\nu_{11}, \nu_{12}]^{\mathrm{T}}$ is an additional system input.

Choose the output of system (5.3.1) as $\mathbf{Y}_1 = [Y_{11}, Y_{12}]^{\mathrm{T}} = [\dot{V}_{\mathrm{dc1}} - \dot{V}^*_{\mathrm{dc1}}, Q_1 - Q^*_1]^{\mathrm{T}}$. Then let $\mathbf{V}_1 = [-\lambda_{11}Y_{11}, -\lambda_{12}Y_{12}]^{\mathrm{T}}$, where λ_{11} and λ_{12} are some positive constants to inject an extra system damping into system (5.3.1). Based on the passivity theory, the closed-loop system is output strictly passive from output $\mathbf{Y}_1$ to input $\mathbf{V}_1$ [61].

Constant gains b_{11} and b_{12} must satisfy the following inequalities to guarantee the convergence of estimation error when the VSC operates within its normal region:

$$\begin{aligned} 3V_{\mathrm{sq1}}/[2C_1L_1V_{\mathrm{dc1}}(1-\theta_{11})] &\geq b_{11} \\ &\geq 3V_{\mathrm{sq1}}/[2C_1L_1V_{\mathrm{dc1}}(1+\theta_{11})] \end{aligned} \tag{5.3.8}$$

$$3V_{\mathrm{sq1}}/[2L_1(1-\theta_{12})] \geq b_{12} \geq 3V_{\mathrm{sq1}}/[2L_1(1+\theta_{12})] \tag{5.3.9}$$

where $0 < \theta_{11} < 1$ and $0 < \theta_{12} < 1$.

During the most severe disturbance, both DC voltage and reactive power reduce from their initial values to around zero within a short period of time Δ. Thus the boundary values of the estimate of states and perturbations are limited as $|\hat{V}_{\mathrm{dc1}}| \leq |V^*_{\mathrm{dc1}}|$, $|\hat{\dot{V}}_{\mathrm{dc1}}| \leq |V^*_{\mathrm{dc1}}|/\Delta$, $|\hat{\Psi}_{11}(\cdot)| \leq |V^*_{\mathrm{dc1}}|/\Delta^2$, $|\hat{Q}_1| \leq |Q^*_1|$, and $|\hat{\Psi}_{12}(\cdot)| \leq |Q^*_1|/\Delta$, respectively.

5.3.2 Inverter Controller Design

The second and third VSCs are chosen as the inverters which regulate active power P_k and reactive power Q_k to their references P^*_k and Q^*_k, respectively, where $k = 2, 3$. Define tracking error with droop controller embedded [139]

$$\mathbf{e}_k = [e_{k1}, e_{k2}]^{\mathrm{T}} = [P_k - P^*_k = R(V_{\mathrm{dc}k} - V^*_{\mathrm{dc}k}), Q_k - Q^*_k]^{\mathrm{T}},$$

where $R = \frac{P_{\mathrm{ACrated}k}}{V_{\mathrm{DCrated}k}\rho_k}$ with ρ_k denotes the droop constant,$P_{\mathrm{ACrated}k}$ is the rated power and $V_{\mathrm{DCrated}k}$ is the rated DC voltage of the kth DC terminal.

REMARKS 1. The values of the droop constant are designed according to the ratings of the converters. For a fixed droop scheme it is usual to choose $\rho_i P_{\text{ACrated}i} = \rho_j P_{\text{ACrated}j}, \forall i, j$. [58]. In this chapter, as 20% wind power is penetrated into terminal 3, the rating of terminal 3 is considered as 120% of terminal 2. Therefore, the droop constant of terminal 2 is chosen to be 85% of the terminal 3 considering power fluctuation of wind generation. After determining the stability region of MTDC system through modal analysis [58], the value droop constant of terminal 2 and terminal 3 are selected to be 0.035 and 0.0295, respectively. Since the droop constant is unequal , the ones with higher values would have dominant contribution from active power control loop. Smaller would ensure lesser deviation in DC link voltages.

Differentiate $\mathbf{e}_k$ until control inputs $u_{\mathrm{q}k}$ and $u_{\mathrm{d}k}$ appear explicitly, it yields

$$\begin{cases} \dot{e}_{k1} = \frac{3V_{\mathrm{sq}k}}{2}\left(-\frac{R_k}{L_k}I_{\mathrm{q}k} - \omega_k I_{\mathrm{d}k}\right) + \frac{3V_{\mathrm{sq}k}}{2L_k}u_{\mathrm{q}k} - \dot{P}_k^* \\ \dot{e}_{k2} = \frac{3V_{\mathrm{sq}k}}{2}\left(-\frac{R_k}{L_k}I_{\mathrm{d}k} + \omega_k I_{\mathrm{q}k} + \frac{V_{\mathrm{sq}k}}{L_k}\right) + \frac{3V_{\mathrm{sq}k}}{2L_k}u_{\mathrm{d}k} - \dot{Q}_k^* \end{cases} \tag{5.3.10}$$

It can be seen that system (5.3.10) includes two decoupled SISO subsystems, in which P_k is controlled by $u_{\mathrm{q}k}$ and Q_k is controlled by $u_{\mathrm{d}k}$, respectively.

The perturbations of system (5.3.10) are defined as

$$\Psi_{k1}(\cdot) = \frac{3V_{\mathrm{sq}k}}{2}\left(-\frac{R_k}{L_k}I_{\mathrm{q}k} - \omega_k I_{\mathrm{d}k}\right) + (\frac{3V_{\mathrm{sq}k}}{2L_k} - b_{k1})u_{\mathrm{q}k} \tag{5.3.11}$$

$$\Psi_{k2}(\cdot) = \frac{3V_{\mathrm{sq}k}}{2}\left(-\frac{R_k}{L_k}I_{\mathrm{d}k} + \omega_k I_{\mathrm{q}k} + \frac{V_{\mathrm{sq}k}}{L_k}\right) + (\frac{3V_{\mathrm{sq}k}}{2L_k} - b_{k2})u_{\mathrm{d}k} \tag{5.3.12}$$

And system (5.3.10) can be expressed by

$$\begin{cases} \dot{e}_{k1} = \Psi_{k1}(\cdot) + b_{k1}u_{\mathrm{q}k} - \dot{P}_k^* \\ \dot{e}_{k2} = \Psi_{k2}(\cdot) + b_{k2}u_{\mathrm{d}k} - \dot{Q}_k^* \end{cases} \tag{5.3.13}$$

where b_{k1} and b_{k2} are constant control gains.

A second-order HGPO is designed to estimate $\Psi_{k1}(\cdot)$ as

$$\begin{cases} \dot{\hat{P}}_k = \hat{\Psi}_{k1}(\cdot) + \frac{\alpha_{k1}}{\epsilon}(P_k - \hat{P}_k) + b_{k1}u_{\mathrm{q}k} \\ \dot{\hat{\Psi}}_{k1}(\cdot) = \frac{\alpha_{k2}}{\epsilon^2}(P_k - \hat{P}_k) \end{cases} \tag{5.3.14}$$

Similarly, a second-order HGPO is designed to estimate $\Psi_{k2}(\cdot)$ as

$$\begin{cases} \dot{\hat{Q}}_k = \hat{\Psi}_{k2}(\cdot) + \frac{\alpha'_{k1}}{\epsilon}(Q_k - \hat{Q}_k) + b_{k2}u_{\mathrm{d}k} \\ \dot{\hat{\Psi}}_{k2}(\cdot) = \frac{\alpha'_{k2}}{\epsilon^2}(Q_k - \hat{Q}_k) \end{cases} \tag{5.3.15}$$

where α_{k1}, α_{k2}, α'_{k1}, and α'_{k2} are observer gains.

The PORPC for system (5.3.10) using the estimate of states and perturbations is designed as

$$\begin{cases} u_{\mathrm{q}k} = b_{k1}^{-1}(-\hat{\Psi}_{k1}(\cdot) - k_{k1}(\hat{P}_k - P_k^*) + \dot{P}_k^* + \nu_{k1}) \\ u_{\mathrm{d}k} = b_{k2}^{-1}(-\hat{\Psi}_{k2}(\cdot) - k'_{k1}(\hat{Q}_k - Q_k^*) + \dot{Q}_k^* + \nu_{k2}) \end{cases} \tag{5.3.16}$$

where k_{k1} and k'_{k1} are feedback control gains and $\mathbf{V}_k = [\nu_{k1}, \nu_{k2}]^{\mathrm{T}}$ is an additional system input.

Choose the output of system (5.3.10) as $\mathbf{Y}_k = [Y_{k1}, Y_{k2}]^{\mathrm{T}} = [P_k - P_k^*, Q_k - Q_k^*]^{\mathrm{T}}$. Let $\mathbf{V}_k = [-\lambda_{k1}Y_{k1}, -\lambda_{k2}Y_{k2}]^{\mathrm{T}}$, where λ_{k1} and λ_{k2} are some positive constants to inject an extra system damping into system (5.3.10). And the closed-loop system is output strictly passive from output $\mathbf{Y}_k$ to input $\mathbf{V}_k$.

Similarly, constant gains b_{k1} and b_{k2} must satisfy:

$$3V_{\mathrm{sq}k}/[2L_k(1-\theta_{k1})] \geq b_{k1} \geq 3V_{\mathrm{sq}k}/[2L_k(1+\theta_{k1})]$$
$$3V_{\mathrm{sq}k}/[2L_k(1-\theta_{k2})] \geq b_{k2} \geq 3V_{\mathrm{sq}k}/[2L_k(1+\theta_{k2})]$$

where $0 < \theta_{k1} < 1$ and $0 < \theta_{k2} < 1$.

Again, the boundary values of the estimate of states and perturbations are limited by $|\hat{P}_k| \leq |P_k^*|$, $|\hat{\Psi}_{k1}(\cdot)| \leq |P_k^*|/\Delta$, $|\hat{Q}_k| \leq |Q_k^*|$, and $|\hat{\Psi}_{k2}(\cdot)| \leq |Q_k^*|/\Delta$, respectively. The overall control structure of PORPC (5.3.7) and (5.3.16) is illustrated by Fig. 5.2, Fig. 5.3 and Fig. 5.4, in which only the measurement of active power P_k and reactive power Q_k at the inverter side, as well as the DC voltage $V_{\mathrm{dc}1}$ and reactive power Q_1 at the rectifier side is needed for the controller and observer design. Note that their references are given by the power system operators to satisfy the practical transmission of electrical power or maintain power system stability through VSC-MTDC systems. Lastly, the obtained control inputs are modulated by the pulse width modulation (PWM) technique [140].

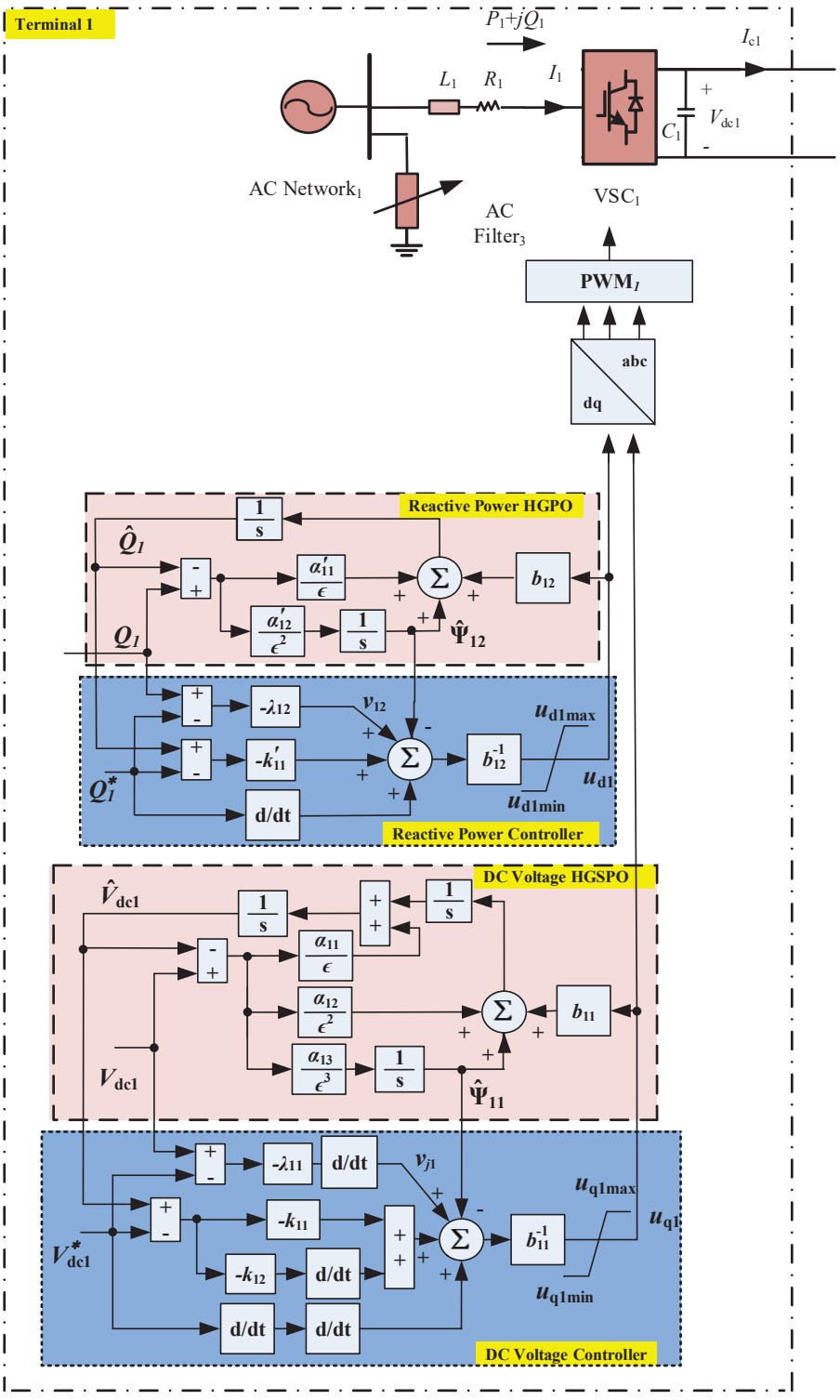

Figure 5.2: Overall control structure of PORPC for terminal one in the VSC-MTDC systems.

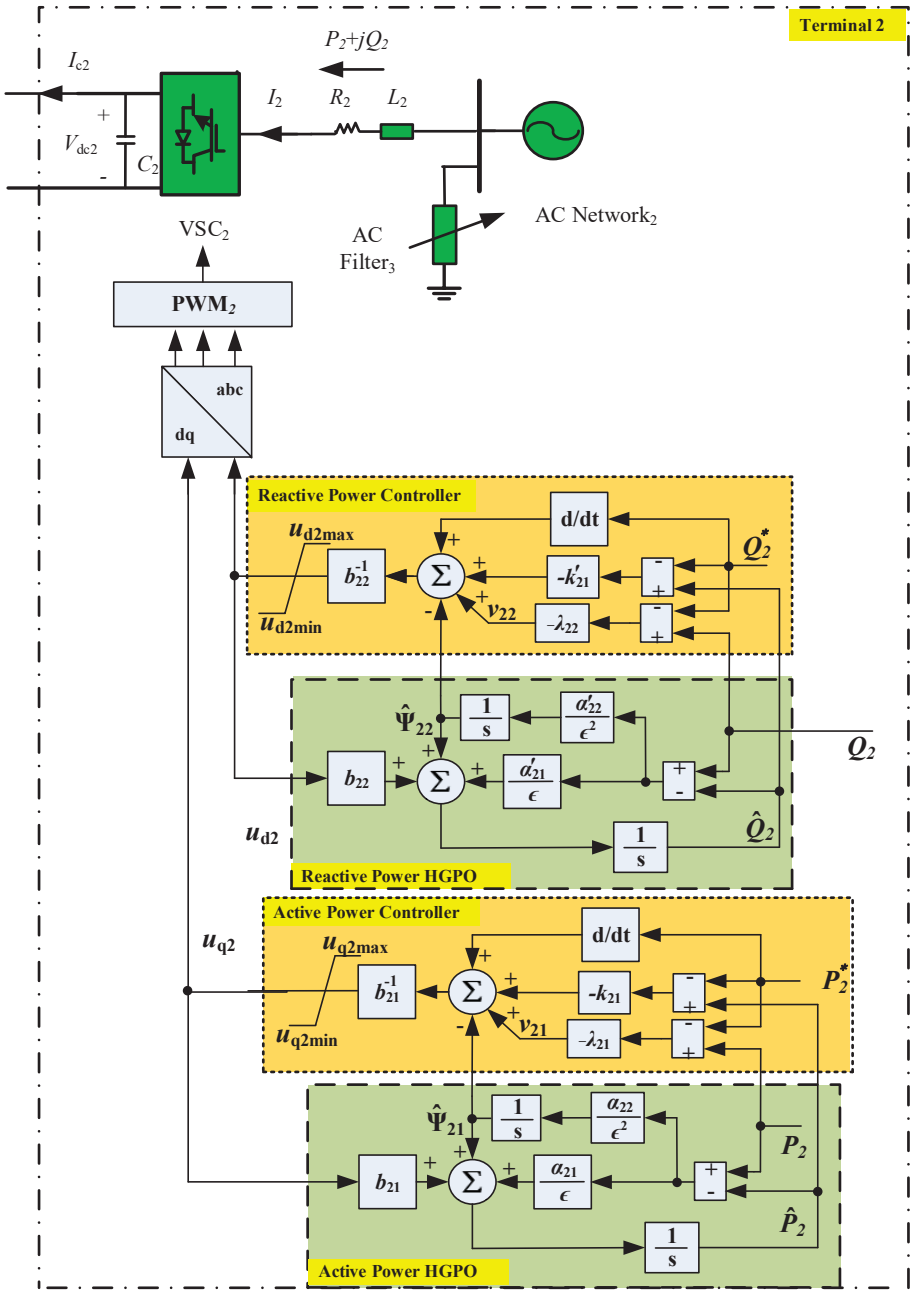

Figure 5.3: Overall control structure of PORPC for terminal two in the VSC-MTDC systems.

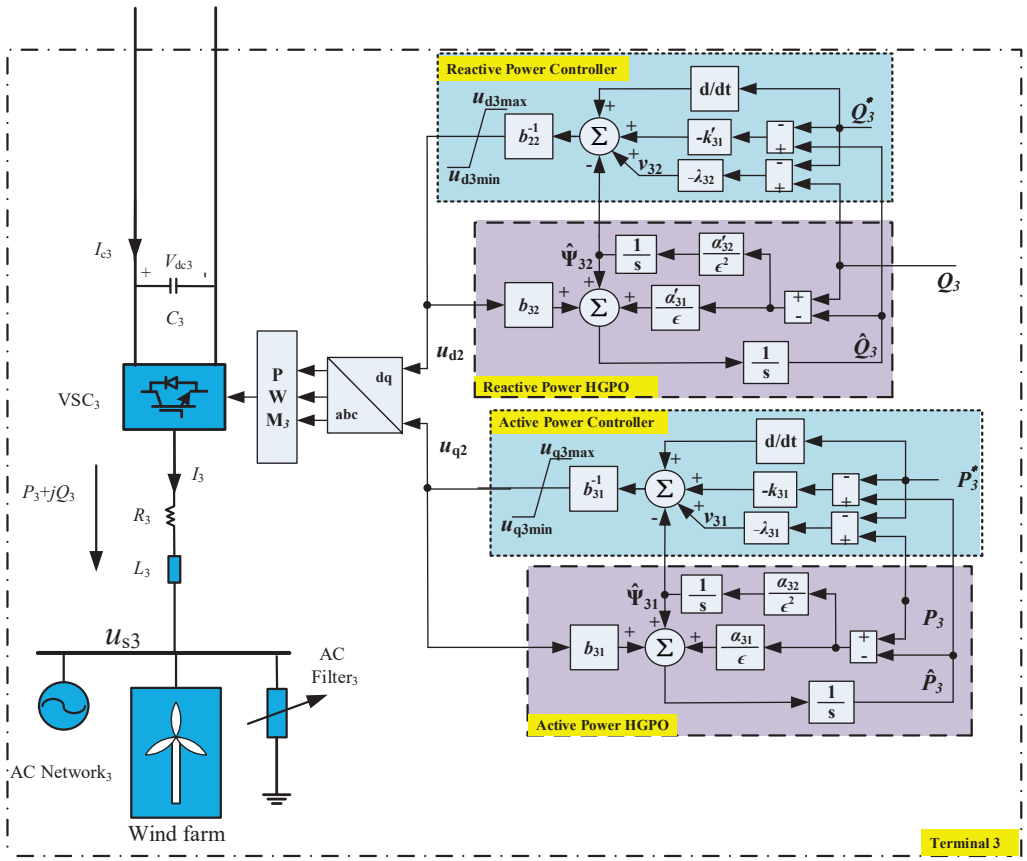

Figure 5.4: Overall control structure of PORPC for terminal three in the VSC-MTDC systems.

5.4 Case Studies

In this section, a three-terminal radial VSC-MTDC system connected to an offshore wind farm is built for simulation which is illustrated by Fig. 5.5, in which the rectifier regulates the DC voltage and reactive power of AC grid_1, while one inverter regulates the active and reactive power of the AC grid_2 and another inverter regulates the active and reactive power of the offshore wind farm with AC grid_3.

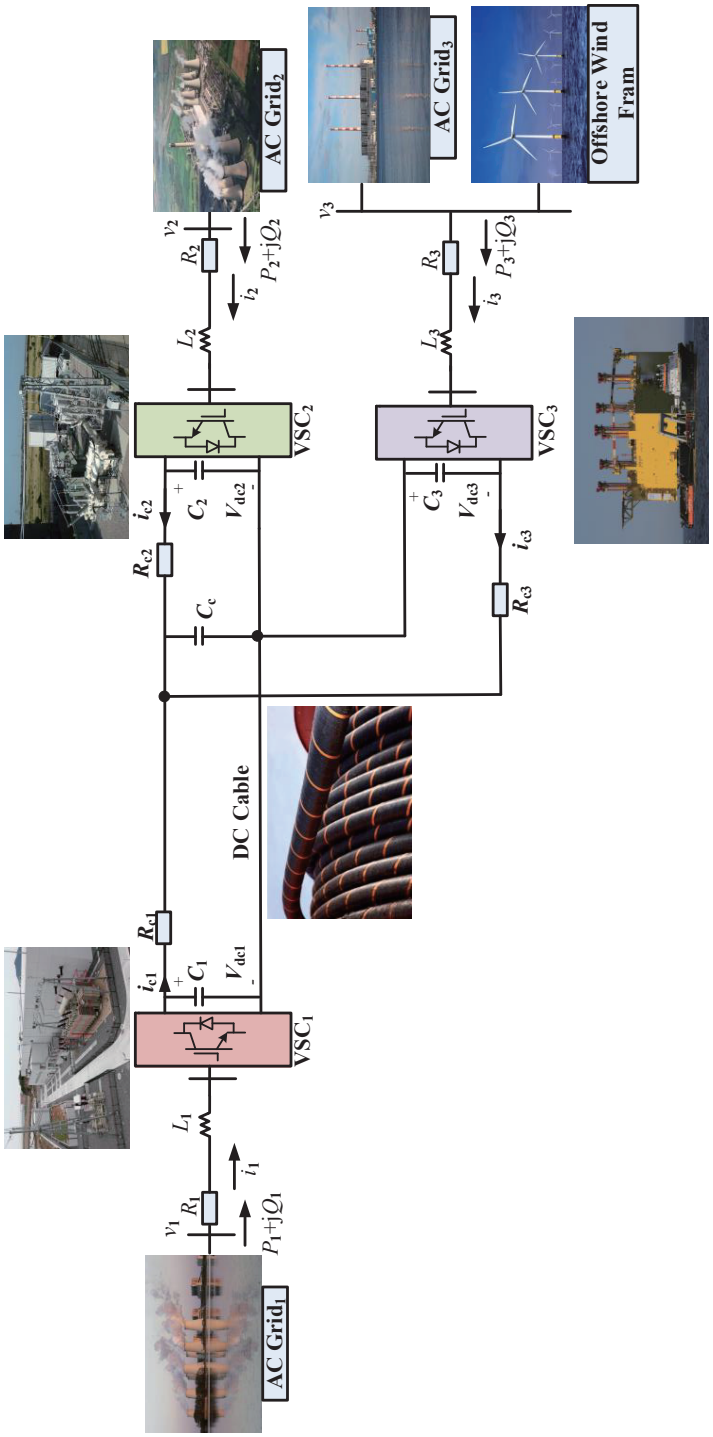

Figure 5.5: The configuration of a three-terminal radial VSC-MTDC system connecting to an offshore wind farm.

PORPC is applied on a three-terminal radial VSC-MTDC system demonstrated by Fig. 5.5, the corresponding controller parameters are tuned to improve the robustness in the presence of time-varying wind farm power outputs and weak grids connection. The three-terminal radial VSC-MTDC system parameters and the control parameters of PORPC are given in Table 5.1 and Table 5.2, respectively. According to the ratings of the individual converter station in three-terminal radial VSC-MTDC system, the droop constant is chosen to be 0.1. The detailed control block is illustrated in Fig. 5.6. The control performance of PORPC is evaluated under various operating conditions in a wide neighborhood of initial operating points, and compared to that of PI control [76, 141]and PC [133]. Due to the security requirement of converters, the control inputs are bounded as $|u_{\mathrm{q1}}| \leq 0.8$ per unit (p.u.), $|u_{\mathrm{d1}}| \leq 0.6$ p.u., $|u_{\mathrm{q}k}| \leq 0.8$ p.u., and $|u_{\mathrm{d}k}| \leq 0.6$ p.u., respectively [142].

Remark 2. For the observer gains shown in Table 1, they usually range from $10^3 - 10^5$ to provide a proper trade-off between estimation speed and peak value [63]. A larger observer gain will accelerate the estimation rate but also produce a higher peak value at the moment when system operation condition varies, while a smaller observer gain would not effectively track the output thus degrade the estimation performance significantly. This chapter chooses them to be 1250 through trial-and-error among this range. For the control gains, they are chosen as so to provide a proper trade-off between the control costs and tracking speed. A too large control gain will rapidly track the output but also result in higher control costs, while a too small control gain might not control the output fast enough but with low control costs. In this chapter, it is selected to be 75 for active power though trial-and-error, respectively. Note that a fast active power is preferred here as it is important to respond quickly for the purpose of power support.

5.4.1 Case 1: Power Regulation

The initial active power of the converter station 2 and 3 are both 40 MW. At 0.5 s, the active power reference of converter station 2 is decreased to 30 MW. And after 0.3 s, the active power reference of converter station 2 is further decreased to 20 MW. Meanwhile, the active power reference of converter 3 is increased to 50 MW

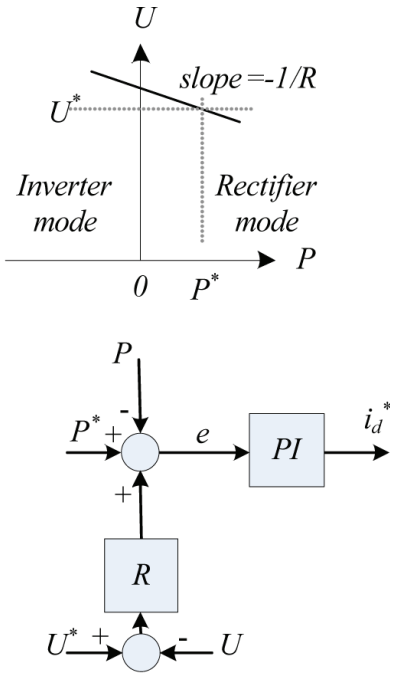

Figure 5.6: Detailed DC voltage droop control block in the VSC-MTDC systems.

Table 5.1: System parameters used in the simulation

AC grids frequency	f	50 Hz
AC grids base voltage	$V_{\mathrm{AC_{base}}}$	100 kV
DC base voltage	$V_{\mathrm{DC_{base}}}$	150 kV
System base power	S_{base}	100 MVA
AC grids resistance (25 km)	R_1, R_2, R_3	0.05 Ω/km
AC grids inductance (25 km)	L_1, L_2, L_3	0.026 mH/km
DC cable resistance (50 km)	R_0	0.21 Ω/km
DC bus capacitance	C_1, C_2, C_3	11.94 μF
Common DC capacitance	C_{c}	19.95 μF

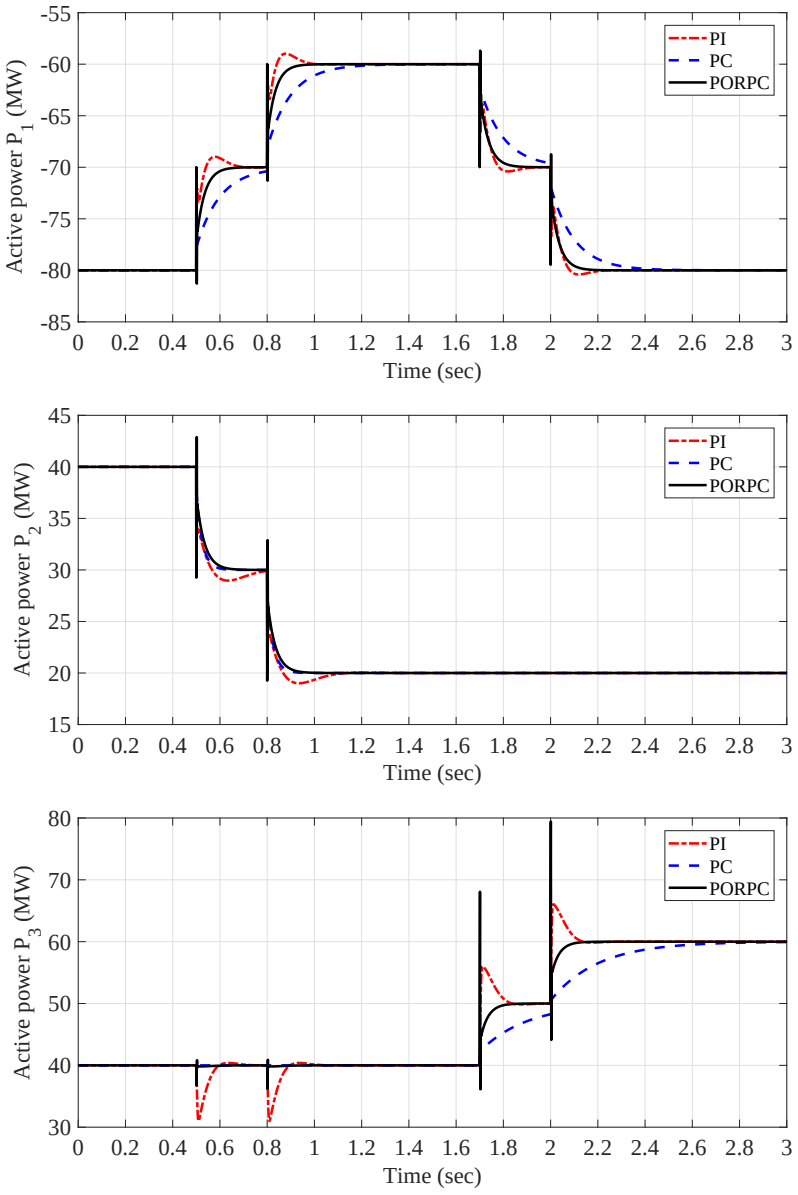

Figure 5.7: System responses obtained under normal operation condition-1.

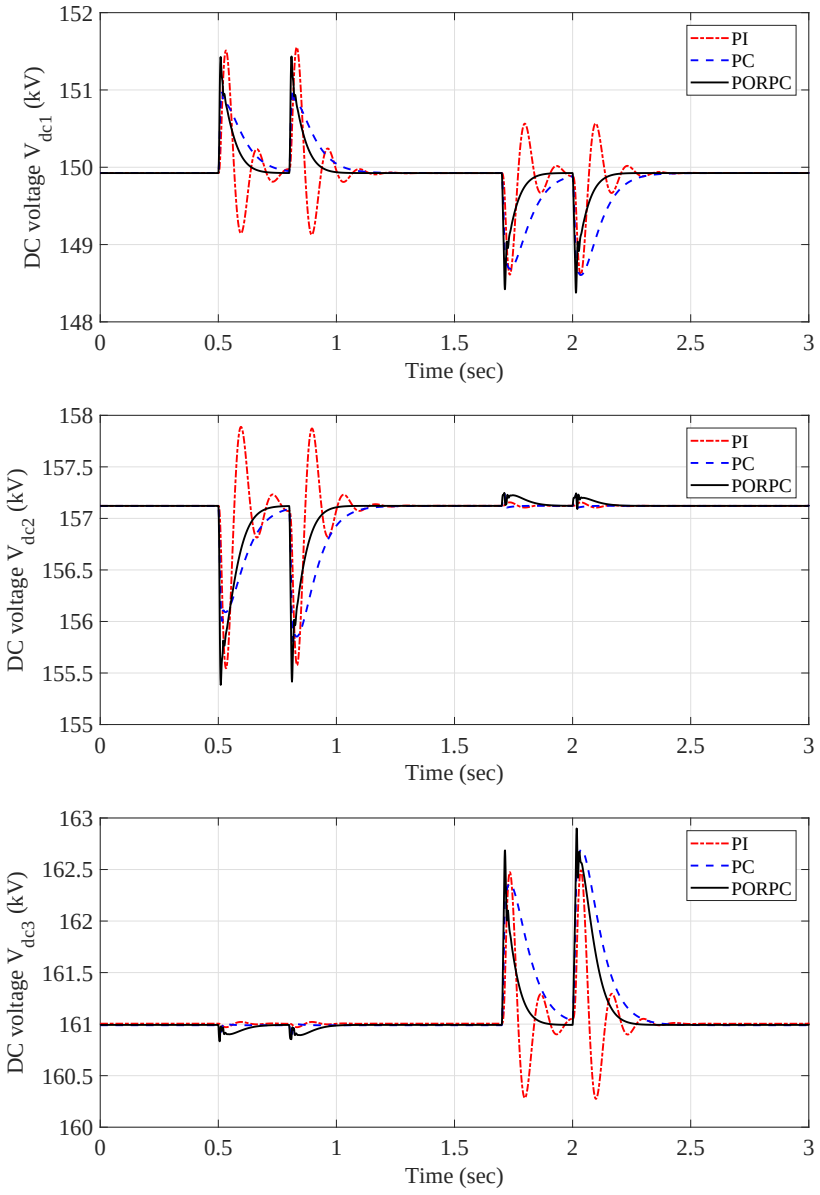

Figure 5.8: System responses obtained under normal operation condition-2.

Table 5.2: Control parameters used in the three-terminal VSC-MTDC system.

Rectifier controller parameters			
$k_{11} = 120$	$k_{12} = 25$	$\lambda_{11} = 5$	$b_{11} = 2$
$b_{12} = 0.05$	$k'_{11} = 75$	$\lambda_{12} = 5$	
Rectifier observer parameters			
$\alpha_{11} = 1250$	$\alpha_{12} = 5.2 \times 10^5$	$\alpha_{13} = 6.7 \times 10^7$	$\alpha'_{11} = 420$
$\alpha'_{12} = 5 \times 10^4$	$\Delta = 0.05\ s$	$\epsilon = 0.1$	
Inverter controller parameters, $k = 2, 3$			
$k_{k1} = 75$	$k'_{k1} = 75$	$b_{k1} = 0.1$	$b_{k2} = 0.1$
$\lambda_{k1} = 6$	$\lambda_{k2} = 6$	$\rho_k = 0.04$	
Inverter observer parameters, $k = 2, 3$			
$\alpha_{k1} = 410$	$\alpha_{k2} = 5 \times 10^4$	$\alpha'_{k1} = 420$	$\alpha'_{k2} = 4 \times 10^4$
$\Delta = 0.05\ s$	$\epsilon = 0.1$		

at 1.7 s. After 0.3 s, the active power reference of converter 2 is further increased to 60 MW. While DC voltage of the rectifier V^*_{dc1} is regulated at the rated value. The system responses are provided by Fig. 5.8. When $t = 0.5$ s, the active power of the converter station 2 decreases from 40 MW to 30 MW. Thus, the active power of the converter station 1 increases to -70 MW resulted from power balance. The converter stations 1 realizes the power balance and the DC voltage control. The active power is -80 MW initially. When $t = 0.8$ s, the active power of the converter station 2 decreases from 30 MW to 20 MW. Thus, the active power of the converter station 1 increases to -60 MW. When $t = 1.7$ s, the active power of the converter station 3 increased from 40 MW to 50 MW. Thus, the active power of the converter station 1 decreases to -70 MW. When $t = 2.0$ s, the active power of the converter station 3 decreased from 50 MW to 60 MW. Thus, the active power of the converter station 1

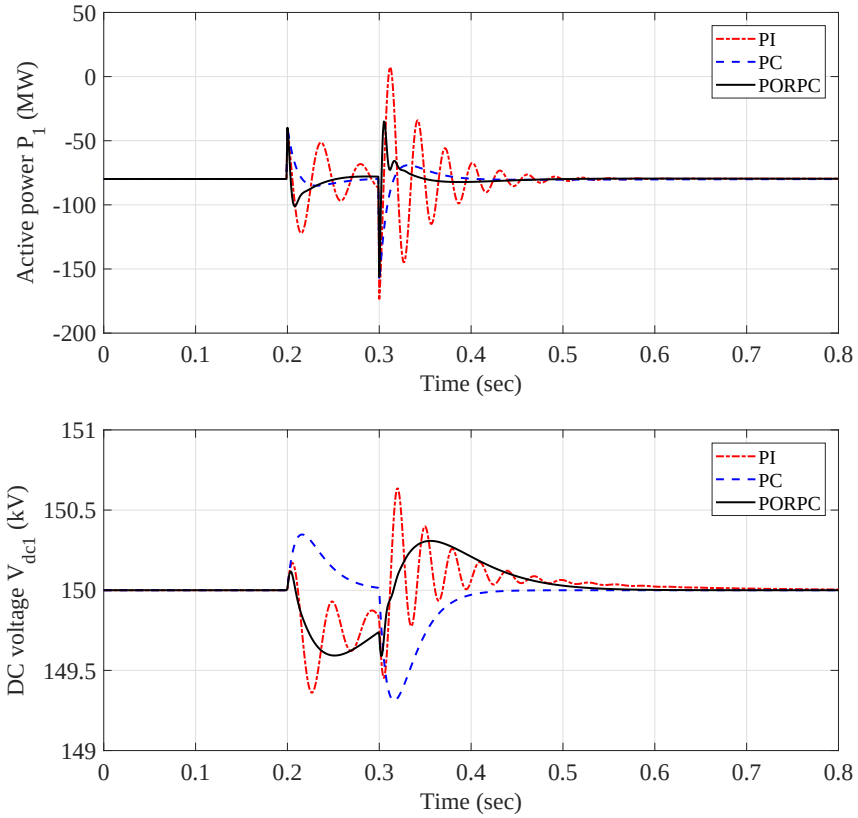

Figure 5.9: System responses obtained under the 10-cycle LLLG fault at AC bus 1.

decreases to -80 MW.

From the above analysis, one can find that the overshoot of active and reactive power is completely eliminated by PC and PORPC compared to that of PI control, which is resulted from the full compensation of nonlinearities. Note that PORPC can achieve as satisfactory control performance as that of PC due to the real-time perturbation compensation, their tiny difference is caused by the estimation error when the power tracking starts.

5.4.2 Case 2: 10-cycle line-line-line-ground (LLLG) Fault at AC Buses

A 10-cycle LLLG fault occurs at AC bus 1 from 0.2 s to 0.3 s. Due to the fault, the voltage at AC bus 1 is decreased to a critical level. Fig. 5.9 shows that PORPC

and PC can rapidly restore the system with less active power oscillations than PI control. Thus, PORPC can effectively restore the disturbed VSC-MTDC system as an extra system damping is injected.

5.4.3 Case 3: Offshore Wind Farm Connection

In order to investigate the effect of the high percentage penetration of wind power [143, 144] into the VSC-MTDC system, AC network$_3$ is connected to an offshore wind farm. Under such framework, the power grid with offshore wind farm generate time-varying wind power variation which results in a fluctuated power flow at DC terminal. To study this circumstance, a wind speed oscillation occurs from 0 s to 4 s using auto-regressive and moving average (ARMA) time series models [145] is simulated. As illustrated in Fig. 5.10, it shows that PORPC can effectively track the active and reactive power. As PORPC does not need an accurate VSC-MTDC system model, an improved control performance can be achieved compared to that of other two methods.

5.4.4 Case 4: Weak Power Grid Connection

Weak power grids are generally defined by the following two aspects [146, 147]: (1) Low effective short circuit ratio (ESCR) which means the impedance relative to the DC power is high, and (2) Low effective DC inertia constant H_{dc} which means the inertia of AC system is low. The ESCR is defined as $\frac{S-Q_{\mathrm{c}}}{P_{\mathrm{d}}}$ where S is the AC system three-phase symmetrical short-circuit level in MVA at the HVDC converter terminal at AC side. Here, P_{d} is the rated DC terminal power in MW, and Q_{c} is the value of three phase fundamental Mvar of all shunt filters and capacitor banks on the bus bar that are connected. The effective inertia constant H_{dc} is defined as $H\frac{S}{P_{\mathrm{d}}}$ where H is conventional inertia constant of the machine in the AC grid [148]. The power grids with ESCR less than 2.5 are defined as high impedance systems. The AC system with H_{dc} less 2 are defined as inadequate inertia system which has limited generation and cannot maintain the normal frequency deviation (less than 5%) [148]. This case attempts to investigate the system performance when

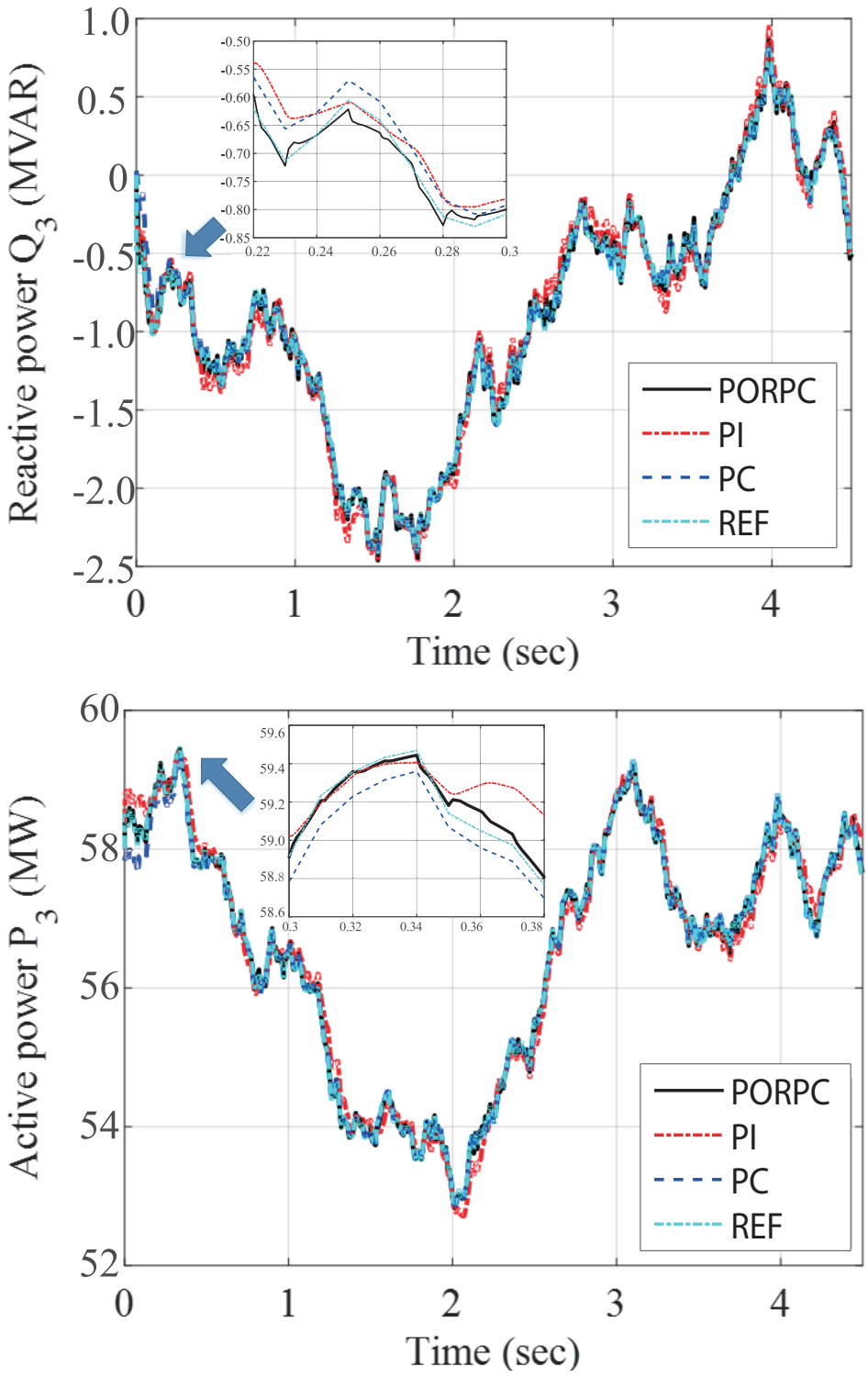

Figure 5.10: System responses obtained when an offshore wind farm is connected to the VSC-MTDC system.

Table 5.3: IAE index of different control schemes

IAE index in VSC-HVDC						
Method \ Case	Power Regulation			10-cycle LLLG Fault		
	PI	PC	PORPC	PI	PC	PORPC
$\mathrm{IAE}_{\mathrm{Q_1}}$	4.18E-02	3.26E-02	3.49E-02	2.62E-01	1.13E-01	5.54E-02
$\mathrm{IAE}_{\mathrm{V_{dc1}}}$	6.54E-03	5.16E-03	5.28E-03	1.75E-01	1.02E-01	3.71E-02
$\mathrm{IAE}_{\mathrm{Q_2}}$	3.05E-02	2.41E-02	3.02E-02	3.53E-01	2.48E-01	6.88E-02
$\mathrm{IAE}_{\mathrm{P_2}}$	3.80E-02	2.83E-02	3.03E-02	2.93E-01	3.07E-01	8.18E-02
$\mathrm{IAE}_{\mathrm{Q_3}}$	3.07E-02	2.43E-02	2.99E-02	3.52E-01	2.47E-01	6.89E-02
$\mathrm{IAE}_{\mathrm{P_3}}$	3.82E-02	2.89E-02	3.04E-02	2.92E-01	3.05E-01	8.19E-02
$\mathrm{IAE}_{\mathrm{u}}$	2.68E-01	2.88E-01	3.10E-01	1.48E-01	1.11E-01	1.14E-01
Method \ Case	Offshore Wind Farm Connection			Strong Power Grid Connection		
	PI	PC	PORPC	PI	PC	PORPC
$\mathrm{IAE}_{\mathrm{Q_3}}$	6.63E-02	6.84E-02	2.16E-02	5.13E-02	4.86E-02	2.62E-02
$\mathrm{IAE}_{\mathrm{P_3}}$	7.67E-02	1.04E-01	1.27E-02	5.71E-02	2.85E-01	2.17E-02
$\mathrm{IAE}_{\mathrm{u}}$	3.32E-02	2.99E-02	3.15E-02	2.92E-02	2.89E-02	2.35E-02
Method \ Case	Weak Power Grid Connection					
	PI	PC	PORPC			
$\mathrm{IAE}_{\mathrm{Q_2}}$	7.15E-02	6.46E-02	7.23E-02			
$\mathrm{IAE}_{\mathrm{P_2}}$	8.91E-02	3.24E-01	4.73E-02			
$\mathrm{IAE}_{\mathrm{u}}$	4.02E-02	4.19E-02	3.67E-02			

the system is made progressively weaker by decreasing effective DC inertia constant and ESCR of the AC grid with reduction of H and increase of impedance of the grid, respectively. A strong power grid which ESCR equals 4.3 and H_{dc} equals 2.7, while a weak power grid which ESCR equals 2.1 and H_{dc} equals 1.7 are connected to terminal 2 during simulation, respectively. The control performance of the test results are provided in Table 5.3.

5.4.5 Comparative Studies

To compare the control performance of each schemes in all four cases, the integral of absolute error (IAE) index is calculated and provided in Table 5.3. Here $\text{IAE}_{Q_1} = \int_0^T |Q_1 - Q_1^*|\text{d}t$, $\text{IAE}_{V_{\text{dc1}}} = \int_0^T |V_{\text{dc1}} - V_{\text{dc1}}^*|\text{d}t$, $\text{IAE}_{Q_2} = \int_0^T |Q_2 - Q_2^*|\text{d}t$, $\text{IAE}_{P_2} = \int_0^T |P_2 - P_2^*|\text{d}t$, $\text{IAE}_{Q_3} = \int_0^T |Q_3 - Q_3^*|\text{d}t$ and $\text{IAE}_{P_3} = \int_0^T |P_3 - P_3^*|\text{d}t$. The units of system variables are p.u.. The simulation time $T = 6$ s such that all system states can converge to the equilibrium point. Note that PORPC has a little bit higher IAE than PC under the nominal model due to the estimation error, while PORPC has similar IAE compared to PI control in the presence of system parameter uncertainties. However, IAE_{Q_1}, $\text{IAE}_{V_{\text{dc1}}}$, IAE_{Q_2}, IAE_{P_2}, IAE_{Q_3} and $\text{IAE}_{P_3}$of PORPC are only 15.93%, 4.68%, 13.69%, 12.87%, 13.92% and 13.3% of that of PC. Furthermore, PORPC provides greater system damping as it has the lowest IAE when the 10-cycle LLLG fault at AC buses occurs. In particular, IAE_{Q_1} and $\text{IAE}_{V_{\text{dc1}}}$ of NAC are only 21.14% and 21.2% of those of PI control when the fault occurs at AC bus 1, while IAE_{Q_2} and IAE_{P_2} of PORPC are only 19.49% and 27.92% of those of PI control when the fault occurs at AC bus 2. Finally, the overall control efforts of different approaches are also presented, here $\text{IAE}_u = \int_0^T \sum_{i=0}^{n=3}(|u_{\text{q}i}| + |u_{\text{d}i}|)dt$, one can find PORPC needs similar control efforts to that of PI control and PC but provides great robustness.

5.5 Hardware-in-the-loop Test

A dSPACE simulator based HIL real-time implementation test is carried out to test the implementation feasibility of PORPC, while the experiment platform is demonstrated in Fig. 5.11. The whole system is modelled with multiple sampling rates. The time resolution of the gating signals of industrial controllers is normally a few microseconds [149] which is far bigger than real-time simulation sampling steps. The rectifier controller (5.3.7) and inverter controller (5.3.16) are implemented on one DSP board (dSPACEDS1104) with a sampling frequency $f_{\text{c}} = 0.5$ kHz, and the VSC-MTDC system is simulated on another dSPACE platform (DS1006 board) with the limit sampling frequency $f_{\text{s}} = 50$ kHz to make HIL simulator as

close to the real plant as possible. The measurements of the reactive power Q_1, D-C voltage V_{dc1}, active power P_2, reactive power Q_2, active power P_3 and reactive power Q_3 are obtained from the real-time simulation of the VSC-MTDC system on the DS1006 board, which are sent to three controllers implemented on another DSP (dSPACEDS1104) board for the control outputs calculation.

5.5.1 HIL test: power regulation

The references of active power of converter 2 changes at $t = 0.3$ s, $t = 0.6$ s and finally decreases to 20 MW. Meanwhile, the reference of active power of converter 3 changes at $t = 1.9$ s, $t = 2.2$ s and finally increases to 60 MW, while DC voltage is regulated at the rated value $V^*_{\mathrm{dc1}} = 150$ kV as similar as case studies investigated in section 4. The system responses of HIL test and simulation are compared by Fig. 5.12, which shows HIL test results have almost the same performance as that of the simulation results. Note that when the active power of the converter station 2 changes such as at 0.3s, the active power of the converter station 2 decreases from 40 MW to 30 MW, the active power of the converter station 1 increases to -70 MW rapidly with some unavoidable propagated overshoot to keep the power balance.

5.5.2 HIL test: 10-cycle line-line-line-ground (LLLG) fault at AC bus 1.

A 10-cycle LLLG fault occurs at AC bus 1 when $t = 0.1$ s. Fig. 5.13 demonstrates that the disturbed system can be rapidly restored as expected in section 4. The system responses obtained by the HIL test is similar to that of simulation results with some communication glitches. Note that there is only tiny difference between simulation result and HIL test result in V_{dc1} caused by the measurement noise (less than 0.34%).

Remark 1. The difference between the simulation and HIL test demonstrated in Fig. 5.12 and Fig. 5.13 is mainly resulted from the following three reasons: (i) Some measurement disturbances exist in HIL test which are not regarded in the simulation, a filter can be applied to remove it and improve the control performance;

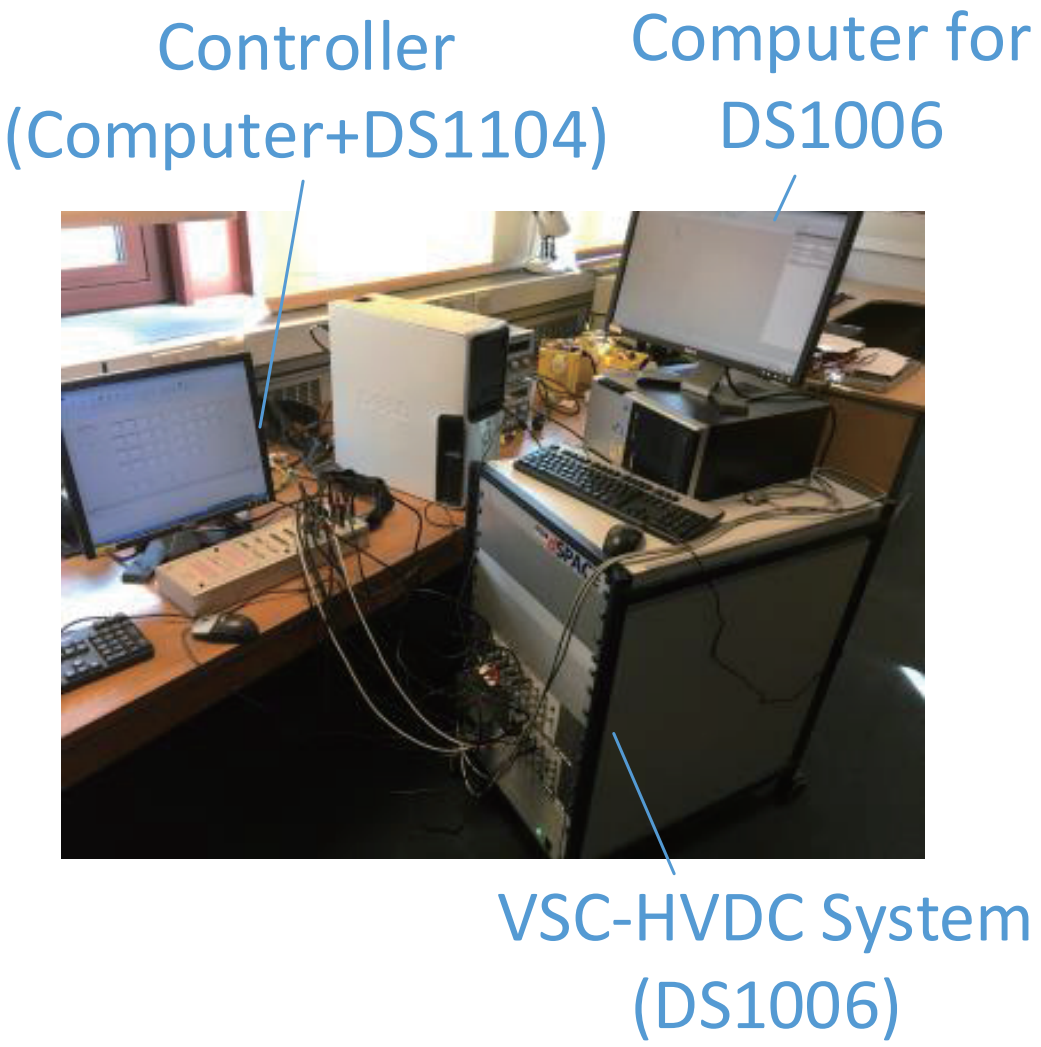

Figure 5.11: The experiment platform of the HIL test.

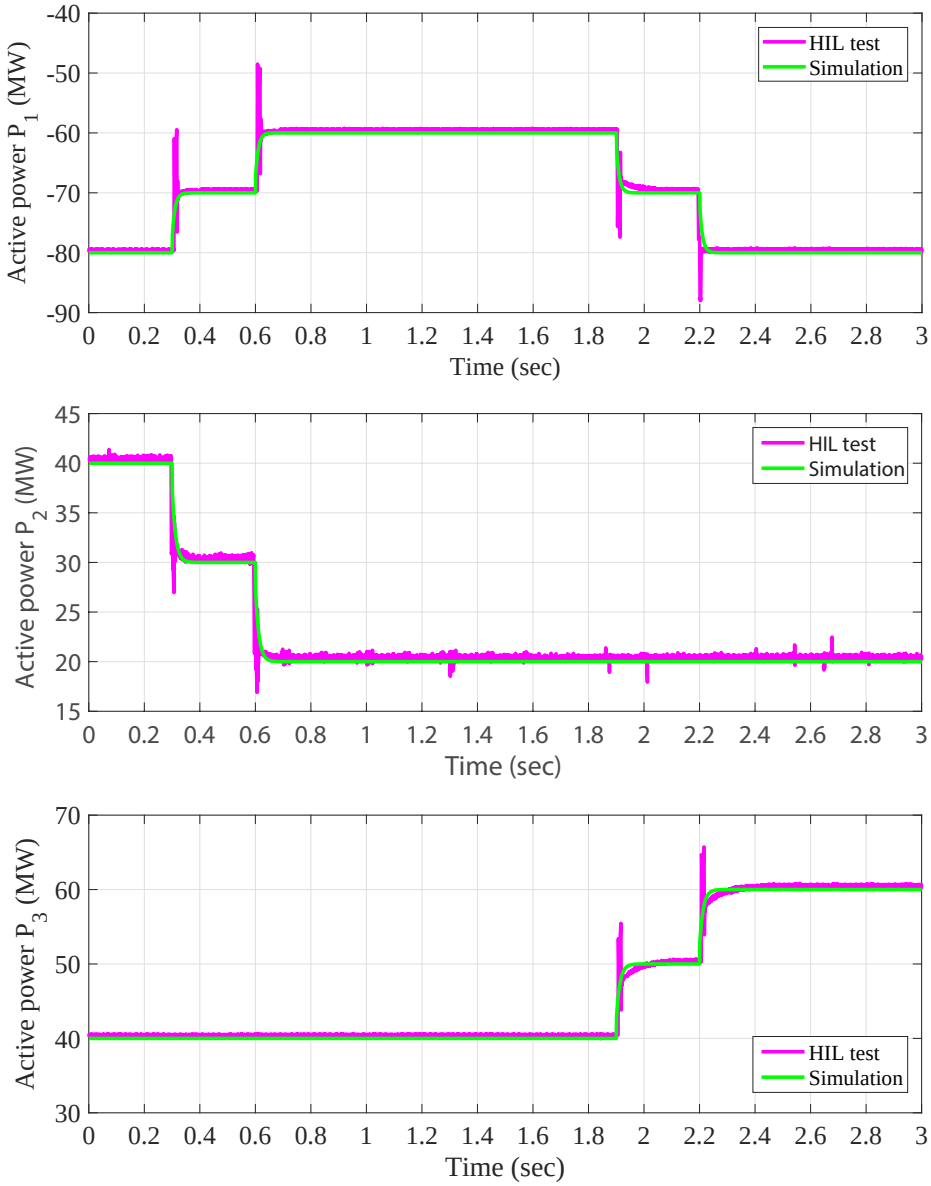

Figure 5.12: HIL test results of system responses obtained under the normal operation condition.

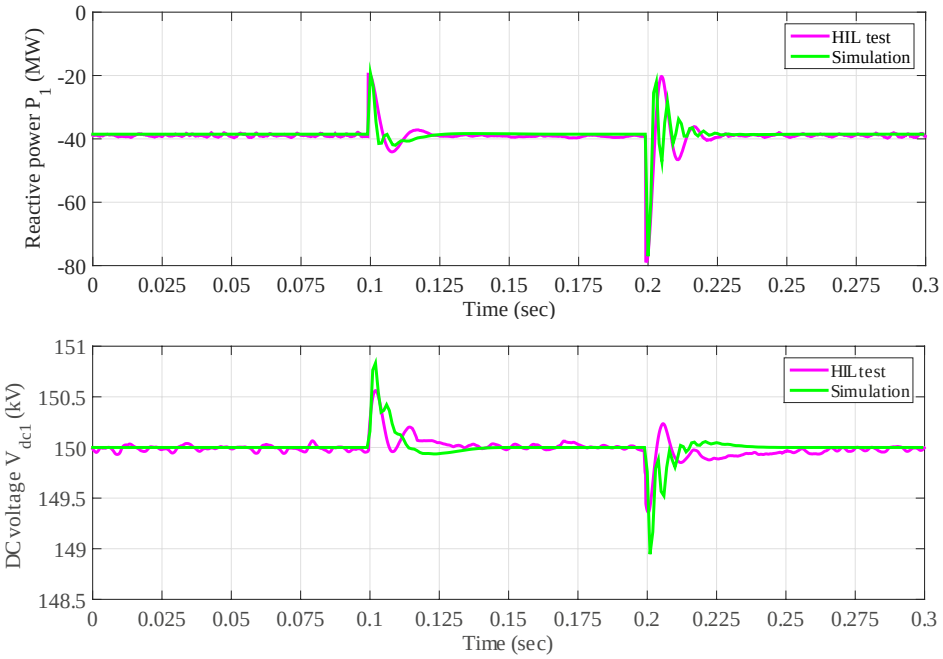

Figure 5.13: HIL test results of system responses obtained under the 10-cycle LLLG fault at AC bus 1.

(ii) The sampling holding and discretization of HIL test might introduce additional errors compared to the continuous control in the simulation; and (iii) The existence of time delay of the real-time controller, whose exact value is unlikely to obtain. A time delay $\tau = 2$ ms is assumed in the simulation.

5.6 Conclusion

This chapter develops a PORPC for the VSC-MTDC system with integrated offshore wind farm to improve the robustness against power fluctuation, system disturbances. The combinatorial effect of system nonlinearities, parameter uncertainties, unmodelled dynamics and external disturbances, e.g., grid faults and time-varying wind power output, is aggregated into a perturbation, which is fully estimated by PO and compensated by PORPC, such that a considerable robustness and improved system damping with reasonably low control efforts can be simultaneously achieved via passification. PORPC does not require an accurate VSC-MTDC system model

and only the reactive power and active power at inverter side, while DC voltage and reactive power at rectifier side need to be measured. Besides, a DC link voltage droop controller is employed to greatly improve the load share arranging response to the grid unbalanced conditions. Future study will be focused on employing optimization algorithms, e.g., genetic algorithm (GA) or particle swarm optimization (PSO), to optimize the parameters selection procedure of PORPC. Four case studies have been undertaken to evaluate the control performance of the proposed approach, including power regulation, AC bus fault, offshore wind farm integration, and weak power grids connection, respectively. Simulation results verify that PORPC can maintain consistent control performance and provide significant robustness under various operation conditions of VSC-MTDC with wind farm integration. Moreover, an HIL test has been carried out through dSPACE simulator which validates the implementation feasibility of the proposed scheme.

As presented in this chapter, the PORPC based control strategy is applied to the VSC-MTDC system, and corresponding dynamic performance has been improved. In the next chapter, the conclusion of the thesis and corresponding further discussion will be given.

Chapter 6

Conclusions and Future Works

6.1 Conclusions

As the summary of the results obtained in this thesis, the research works presented have effectively improved the dynamic performance of the VSC-HVDC system via developing advanced control strategies for different control layers. Hence in the practical application projects, the potentialities of VSC-HVDC system can be further developed. As the first part of this thesis, the general background of the HVDC is provided in Chapter 1. Differing from the classic LCC based HVDC, VSC-HVDC is emphasized for its variable application purposes in the recent practical projects. MMC which is the most popular VSC topology option adopted by recent VSC-HVDC practical projects has also been introduced. The first chapter in this thesis also provide the general research review on control strategies which are applied to MMC current regulation, point-to-point VSC-HVDC system control, FRT capability enhancement of VSC-HVDC system with wind farm integration and coordinated operation of MTDC with wind farm integration.

The other parts of the research work presented in this thesis can be summarized as follows:

- Passivity of the system is derived for stabilization independently of the notion of energy shaping. Passivity based control is proposed to improve system damping performance via passivation which remaining the parts of useful sys-

tem nonlinearities. Through applying the PBC in the MMC lower-level current controller in chapter 2, the control costs can be effectively saved while ensuring the system global stability.

- The robustness of the two-terminal VSC-HVDC system requires to be investigated and improved due to its variable application purposes. SMC is proposed in VSC converter higher-level voltage controller for its inherent advantages of enhancing system robustness against some system disturbances. Considering the operation conditions of the two-terminal VSC-HVDC systemone improved SMC which is named as POSMC is proposed in chapter 3 for suppressing the chatting effects and enhancing the robustness against comprehensive perturbation via adopting SMSPO.

- The FRT requirements inspired by nowadays strict grid code raise the challenges for transmission system which is used for renewable energy source integration. VSC-HVDC transmission system is regarded as the favourable solution for renewable energy source integration, especially offshore wind farm integration due to its inherent benefits. FRT capability of offshore wind farms with VSC-HVDC transmission systems connected is investigated. NAC is applied in VSC voltage higher-level controller for FRT capability enhancement and combined with the de-loading strategy which is designed deliberately for offshore wind farm FRT processes. Hence the FRT capability of VSC-HVDC transmission system with offshore wind farms integration is enhanced efficiently without installing any extra hardware devices.

- Recently MTDC system draws attention to the future embedded DC grid planning. With renewable energy sources connection and future flexible operation requirements between generation and load, the stability of the MTDC requires investigation and corresponding efficient guarantee means. Enhanced PBC which is called as PORPC is proposed in converter higher-level voltage controller to enhance the robustness against system uncertainties. As mentioned above, through comparative studies on different controllers, the proposed controller can handle 80%-120% system parameter mismatches. PORPC is com-

bined with well-proven droop control strategy which is essential to the MTDC and micro-grid for proper load sharing under various operation conditions especially grid unbalance condition.

Necessary simulations and HIL tests are implemented for validating the effectiveness of the proposed controllers. Since the effectiveness of the proposed controllers have already been validated on investigated HVDC applications mentioned above. However, there are some limitations need to be mentioned. Because of the complexity of the proposed controllers, the proposed controllers require state-of-the-art controller hardware for implementation. Although VSC-HVDC system is modern technology, many projects which were built ten years ago lack equipping modern DSP for controllers and corresponding adequate computation capability for advanced controllers. Therefore not all VSC-HVDC systems can be equipped with proposed controllers. Besides, conventional LCC-HVDC systems still hold half share for nowadays HVDC market which lack controllability in converters. Proposed advanced control methods are also not suitable for these built LCC-HVDC systems. As for dual-infeed HVDC system which was proposed recently, the effectiveness of advanced controller remains to be validated.

6.2 Future Works

Several related research directions which deserve further investigations are stated as follows:

- Advanced control theory used in this thesis can be further optimized via further combination. For example, PBC which is applied for MMC low-level current controller in chapter 2 . can be integrated into two-terminal VSC-HVDC system with POSMC mentioned in chapter 3. However, the integration requires more complex HVDC mathematic model which is totally different from mathematic model mentioned in chapter 2 and 3. Better dynamic performance is expected to be achieved via integration but more complex mathematic model remains to be developed.

- Hardware implementation of advanced control theory is one serious obstacle during the advanced control application process. Current computation capability limitation of the existing controller hardware like DSP, FPGA and CPU requires optimization on designing advanced controller. Controller is required to be designed to be more robust to face the time delay brought hardware computation limitation.

- For controller parameter tuning, there is various optimisation methods under rapid development. Future study will be focused on employing optimization algorithms, e.g., genetic algorithm (GA) or particle swarm optimization (PSO), to optimize the parameters selection procedure of control method proposed in the thesis

- Other system overriding control strategies like power synchronization control will take into consideration with advanced converter controller. Integrating with more controllers in different layers requires further investigation on system mathematic model. Hence system mathematic model will also be investigated and developed in the future study.

References

[1] D. Van Hertem, O. Gomis-Bellmunt, and J. Liang, *HVDC Grids for Offshore and Supergrid of the Future*. New York, NY, USA: Wiley, 2016.

[2] M. Barnes, D. Van Hertem, S. P. Teeuwsen, and M. Callavik, "HVDC systems in smart grids," *Proc. IEEE* , vol. 105, no. 11, pp. 2082-2098, Nov. 2017.

[3] M. Callavik, M. Larsson, and S. Stoeter, "Powering the world," *ABB Rev.*, Jul. 2014.

[4] Transnet BW, Ultranet, 2017. [Online]. Available: https://www.transnetbw.de/de/ ultranet/

[5] M. Marz et al., "Mackinac HVDC converter automatic runback utilizing locally measured quantities," in *Proc. CIGR*, Toronto, ON, Canada, Sep. 2014, pp. 22-24. [Online].

[6] R. Chinnasamy, "Analysis of the global HVDC and FACTS market," in *Industry Research Reports*. San Antonio, TX, USA: Frost Sullivan, Sep. 2015.

[7] S. Thorburn and T. Jonsson, "AC/DC Backing up AC grids with DC technology," *ABB Rev.*. Jul. 2014.

[8] K. Sharifabadi, L. Harnefors, H.P. Nee, R. Teodorescu, and S. Norrga, *Design, Control and Application of Modular Multilevel Converters for HVDC Transmission Systems.* New York, NY, USA: Wiley, 2016.

[9] M. Eremia and C.C. Liu, *Advanced Solution in Power Systems: HVDC, FACT, and Artificial Intelligence.* New York, NY, USA: Wiley, 2016.

[10] O. Heyman, "HVDC lightłIts time to connect," ABB, Ludvika, Sweden, Tech. Rep., Dec. 2012.

[11] R. Burns, *Advanced Control Engineering*, Butterworth-Heinemann, 2001.

[12] K. Liu, and Y. Yu. *Robust Control : Theory and Applications,* John Wiley & Sons, Incorporated, 2016.

[13] S. Yang, P. Wang, and Y. Tang, "Feedback linearization-based current control strategy for modular multilevel converters," *IEEE Trans. Power Electron.*, vol. 33, no. 1, pp. 161-174, Jan. 2018.

[14] L. Harnefors, A. Antonopoulos, S. Norrga, L. Angquist, and H. P. Nee, "Dynamic analysis of modular multilevel converters," *IEEE Trans. Ind. Electron.*, vol. 60, no. 7, pp. 2526-2537, Jul. 2013.

[15] M. Hagiwara and H. Akagi, "Control and experiment of pulsewidthmodulated modular multilevel converters," *IEEE Trans. Power Electron.*, vol. 24, no. 7, pp. 1737-1746, Jul. 2009.

[16] Q. Tu, Z. Xu, and L. Xu, "Reduced switching-frequency modulation and circulating current suppression for modular multilevel converters," *IEEE Trans. Power Del.*, vol. 26, no. 3, pp. 2009-2017, Jul. 2011.

[17] R. Lizana, M. A. Perez, D. Arancibia, J. R. Espinoza, and J. Rodriguez, "Decoupled current model and control of modular multilevel converters," *IEEE Trans. Ind. Electron.*, vol. 62, no. 9, pp. 5382-5392, Sep. 2015.

[18] B. Bahrani, S. Debnath, and M. Saeedifard, "Circulating current suppression of the modular multilevel converter in a double-frequency rotating reference frame," *IEEE Trans. Power Electron.*, vol. 31, no. 1, pp. 783-792, Jan. 2016.

[19] Z. Li, P. Wang, Z. Chu, H. Zhu, Y. Luo, and Y. Li, "An inner current suppressing method for modular multilevel converters," *IEEE Trans. Power Electron.*, vol. 28, no. 11, pp. 4873-4879, Nov. 2013.

[20] S. Li, X.Wang, Z.Yao, T. Li, and Z. Peng, "Circulating current suppressing strategy for MMC-HVDC based on nonideal proportional resonant controllers under unbalanced grid conditions," *IEEE Trans. Power Electron.*, vol. 30, no. 1, pp. 387-397, Jan. 2015.

[21] L. He, K. Zhang, J. Xiong, and S. Fan, "A repetitive control scheme for harmonic suppression of circulating current in modular multilevel converters," *IEEE Trans. Power Electron.*, vol. 30, no. 1, pp. 471-481, Jan. 2015.

[22] M. Zhang, L. Huang, W. Yao, and Z. Lu, "Circulating harmonic current elimination of a CPS-PWM-based modular multilevel converter with a plug-in repetitive controller," *IEEE Trans. Power Electron.*, vol. 29, no. 4, pp. 2083-2097, Apr. 2014.

[23] J. Qin and M. Saeedifard, "Predictive control of a modular multilevel converter for a back-to-back HVDC system," *IEEE Trans. Power Del.*, vol. 27, no. 3, pp. 1538-1547, Jul. 2012.

[24] M. Vatani, B. Bahrani, M. Saeedifard, and M. Hovd, "Indirect finite control set model predictive control of modular multilevel converters," *IEEE Trans. Smart Grid*, vol. 6, no. 3, pp. 1520-1529, May. 2015.

[25] B. S. Riar, T. Geyer, and U. K. Madawala, "Model predictive direct current control of modular multilevel converters: Modeling, analysis, and experimental evaluation," *IEEE Trans. Power Electron.*, vol. 30, no. 1, pp. 431-439, Jan. 2015.

[26] L. Ben-Brahim, A. Gastli, M. Trabelsi, K. A. Ghazi, M. Houchati, and H. Abu-Rub, "Modular multilevel converter circulating current reduction using model predictive control," *IEEE Trans. Ind. Electron.*, vol. 63, no. 6, pp. 3857-3866, Jun. 2016.

[27] H. Barnklau, A. Gensior, and J. Rudolph, "A model-based control scheme for modular multilevel converters," *IEEE Trans. Ind. Electron.*, vol. 60, no. 12, pp. 5359-5375, Dec. 2013

[28] R. Ortega, A. Loria, P. J. Nicklasson, and H. Sira-Ramirez, PassivityBased Control of Euler-Lagrange Systems. London, U.K.: Springer Verlag, 1998.

[29] T. M. Haileselassie, M. Molinas, and T. Undeland, "Multi-terminal VSCHVDC system for integration of offshore wind farms and green electrification of platforms in the North Sea," *presented at the Nordic Workshop Power Ind. Electron.*, Otakaari, Finland, Jun. 9-11, 2008.

[30] S. Li, T. A. Haskew, and L. Xu, "Control of HVDC light system using conventional and direct current vector control approaches," *IEEE Trans. Power Electron.*, vol. 25, no. 12, pp. 3106-3118, Dec. 2010.

[31] S. Y. Ruan, G. J. Li, L. Peng, Y. Z. Sun, and T. T. Lie, "A nonlinear control for enhancing HVDC light transmission system stability," *Electrical Power and Energy Syst.*, vol. 29, pp. 565-570, 2007.

[32] M. Durrant, H. Werner, and K. Abbott, "Synthesis of multi-objective controllers for a VSC HVDC terminal using LMIs," in *Proc. IEEE Conf. Decision and Control*, pp. 4473-4478, Dec. 2004.

[33] S. Y. Ruan, G. J. Li, X. H. Jiao, Y. Z. Sun, and T. Lie, "Adaptive control design for VSC-HVDC systems based on backstepping method," *Elect. Power Syst. Res.*, vol. 77, pp. 559-565, Apr. 2007.

[34] L. Zhang, L. Harnefors, and H. Nee, "Interconnection of two very weak AC systems by VSC-HVDC links using power-synchronization control," *IEEE Trans. Power Syst.*, vol. 26, no. 1, pp. 344-355, July 2011.

[35] A. D. S. Lordelo and H. A. Fazzolari, "On interval goal programming switching surface robust design for integral sliding mode control," *Control Eng. Pract.*, vol. 32, pp. 136-146, Jul. 2014.

[36] Q. Zong, Z. S. Zhao and J. Zhang, "Higher order sliding mode control with self-tuning law based on integral sliding mode," *IET Contr. Theory Appl.*, Vol.4, No.7, 1282-1289, 2010.

[37] M. Gokasan, S. Bogosyan and D. J. Goering "Sliding mode based powertrain control for efficiency improvement in series hybrid-electric vehicles," *IEEE Trans. Power Electron.*, vol. 21, no. 3, pp. 779-790, May 2006.

[38] A. Kessal and L. Rahmani, "Ga-optimized parameters of sliding-mode controller based on both output voltage and input current with an application in the PFC of AC/DC converters," *IEEE Trans. Power Electron.*, vol. 29, no. 6, pp. 3159-3165, June 2014.

[39] C. Lascu, I. Boldea, and F. Blaabjerg, "Direct torque control of sensorless induction motor dirves: A sliding-mode approach," *IEEE Trans. Ind. Electron.*, vol. 40, no. 2, pp. 582-590, Mar./Apr. 2004.

[40] B. Beltran, T. Ahmed-Ali, and M. E. H. Benbouzid, "Sliding mode power control of variable-speed wind energy conversion systems," *IEEE Trans. Ind. Electron.*, vol. 56, no. 9, pp. 3314-3321, Jun. 2008.

[41] A. Moharana and P. K. Dash, "Input-output linearization and robust sliding-mode controller for the VSC-HVDC transmission link," *IEEE Trans. Power Del.*, vol. 25, no. 3, pp. 1952-1961, July 2010.

[42] C. Edwards and S.K. Spurgeon, *Sliding Mode Control: Theory and Applications.* New York: Taylor & Francis, 1998.

[43] A. Moawwad, M. S. El Moursi, and W. Xiao, "Advanced fault ride-through management scheme for VSC-HVDC connecting offshore wind farms," *IEEE Trans. Power Syst.*, vol. 31, no. 6, pp. 4923-4934, Nov. 2016.

[44] S. Nanou, G. Patsakis, and S. Papathanassiou, "Assessment of communication-independent grid code compatibility solutions for VSC-HVDC connected offshore wind farms," *Electr. Power Syst. Res.*, vol.121, pp. 38-51, Apr. 2015.

[45] V. Yaramasu, B. Wu, P. C. Sen, S. Kouro, and M. Narimani,"High-power wind energy conversion systems: state-of-the-art and emerging technologies," *Proc. IEEE*, vol. 103, no. 5, pp. 740-788, May 2015

[46] Requirements for Offshore Grid Connections in the Grid of TenneT TSO GmbH, TenneT TSO GmbH, Bayreuth, Germany, December 2012.

[47] M. I. Daoud, A. M. Massoud, A. S. Abdel-Khalik, A. Elserougi, and S. Ahmed, "A flywheel energy storage system for fault ride through support of grid-connected VSC HVDC-based offshore wind farms," *IEEE Trans. Power Syst.*, vol. 31, no. 3, pp. 1671-1680, May 2016.

[48] A. Kirakosyan, M. S. E. Moursi and V. Khadkikar, "Fault Ride Through and Grid Support Topology for the VSC-HVDC Connected Offshore Wind Farms," *IEEE Trans. Power Del.*, vol. 32, no. 3, pp. 1592-1604, Jun. 2017

[49] T. D. Vrionis, X. I. Koutiva, N. A. Vovos, and G. B. Giannakopoulos, "Control of an HVdc link connecting a wind farm to the grid for fault ride-through enhancement," *IEEE Trans. Power Syst.*, vol. 22, no. 4, pp. 2039-2047, Nov. 2007.

[50] L. Xu, L. Yao, and C. Sasse, "Grid integration of large DFIG-based wind farms using VSC transmission," *IEEE Trans. Power Syst.*, vol. 22, no. 3, pp. 976-384, Aug. 2007.

[51] C. Feltes, H. Wrede, F. W. Koch and I. Erlich, "Enhanced Fault Ride-Through Method for Wind Farms Connected to the Grid Through VSC-Based HVDC Transmission," *IEEE Trans. Power Syst.*,vol. 24, no. 3, pp. 1537-1546, Aug. 2009.

[52] G. Ramtharan, A. Arulampalam, J. B. Ekanayake, F. M. Hughes, and N. Jenkins, "Fault ride through of fully rated converter wind turbines with AC and DC transmission systems," *IET Renew. Power Gener.*,vol. 4, pp. 426-438, 2009.

[53] I. Erlich, C. Feltes, and F. Shewarega, "Enhanced voltage drop control by VSC-HVDC systems for improving wind farm fault ridethrough capability," *IEEE Trans. Power Del.*, vol. 29, no. 1, pp. 378-85, Feb. 2014.

[54] A. Mullane, G. Lightbody, and R. Yacamini, "Wind turbine fault ride through enhancement," *IEEE Trans. Power Syst.*, vol. 20, no. 4, pp.1929-1937, Nov. 2005.

[55] Q. H. Wu, L. Jiang, and J. Y. Wen, "Decentralized adaptive control of interconnected non-linear systems using high gain observer," *Int. J. Control*, vol. 77, no. 8, pp. 703-712, 2004.

[56] L. Jiang, Q. H. Wu, and J. Y. Wen, "Decentralized nonlinear adaptive control for multi-machine power systems via high-gain perturbation observer," *IEEE Trans. Circuits Syst. I, Reg. Papers.*, vol. 51, no. 10, pp. 2052-2059, 2004.

[57] J. Chen, L. Jiang, Wei Yao, and Q. H. Wu, "Perturbation estimation based nonlinear adaptive control of a full-rated converter wind turbine for fault ride-through capability enhancement," *IEEE Trans. Power Syst.*, vol. 29, no. 6, pp. 2733-2743, 2014

[58] N. R. Chaudhuri and B. Chaudhuri, "Adaptive droop control for effective power sharing in multi-terminal dc (MTDC) grids," *IEEE Trans. Power Syst.*, vol. 28, no. 1, pp. 21-29, Feb. 2013.

[59] X. Zhao and K. Li, "Adaptive backstepping droop controller design for multi-terminal high-voltage direct current systems," *IET Gener., Transm. Distrib.*, vol. 9, no. 10, pp. 975-983, 2015.

[60] G. Stamatiou and M. Bongiorno, "Power-dependent droop-based control strategy for multi-terminal HVDC transmission grids," *IET Gener., Transm. Distrib.*, vol. 11, no. 2, pp. 383-391, 2017.

[61] B. Yang, L. Jiang, W. Yao, and Q. H. Wu, "Perturbation estimation based coordinated adaptive passive control for multimachine power systems," *Control Eng. Pract.*, vol. 44, pp. 172-192, 2015

[62] L. Harnefors, A. G. Yepes, A. Vidal, and J. Doval-Gandoy, "Passivity-based controller design of grid-connected VSCs for prevention of electrical reso-

nance instability," *IEEE Trans. Ind. Electron.*, vol. 62, no. 2, pp. 702-710, Feb. 2015.

[63] B. Yang, L. Jiang, W. Yao, and Q. H. Wu, "Perturbation observer based adaptive passive control for damping improvement of multi-terminal voltage source converter-based high voltage direct current systems" *Trans. Inst. Meas. Control*, vol. 39, no. 9, pp. 1409-1420, 2017

[64] S. Debnath, J. Qin, B. Bahrani, M. Saeedifard, and P. Barbosa, "Operation, control, and applications of the modular multilevel converter: A review," *IEEE Trans. Power Electron.*, vol. 30, no. 1, pp. 37-53, Jan. 2015.

[65] M. A. Perez, S. Bernet, J. Rodriguez, S. Kouro, and R. Lizana, "Circuit topologies, modeling, control schemes, and applications of modular multilevel converters," *IEEE Trans. Power Electron.*, vol. 30, no. 1, pp. 4-17, Jan. 2015

[66] M. Saeedifard, R. Iravani, "Dynamic performance of a modular multilevel back-to-back HVDC system," *IEEE Trans. Power Del.*, vol. 25, no. 4, pp. 2903-2912, Oct. 2010.

[67] R. Ortega and G. Espinosa, "Torque regulation of induction motors," *Automatica*, vol. 29, no. 3, pp. 621-633, 1993.

[68] H. Sira-Ramirez, R. A. Perez-Moreno, R. Ortega, and M. Garcia-Esteban, "Passivity-based controllers for the stabilization of DC-to-DC power converters," *Automatica*, vol. 33, no. 4, pp. 499-513, 1997.

[69] A. M. Stankovic, D. J. Perreault, and K. Sato, "Synthesis of dissipative nonlinear controllers for series resonant DC/DC converters," *IEEE Trans. Power Electron.*, vol. 14, pp. 673-682, July 1999.

[70] H. Saad, X. Guillaud, J. Mahseredjian, S. Dennetiere, and S. Nguefeu, "MMC capacitor voltage decoupling and balancing controls," *IEEE Trans. Power Del.*, vol. 30, no. 2, pp. 704-712, Apr. 2015.

[71] R. Ortega, A. J. Van Der Schaft, I. Mareels and B. Maschke, "Putting energy back in control," in *IEEE Control Systems Magazine*, vol. 21, no. 2, pp. 18-33, April 2001.

[72] N. Flourentzou, V. G. Agelidis, and G. D. Demetriades, "VSC-based HVDC power transmission systems: an overview," *IEEE Trans. Power Electron.*, vol. 24, no. 3, pp. 592-602, Mar. 2009.

[73] D. V. Hertema and M. Ghandhari, "Multi-terminal VSC HVDC for the European supergrid: Obstacles," *Renewable Sustainable Energy Rev.*, no. 14, pp. 3156-3163, 2010.

[74] L. Zhang, L. Harnefors and H. P. Nee, "Modeling and control of VSC-HVDC links connected to island systems," *IEEE Trans. Power Syst.*, vol. 26, no. 2, pp. 783-793, May, 2011.

[75] T. M. Haileselassie, M. Molinas, and T. Undeland, "Multi-terminal VSCHVDC system for integration of offshore wind farms and green electrification of platforms in the North Sea," *presented at the Nordic Workshop Power Ind. Electron.*, Otakaari, Finland, Jun. 9-11, 2008.

[76] S. Li, T. A. Haskew, and L. Xu, "Control of HVDC light system using conventional and direct current vector control approaches," *IEEE Trans. Power Electron.*, vol. 25, no. 12, pp. 3106-3118, Dec. 2010.

[77] S. Y. Ruan, G. J. Li, L. Peng, Y. Z. Sun, and T. T. Lie, "A nonlinear control for enhancing HVDC light transmission system stability," *Electrical Power and Energy Syst.*, vol. 29, pp. 565-570, 2007.

[78] M. Durrant, H. Werner, and K. Abbott, "Synthesis of multi-objective controllers for a VSC HVDC terminal using LMIs," in *Proc. IEEE Conf. Decision and Control*, pp. 4473-4478, Dec. 2004.

[79] S. Y. Ruan, G. J. Li, X. H. Jiao, Y. Z. Sun, and T. Lie, "Adaptive control design for VSC-HVDC systems based on backstepping method," *Elect. Power Syst. Res.*, vol. 77, pp. 559-565, Apr. 2007.

[80] L. Zhang, L. Harnefors, and H. Nee, "Interconnection of two very weak AC systems by VSC-HVDC links using power-synchronization control," *IEEE Trans. Power Syst.*, vol. 26, no. 1, pp. 344-355, July 2011.

[81] J. Hu, Z. D. Wang, H. J. Gao, and L. K. Stergioulas "Robust sliding mode control for discrete stochastic systems with mixed time delays, randomly occurring uncertainties, and randomly occurring nonlinearities," *IEEE Trans. Ind. Electron.*, vol. 59, no. 7, pp. 3008-3015, July 2012.

[82] W. Huo "Predictive variable structure control of nonholonomic chained systems," *International Journal of Computer Mathematics-Computer Mathematics in Dynamics and Control*, vol. 85, no. 6, pp. 949-960, June 2008.

[83] Q. Zong, Z. S. Zhao and J. Zhang "Higher order sliding mode control with self-tuning law based on integral sliding mode," *IET Control Theory Appl.*, vol. 4, no. 7, pp. 1282-1289, July 2010.

[84] M. Gokasan, S. Bogosyan and D. J. Goering "Sliding mode based powertrain control for efficiency improvement in series hybrid-electric vehicles," *IEEE Trans. Power Electron.*, vol. 21, no. 3, pp. 779-790, May 2006.

[85] A. Kessal and L. Rahmani, "Ga-optimized parameters of sliding-mode controller based on both output voltage and input current with an application in the PFC of AC/DC converters," *IEEE Trans. Power Electron.*, vol. 29, no. 6, pp. 3159-3165, June 2014.

[86] C. Lascu, I. Boldea, and F. Blaabjerg, "Direct torque control of sensorless induction motor dirves: A sliding-mode approach," *IEEE Trans. Ind. Electron.*, vol. 40, no. 2, pp. 582-590, Apr. 2004.

[87] B. Beltran, T. Ahmed-Ali, and M. E. H. Benbouzid, "Sliding mode power control of variable-speed wind energy conversion systems," *IEEE Trans. Ind. Electron.*, vol. 56, no. 9, pp. 3314-3321, Jun. 2008.

[88] A. Moharana and P. K. Dash, "Input-output linearization and robust sliding-mode controller for the VSC-HVDC transmission link," *IEEE Trans. Power Del.*, vol. 25, no. 3, pp. 1952-1961, July 2010.

[89] C. Edwards and S. Spurgeon, "Sliding mode control: theory and applications," CRC Press, 1998.

[90] C. Johnson, "Accommodation of external disturbances in linear regulator and servomechanism problems," *IEEE Trans. Autom. Control*, vol. 16, no. 6, pp. 635-644, Dec. 1971.

[91] W. H. Chen, D. J. Ballance, P. J. Gawthrop, and J. O'Reilly, "A nonlinear disturbance observer for robotic manipulators," *IEEE Trans. Ind. Electron.*, vol. 47, no. 4, pp. 932-938, Aug. 2000.

[92] J. H. She, M. Fang, Y. Ohyama, H. Hashimoto, and M. Wu, "Improving disturbance-rejection performance based on an equivalent-inputdisturbance approach," *IEEE Trans. Ind. Electron.*, vol. 55, no. 1, pp. 380-389, Jan. 2008.

[93] J. Q. Han. "From PID to active disturbance rejection control," *IEEE Trans. Ind. Electron.*, vol. 56, pp. 900-906, Mar. 2009.

[94] L. Sun, J. Dong, D. Li, and K. Y. Lee, "A practical multivariable control approach based on inverted decoupling and decentralized active disturbance rejection control," *Ind. Eng. Chem. Res.*, vol 55, no. 7, pp. 2008-2019, Jan. 2016.

[95] B. Z. Guo and Z. L. Zhao, "On the convergence of an extended state observer for nonlinear systems with uncertainty," *Systems & Control Letters*, vol. 60, no. 6, pp. 420-430, June 2011.

[96] S. J. Kwon and W. K. Chung, "Perturbation compensator based robust tracking control and state estimation of mechanical systems." Springer, New York, 2004.

[97] Y. Xia, Z. Zhu, and M. Fu, "Back-stepping sliding mode control for missile systems based on an extended state observer," *IET Control Theory Appl.*, vol. 5, no. 1, pp. 93-102, 2011.

[98] M. Yue, B. Y. Liu, C. An, and X. J. Sun "Extended state observer-based adaptive hierarchical sliding mode control for longitudinal movement of a spherical robot," *Nonlinear Dyn.*, vol. 78, pp. 1233-1244, 2014.

[99] R. E. Best, *Phase Locked Loops*, 5th Edition, McGraw-Hill, 2003.

[100] D. Jovcic, "Phase locked loop system for FACTS," *IEEE Trans. Power Syst.*, vol. 18, no. 3, pp. 1116-1124, Aug. 2003.

[101] J. X. Wang, S, H. Li, J. Yang, B. Wu and Q. Li "Extended state observer-based sliding mode control for PWM-based DC-DC buck power converter systems with mismatched disturbances," *IET Control Theory Appl.*, vol. 9, no. 4, pp. 579-586, 2015.

[102] L. Jiang, Q. H. Wu, and J. Y. Wen, "Nonlinear adaptive control via sliding-mode state and perturbation observer," *IEE Proc. Control Theory Appl.*, vol. 149, no. 4, pp. 269-277, 2002.

[103] Y. Liu, Q. H. Wu, X. X. Zhou, and L. Jiang, "Perturbation observer based multiloop control for the DFIGWT in multimachine power system." *IEEE Trans. Power Syst.*, vol. 29, no. 6, pp. 2905-2915, Nov. 2014.

[104] J. Hernandez and J. P. Barbot, "Sliding observer-based feedback control for flexible joints manipulator." *Automatica*, vol. 32, no. 9, pp. 1243-1254, 1996.

[105] R. Sanchis and H. Nijmeijer, "Sliding controller-sliding observer design for nonlinear systems." *European Journal of Control*, vol. 4, pp. 208-234, 1998.

[106] C. Feltes, H. Wrede, F. W. Koch and I. Erlich, "Enhanced Fault Ride-Through Method for Wind Farms Connected to the Grid Through VSC-Based HVDC Transmission," *IEEE Trans. Power Syst.*,vol. 24, no. 3, pp. 1537-1546, Aug. 2009.

[107] J. M. Carrasco, L. G. Franquelo, J. T. Bialasiewicz, E. Galvan, R. C. P. Guisado, M. A. M. Prats, J. I. Leon, and N. Moreno-Alfonso, "Power-electronic systems for the grid integration of renewable energy sources: A survey," *IEEE Trans. Power Electron.*, vol. 53, no. 4, pp. 1002-1016, Aug. 2006.

[108] A. Moawwad, M. S. El Moursi, and W. Xiao, "Advanced fault ride-through management scheme for VSC-HVDC connecting offshore wind farms," *IEEE Trans. Power Syst.*, vol. 31, no. 6, pp. 4923-4934, Nov. 2016.

[109] S. Nanou, G. Patsakis, and S. Papathanassiou, "Assessment of communication-independent grid code compatibility solutions for VSC-HVDC connected offshore wind farms," *Electr. Power Syst. Res.*, vol.121, pp. 38-51, Apr. 2015.

[110] V. Yaramasu, B. Wu, P. C. Sen, S. Kouro, and M. Narimani,"High-power wind energy conversion systems: state-of-the-art and emerging technologies," *Proc. IEEE*, vol. 103, no. 5, pp. 740-788, May 2015

[111] *Requirements for Offshore Grid Connections in the Grid of TenneT TSO GmbH*, TenneT TSO GmbH, Bayreuth, Germany, December 2012.

[112] M. I. Daoud, A. M. Massoud, A. S. Abdel-Khalik, A. Elserougi, and S. Ahmed, "A flywheel energy storage system for fault ride through support of grid-connected VSC HVDC-based offshore wind farms," *IEEE Trans. Power Syst.*, vol. 31, no. 3, pp. 1671-1680, May 2016.

[113] A. Kirakosyan, M. S. E. Moursi and V. Khadkikar, "Fault Ride Through and Grid Support Topology for the VSC-HVDC Connected Offshore Wind Farms," *IEEE Trans. Power Del.*, vol. 32, no. 3, pp. 1592-1604, Jun. 2017

[114] T. D. Vrionis, X. I. Koutiva, N. A. Vovos, and G. B. Giannakopoulos, "Control of an HVdc link connecting a wind farm to the grid for fault ride-through enhancement," *IEEE Trans. Power Syst.*, vol. 22, no. 4, pp. 2039-2047, Nov. 2007.

[115] L. Xu, L. Yao, and C. Sasse, "Grid integration of large DFIG-based wind farms using VSC transmission," *IEEE Trans. Power Syst.*, vol. 22, no. 3, pp. 976-384, Aug. 2007.

[116] G. Ramtharan, A. Arulampalam, J. B. Ekanayake, F. M. Hughes, and N. Jenkins, "Fault ride through of fully rated converter wind turbines with AC and DC transmission systems," *IET Renew. Power Gener.*,vol. 4, pp. 426-438, 2009.

[117] I. Erlich, C. Feltes, and F. Shewarega, "Enhanced voltage drop control by VSC-HVDC systems for improving wind farm fault ridethrough capability," *IEEE Trans. Power Del.*, vol. 29, no. 1, pp. 378-85, Feb. 2014.

[118] A. Mullane, G. Lightbody, and R. Yacamini, "Wind turbine fault ride through enhancement," *IEEE Trans. Power Syst.*, vol. 20, no. 4, pp.1929-1937, Nov. 2005.

[119] Q. H. Wu, L. Jiang, and J. Y. Wen, "Decentralized adaptive control of interconnected non-linear systems using high gain observer," *Int. J. Control*, vol. 77, no. 8, pp. 703-712, 2004.

[120] L. Jiang, Q. H. Wu, and J. Y. Wen, "Decentralized nonlinear adaptive control for multi-machine power systems via high-gain perturbation observer," *IEEE Trans. Circuits Syst. I, Reg. Papers.*, vol. 51, no. 10, pp. 2052-2059, 2004.

[121] J. Chen, L. Jiang, Wei Yao, and Q. H. Wu, "Perturbation estimation based nonlinear adaptive control of a full-rated converter wind turbine for fault ride-through capability enhancement," *IEEE Trans. Power Syst.*, vol. 29, no. 6, pp. 2733-2743, 2014

[122] A. Yazdani and R. Iravani, *Voltage-Sourced Converters: Modeling, Control, and Applications.* Hoboken, NJ: Wiley, 2010.

[123] L. P. Kunjumuhammed, B. C. Pal, R. Gupta, and K. J. Dyke, "Stability analysis of a PMSG-based large offshore wind farm connected to a VSC HVDC," *IEEE Trans. Energy Convers.*, vol. 32, no. 3, pp. 1166-1176, Sep. 2017.

[124] B. Yang, T. Yu, H. C. Shu, et al, "Passivity-based sliding-mode control design for optimal power extraction of a PMSG based variable speed wind turbine", *Renew. Energy*, vol. 119, pp. 577-589, Apr. 2018,

[125] L. Jiang, Q. H. Wu, and J. Y. Wen, "Nonlinear adaptive control via sliding-mode state and perturbation observer," *IEE Proc. Control Theory Appl.*, vol. 149, no. 4, pp. 269-277, 2002.

[126] Y. Liu, Q. H. Wu, X. X. Zhou, and L. Jiang, "Perturbation observer based multiloop control for the DFIG WT in multimachine power system." *IEEE Trans. Power Syst.*, vol. 29, no. 6, pp. 2905-2915, Nov. 2014.

[127] Y.Y. Sang, B. Yang, L. Jiang, "Nonlinear adaptive control design for the VSC-HVDC light transmission system". *50th Int. Universities Power Engineering Conf. (UPEC)*, UK, Sep. 2015.

[128] S. Li, A. Timothy, T. Haskew, P. Swatloski, and W. Gathings, "Optimal and direct-current vector control of direct-driven PMSG wind turbines," *IEEE Trans. Power Electron.*, vol. 27, no. 5, pp. 2325-2337, May 2012.

[129] Z. Shen and V. Dinavahi, "Real-time device-level transient electrothermal model for modular multilevel converter on FPGA," *IEEE Trans. Power Electron.*, vol. 31, no. 9, pp. 6155-6168, Sep. 2016.

[130] L. Xu and L. Yao, "DC voltage control and power dispatch of a multiterminal HVDC system for integrating large offshore wind farms," *IET Renew. Power Gener.*, vol. 5, no. 3, pp. 223-233, May 2011.

[131] P. Bresesti, W. L. Kling, R. L. Hendriks, and R. Vailati, "HVDC connection of offshore wind farms to the transmission system," *IEEE Trans. Energy Convers.*, vol. 22, no. 1, pp. 37-43, Mar. 2007.

[132] X. Li et al., "Nanao multi-terminal VSC-HVDC project for integrating large-scale wind generation," in *Proc. IEEE Power Energy Soc. Gen. Meeting*, National Harbor, MD, USA, 2014.

[133] L. Harnefors, A. G. Yepes, A. Vidal, and J. Doval-Gandoy, "Passivity-based controller design of grid-connected VSCs for prevention of electrical resonance instability," *IEEE Trans. Ind. Electron.*, vol. 62, no. 2, pp. 702-710, Feb. 2015.

[134] R. E. Torres-Olguin, M. Molinas, and T. Undeland, "Offshore wind farm grid integration by VSC technology with LCC-based HVDC transmission," *IEEE Trans. Sustain. Energy*, vol. 3, no. 4, pp. 899-907, Oct. 2012.

[135] S. Heier, *Grid Integration of Wind Energy Conversion Systems*, New York: Wiley, 2006

[136] J. G. Slootweg, S. W. H. D. Haan, H. Polinder, and W. L. Kling, "General model for representing variable speed wind turbines in power system dynamics simulations," *IEEE Trans. Power Syst.*, vol. 18, no. 1, pp. 144-151, Feb. 2003.

[137] B. Yang, T. Yu, H. Shu, J. Dong, and L. Jiang, "Robust sliding mode control of wind energy conversion systems for optimal power extraction via nonlinear perturbation observers," *Appl. Energy*, vol. 210, pp. 711-723, Jan. 2017.

[138] B. Yang, L. Jiang, L. Wang, Wei Yao, and Q. H. Wu, "Nonlinear maximum power point tracking control and modal analysis of DFIG based wind turbine," *Int. J. Electr. Power Energy Syst.*, vol. 74, pp. 429-436, Jan. 2016.

[139] T. M. Haileselassie and K. Uhlen, "Impact of DC line voltage drops on power flow of MTDC using droop control," *IEEE Trans. Power Systems*, vol. 27, no. 3, pp. 1441-1449, Aug. 2012.

[140] F. Wu, D. Sun, and J. Duan, "Diagnosis of single-phase open-line fault in three-phase PWM rectifier with LCL filter ", *IET Gener. Transm. Distrib.*, vol. 10, pp. 1410-1421, May, 2016.

[141] A. Yazdani and R. Iravani, "Dynamic model and control of the NPC-based back-to-back HVDC system," *IEEE Trans. Power Del.*, vol. 21, no. 1, pp. 414-424, Jan. 2006

[142] D. Jovcic and K. Ahmed, *High-Voltage Direct Current Transmission: Converters Systems and DC Grids.* Hoboken, NJ, USA: Wiley, 2015

[143] J. Liu, J. Wen, W. Yao, and Y. Long, "Solution to short-term frequency response of wind farms by using energy storage systems," *IET Renew. Power Gener.*, vol. 10, pp. 669-678, 2016

[144] S. Liao, W. Yao, X. Han, J. Wen, and S. Cheng. "Chronological operation simulation framework for regional power system under high penetration of renewable energy using meteorological data," *Appl. Energy*, vol. 203, pp. 816-828, Oct. 2017.

[145] P. Wang and R. Billinton, "Reliability benefit analysis of adding WTG to a distribution system," *IEEE Trans. Energy Convers.*, vol. 16, no. 2, pp. 134-139, Jun. 2001.

[146] P. Kundur, "Power system stability and control," McGraw-Hill, New York, 1994.

[147] D. Babazadeh, A. Muthukrishnan, P. Mitra, T. Larsson and L. NordstrÖm, "Real-time estimation of AC-grid short circuit capacity for HVDC control application," in *IET Gener. Transm. Distrib.*, vol. 11, no. 4, pp. 838-846, 2017.

[148] A. Yogarathinam, J. Kaur, and N. R. Chaudhuri, "Impact of inertia and effective short circuit ratio on control of frequency in weak grids interfacing LCC-HVDC and DFIG-based wind farms," *IEEE Trans. Power Del.*, vol. 32, no. 4, pp. 2040-2051, Aug. 2017

[149] W. Li and J. Belanger, "An FPGA-based real-time HIL test bench for full-bridge modular multilevel STATCOM controller," in *Power Electronics and Applications (EPE'15 ECCE-Europe), 2015 17th European Conference on*, Sept 2015.